Universitá degli Studi di Padova

Sede Amministrativa: Università degli Studi di Padova

Dipartimento di Astronomia

DOTTORATO DI RICERCA IN: ASTRONOMIA
CICLO: XX

Structure and Evolution of Protoplanetary Disks

Coordinatore: Prof. Giampaolo Piotto

Supervisore: Prof. Piero Rafanelli

Dottorando: Davide Fedele

DATA CONSEGNA TESI
31 LUGLIO 2008

A Veronica

Contents

Sommario

La ricerca di pianeti al di fuori del sistema solare é uno dei maggiori settori di studio dell'astrofisica moderna. I pianeti si formano in un disco formato di gas e polvere interstellare che orbita attorno alla stella durante le prime fasi di formazione stellare. Tale disco *proto-planetario* é lo stadio avanzato del disco di accrescimento che si forma durante il collaso della nube molecolare progenitrice per conservare il momento angolare della nube. In questa fase, il disco trasporta momento angolare verso l'esterno e il materiale presente nel disco si muove su orbite sempre piú piccole fino ad essere catturato dalla stella centrale. Processi di coagulazione della polvere danno inizio al processo di formazione di pianeti. Il gas e la polvere presenti nel disco vengono dissipati lasciando, eventualmente, un sistema planetario. Una questione ancora aperta é: in che modo il materiale del disco viene dissipato. Qual é il meccanismo responsabile della dispersione del disco? Oltre alla formazione di pianeti, altri fenomeni possono giocare un ruolo fondamentale a riguardo. Tra questi: l'accrescimento di materia sulla stella centrale, la foto-evaporazione per opera della radiazione ultravioletta della stella, il vento stellare e/o del disco.

Lo scopo di questo lavoro é di studiare nel detaglio la struttura e l'evoluzione di dischi proto-planetari. Moderne tecniche investigative quali la spettroscopia ad alta risoluzione e l'interferometria infrarossa sono adatte allo scopo. L'alta risoluzione spettroscopica permette di risolvere il profilo di velocitá intrinseco delle righe del gas, sia atomico che molecolare. Questo permette di determinare sia la geometria sia le condizioni fisiche, quali velocitá, temperatura e densitá del disco. L'interferometria infrarossa é una tecnica relativamente nuova in astronomia. Tale tecnica permette di risolvere spazialmente regioni del disco non accessibili dalle tradizionali tecniche osservative. Il lavoro presentato di seguito mira a contribuire alla comprensione della struttura ed evoluzione dei dischi proto-planetari durante tre differenti fasi evolutive: a) *le primi fasi evolutive quando il sistema stella-disco é ancora (parzialmente) immerso in un inviluppo di materiale rimanente della nube progenitrice in collasso gravitazionale*; b) *la fase di "Classe II" (secondo la classificazione di Lada 1987). In questa fase il gas e la polvere del disco evolvono velocemente trasformando radicalmente la struttura del disco*; c) *la fase di transizione tra "Classe II" e "Classe III" durante la quale il gas e la polvere vengono dissipati.*

Durante le primi fasi di evoluzione del disco, il sistema stella-disco-inviluppo va incontro a potenti instabilitá dovuti all'improvviso e rapido aumento del tasso di accrescimento di massa dal disco alla stella. Tale fenomeno é noto come "esplosione di tipo FU Orionis" (che é il prototipo) ed é visibile come un'aumento brusco della luminositá del sistema. Il tasso di accrescimento puó variare di $4-5$ ordini di grandezza passando da $10^{-7}-10^{-8}$ $M_\odot$ yr^{-1} a $10^{-3}-10^{-4}$ $M_\odot$ yr^{-1}. Studi statistici suggeriscono che tutte le stelle di piccola massa sperimentano simili fenomeni piú volte durante questa fase evolutiva. Verso la fine del 2003, la stella giovane V1647 Orionis nella nube L1630 all'interno della nube molecolare Orion B ha mostrato una simile esplosione. Alcune caratteristiche dell'evento sono del tutto simile al fenomeno FU Orionis. Noi abbiamo condotto un'analisi spettroscoprica e fotometrica durante tutta la fase di massima luminositá del sistema, confermando la natura dell'esplosione come dovuta ad una instabilitá termica del disco. Le nostre osservazioni hanno anche messo in evidenza per la prima volta la connessione tra un evento di accrescimento e l'emissione di un getto di tipo Herbig-Haro.

Durante la fase di Classe II, la polvere del disco si coagula e forma via via strutture di dimensioni maggiori. Questo é il primo stadio per la formazione di pianeti. Noi abbiamo applicato l'alta risoluzione spettrale e l'interferometria infrarossa con lo scopo di comparare direttamente l'emissione del gas e della polvere in tre dischi proto-planetari. Questo lavoro fornisce alcune importanti informazioni sulla struttura relativa di queste due componenti. Un disaccopiamento fisico del gas e della polvere puó avvenire portando a sostanziali differenze nella distribuzione dei due. Una volta avvenuto il disaccoppiamento, la polvere puó "cadere" piú velocemente verso l'interno del disco aumentando il rapporto di massa tra polvere e gas. A sua volta, un maggiore rapporto di massa polvere-gas puó indurre la formazione di pianetesimi attraverso instabilitá gravitazionale.

La transizione tra la fase di Classe II alla fase di Classe III é caratterizzata da diversi processi che portano a dissipare il disco. Tra questi, l'accrescimento di materiale sulla stella e la foto-evaporazione sono i piú efficaci. La formazione di pianeti é dunque in competizione con tali fenomeni e non tutti i dischi potrebbero essere in grado di formare pianeti. Per questo motivo, una quantitá fondamentale é il tempo scala dell'accrescimento, ovvero l'etá alla quale l'accrescimento termina. Questo é indirettamente una misura del tempo scale di dissipazione del gas, che é rilevante per la formazione di pianeti giganti. Noi abbiamo osservato un campione di ammassi stellari giovani di differente etá allo scopo di tracciare l'evoluzione dell'accrescimento. I primi risultati mostrano che l'accrescimento termina in un tempo scale simile alla dissipazione della polvere, $5-10$ Myr.

Abstract

The hunt for exo-planets is one of the major topics of modern astronomy. Planets are thought to form in a circumstellar disk orbiting around the star during its pre-main sequence evolution. Such a *protoplanetary* disk is believed to be an evolved form of the accretion disk formed during the collapse of the molecular cloud to conserve the initial angular momentum. During the phase of disk accretion, angular momentum is transferred to larger radii permitting the accretion of material onto the central star. At this stage, coagulation of dust grains is thought to take place in the mid-plane of the disk, giving rise to the formation of planets. From our solar system and from observations of *debris* disks (the remnant of the protoplanetary disks) we know that both the gas and the dust have to dissipate either forming a planetary system, or being in some way swept away from the disk. How dust and gas dissipate? Which is the main driver of disk dispersal?

The scope of this thesis is to investigate the structure and evolution of protoplanetary disk. High resolution observational techniques such as high resolution optical/infrared spectroscopy and infrared interferometry are well suited for this purpose. High resolution spectroscopy allow to resolve the velocity profile of disk emission lines and determine some important parameters such as the disk geometry and the physical conditions of the line emitting region. Infrared interferometry allows to spatially resolve and constraint the disk geometry within the planet forming region.

The work presented here aims at contributing to the comprehension of the disk structure and evolution at three different evolutionary stages: a) *the early phase when the system is still (partially) embedded in a remnant of the molecular cloud*; b) *the so-called Class II phase (from the classification of Lada 1987). At this stage gas and dust evolve rapidly leading to drastic changes of the disk structure*; c) *the transition phase from Class II to Class III when gas and dust are dissipated leaving, eventually, a planetary system.*

During the early phases of disk evolution the star-disk-envelope system experience powerful instability which are related to rapid enhancement of the mass accretion rate on a timescale of few months. These events are recognizable as so-called FU Orionis outbursts, in which the optical brightness of the system can increase by 4 or more magnitudes. The mass accretion rate increases from 10^{-7} – 10^{-8} $M_\odot$ $yr^{-1}$to 10^{-3}–10^{-4} $M_\odot$ yr^{-1}. Statistical studies suggest that young low-mass stars experience several FU Orionis outburst. In late 2003, the young star V1647 Orionis in the L1630 Ori cloud within the Orion B molecular cloud went into outburst. The outburst shares some properties of the FU Orionis outburst. Following spectro-photometric observations confirmed the nature of the outburst as a disk-instability event. We also find, for the first time, probe of a direct link between an accretion event and the ejection of an Herbig-Haro object (HH).

During the Class II phase dust coagulation and grain growth occur. This is the first step of planet formation. We applied high resolution optical spectroscopy and infrared interferometry to direct compare gas and dust emission from the disk surface of three protoplanetary disks. This study gives some insight on the relative distribution of gas and dust in disk and on the temporal evolution of the two components. A physical decoupling of gas and dust may occur leading to changes in the relative structure of the two (different scale height) and to rapid settling of dust on the disk midplane. This may increase the dust-to-gas mass ratio in the disk interior and, according to recent simulation, may trigger the formation of planetesimals via gravitational instability.

The transition phase from a Class II to a Class III system is characterized by various processes which dissipate the disk material. In particular, viscous accretion and photo-evaporation are very efficient in removing disk material and planet formation is likely in competition with disk dispersion. For this reason, a fundamental quantity is the mass accretion timescale, i.e. the time at which the disk accretion phase ceases. In turn, the time at which the disk accretion phase ceases is a strong constraint on the gas dissipation timescale, relevant for the formation of giant planets. We have observed a number of young stellar clusters of different age aimed at tracing the evolution viscous accretion with time. The preliminary results show that the accretion seems to cease at similar age of the dust dissipation, i.e. within 5 – 10 Myr.

1

Introduction

In this thesis we will discuss the structure and evolution of circumstellar disks surrounding young stars during the early, pre-main-sequence (PMS), evolutionary phase. The disk, formed during the star formation process, is the locus of planet formation. How the gas and the dust forming the disk turn into planets is one of the fundamental question of modern astrophysics. We bring here our contribution to three main topics: a) *the stability of protoplanetary disks*; b) *resolving the dust and gas distribution of the planet forming region*; c) *the evolution of mass accretion rate; setting the planet formation timescale.*

In this chapter, we briefly review the star formation process and the current understanding of the structure and evolution of protoplanetary disks.

1.1 From gas to stars

According to modern cosmology the Big Bang formed a diffuse, hot and dense gas, mainly H and He. The expansion of the universe and the initial anisotropy allowed the aggregation of the gas up to the formation of the first structures. Since the formation of the first stars, star formation occurred at any time and is still occurring in the current universe. During the elapsed time a substantial part of the initial gas turned into stars and these are now the main constituent of galaxies. Thanks to the ongoing star formation in the Galaxy we have a comprehensive – but still incomplete – picture of the transformation from gas to stars.

The observations at radio wavelength have revealed that gas in the Galaxy is often grouped in large structures, clouds. These clouds are mainly formed by molecular gas. The most abundant molecule is H_2, followed by CO. Such *molecular clouds* have low temperature ($10 \div 50$ K) and density of few $10^{2-4}\ cm^{-3}$ depending on the size of the cloud. Molecular clouds are typically in mechanical equilibrium, that is, the collapse under the gravitational force is balanced by the internal pressure. The typical width of the emission line from a molecular cloud is larger than width due to pure thermal motion of the gas. This rules out the kinetic energy (due to thermal motion only) as the force contrasting the gravitation. The observations are indeed consistent with the presence of turbulent motions and the presence of magnetic field. Both these phenomena may sustain the gravitational force. Furthermore, the rotation of the cloud may also play a role.

Star forming regions are often spatially linked with molecular clouds. This evidence suggests a connection between the two. The mechanical equilibrium of a cloud may be broken as soon as either an internal (e.g. local superdensity, ambipolar diffusion) or external (e.g. stellar wind, radiation pressure, supernova explosion) cause occurs. In this case the gravitational force may overwhelm the balancing pressure and give rise to the collapse of the cloud. The collapse is free-fall. The free-fall will stop as the core reaches the quasi-hydrostatic equilibrium and forms a *protostar*. The protostar will now contracts and emits energy released by the gravitational contraction. The temperature and the density of the core increase. If there is enough mass the core of the protostar will reach a temperature of $1{\times}10^6$ K and give rise to the thermonuclear reactions with the burning of the Deuterium. In modern astrophysics, the locus of the Hertsprung-Russel (HR) diagram coincident with the Deuterium burning limit ($1{\times}10^6$ K) is called *stellar birthline*. At slightly higher temperature ($3{\times}10^6$ K) begins the Lithium burning. When the fuel is exhausted the core of the star contracts until a temperature of $\sim 10^7$ K is reached and starts the burning of Hydrogen. The star is now on the Zero-Age-Main-Sequence of the HR-diagram. Only objects more massive than 0.075 $M_\odot$ will be able to ignites Hydrogen.

1.2 Circumstellar disk

The typical spectral energy distribution (SED) of a PMSs is characterized by a strong excess over the stellar photosphere. This excess extends from slightly below 1μm up to millimeter wavelength. The origin of this excess is circumstellar dust which absorbs stellar UV/optical emission and re-emits it at longer wavelength. It is today widely accepted that this dust is confined to

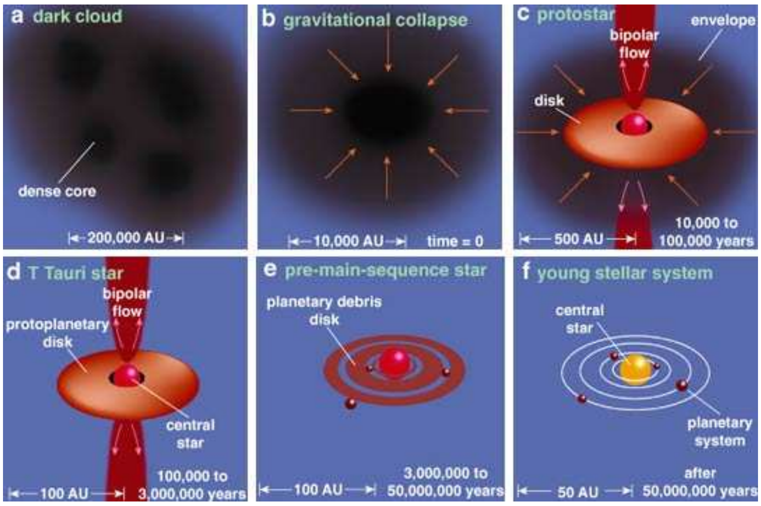

Figure 1.1: *From Green 2001 [53]*: Sketch of star formation process. The collapse of the molecular cloud forms a central star and a circumstellar disk. The mass accretion onto the central star proceeds in two steps: 1) the disk accretes material from an infalling envelope (remnant of the cloud) and 2) the disk transfers angular momentum to large distances permitting the accretion of material into the star. A bipolar flow and a disk wind develops. The disk material dissipates and, eventually, a planetary system is formed.

a disk structure orbiting the star during its pre-main-sequence evolution. This is consistent with the star formation theory. To conserve the initial angular momentum of the cloud, the infalling material will indeed form an equatorial disk-like structure. Fig. 1.1 shows a schematic view of the star formation process.

Following the classification of Lada [92], the different evolutionary stages of the pre-main-sequence evolution can be traced by the SED. In particular, the infrared excess may be used as an observational measure of the stellar youth. Let us introduce the infrared spectral index α_{IR}:

$$\alpha_{IR} = \frac{dlog(\lambda F_\lambda)}{dlog(\lambda)} \tag{1.1}$$

where λ is the wavelength and F_λ the observed flux. Objects for which $\alpha_{IR} > 0$ belong to the Class I. As the infrared excess decreases ($-1.5 < \alpha_{IR} < 0$), the system is said to be a Class II source. Class III indicates a star with no, or little, infrared excess. Objects detected at infrared and millimeter wavelengths and with no optical counterpart belong to the Lada Class 0.

The Class 0 corresponds to the early protostar phase. At this stage the central object is highly embedded in the core and is not visible in the optical. As the system ages, the protostar becomes visible at optical wavelengths corresponding to a Class I. An envelope, remnant of the initial cloud, may still be present. The bulk of the stellar mass is accreted during these early stages. The Class II phase is characterized by the PMS star and an optically thick circumstellar disk. No, or little, dust is present around a Class III source where the star reached the main sequence.

We will concentrate now on the Class II objects. After the disk formation, matter falls in from the cloud onto the disk. The disk, in turn, transfers angular momentum to large radial distance allowing the accretion of material into the central star. The infall of material produces a UV and optical *"hot"* continuum (*veiling*) with many emission lines. In some cases the optical and UV excess continuum emission overwhelms that of the stellar photosphere.

The hot continuum was originally thought to be produced in a shear boundary layer between the rapidly rotating disk and the more slowly rotating central star (Lynden-Bell & Pringle [102]). Theoretical work on accretion in classical T Tauri stars (CTTSs) has moved away from this picture in favor of magnetospheric accretion (e.g. Königl [88]). A sketch of the magnetospheric accretion model is shown in Fig. 1.2. In this model, the stellar magnetic field truncates the disk at some inner radius and accretion continues onto the star by gas infall along magnetic field lines connecting the star to the disk near the truncation radius. In the magnetospheric accretion model, the hot continuum is produced by a shock at the base of the magnetospheric accretion column, near the stellar surface while the optically thick, warm ($\sim 10^4\ K$) and nearly free-falling gas in the stellar magnetosphere is responsible for the emission lines.

Recent X-ray surveys with the Chandra and XMM-Newton space telescope have revealed an high X-ray activity from young stars. Fig. 1.2 shows the different regions where the high-energy radiation can be produced at the disk-star boundary. These are the regions where magnetic reconnections and/or shocks occur (e.g. Montmerle [114]).

1.3 Disk structure

Disks are commonly observed around T Tauri stars (PMS stars with $M_{*}< 1.5\ M_{\odot}$) and around Herbig AeBe stars (HAEBE, PMS stars with $1.5\ M_{\odot} < M_{*}< 5\ M_{\odot}$). Signatures of disk were also detected in the very low-mass brown dwarfs objects (e.g. Jayawardhana, Mohanty & Basri [75]) and in the massive $7M_{\odot}$ star IRAS20126+4104 (Cesaroni et al. [26]). In the vast majority of

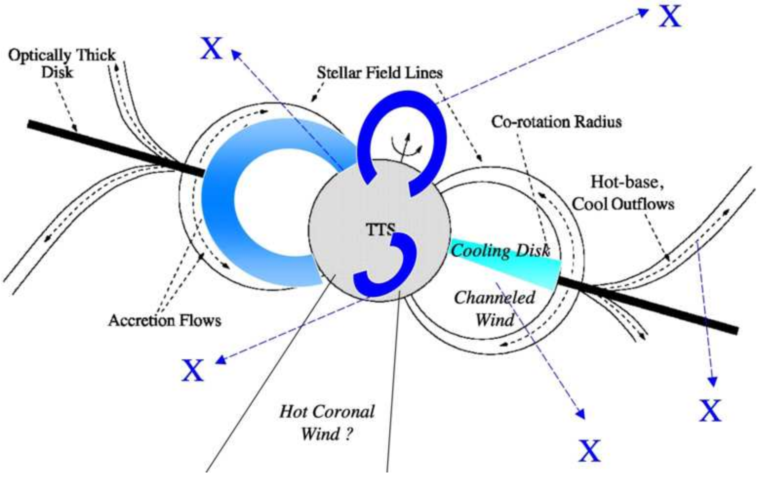

Figure 1.2: *From Montmerle [114]*: Sketch of the magnetospheric accretion during the pre-main sequence phase of a star. The optically thick disk is truncated by the stellar magnetic field lines. Through the field lines material from the disk is transported into the central star. Various X-ray emitting regions may exist

cases, the disks are detected around the Lada Class II objects. This is due to the longer duration of the Class II phase ($10^6 - 10^7$ yr) compared to the Class I phase (10^5 yr). The main internal energy source in these structures is the dissipation of kinetic energy as material accretes onto the central star, *viscous accretion.* For the typical mass accretion rate measured in T Tauri and HAEBE stars, $10^{-7} - 10^{-12}$ $M_\odot$ yr^{-1}, the energy released ($\propto \dot{M}_{acc}$) is low and the disk is mainly heated by the stellar radiation. The disk is said *passive.* The dust present in the disk surface absorbs a large amount of the stellar optical/UV radiation. On the other hand, the gas interacts with the stellar radiation through photoionization, photodissociation of molecules, photoevaporation, etc. Gas and dust in the disk surface shield the disk's interior from the stellar radiation. As a consequence, for a given radius, the temperature in the disk is higher on the disk surface and decreases towards lower height. For this reason disk features are often seen in emission.

On rare occasions, the mass accretion rate in PMS stars is seen to increase by more than four orders of magnitude on a timescale of months. These events are recognizable as so-called FU Orionis outbursts, in which the optical brightness of the system can increase by 4 or more magnitudes. The physical reason of such a FU Orionis outburst is that due to a disk instability the mass accretion rate onto the central star changes, within a period less than a month, from those commonly found around PMS stars into values of 10^{-3}–10^{-4} $M_{\odot}$ yr^{-1}. Statistical studies suggest that young low-mass stars experience several FU Orionis outburst during the early phase of stellar evolution. During a FU Ori event, the accretion luminosity may become the first energy source and the disk is said *active*. In this case the temperature gradient is altered. The disk mid-plane is now hotter than the disk surface and absorption features may appear in the disk spectrum.

The SED is one of the most basic and powerful tool of investigation in astrophysics. The absorption/re-emission of stellar radiation by means of dust is clearly visible in the SED of a PMS star as an excess luminosity over the stellar photosphere at infrared-millimeter wavelength. Dust emission is related to temperature and size of the grains. For a disk in Keplerian rotation around the star, the temperature is higher close to the star and decreases at larger radii. For a solar-type star, near infrared wavelengths trace the hot dust close to the star ($\sim$ 0.03 - 0.1 AU). Longer wavelengths trace cooler dust between $\sim$ 0.2 - 10 AU with mid-infrared excess and between $\sim$ 10 - 100 AU at far-infrared/millimeter. At millimeter wavelengths in particular, the disk emission becomes optically thin and the emission is sensitive to the total disk mass. It should be kept in mind that the "wavelength-distance" relation is valid only in first approximation. The vertical stratification of gas and dust and grains properties may have important role on the disk emission.

Infrared interferometric observations have shown that the inner edge of the dust disk is much larger than those predicted by the magnetospheric accretion (e.g. Millan-Gabet et al. [111]). Given the high temperatures at small stellar distance, the innermost part of the disk is voided of dust due to the sublimation of grains. Within the dust sublimation radius, gas may still be present. At the inner edge of the dusty disk, the disk is "puffed-up" (Dullemond, Dominik & Natta [37]) and curved (Isella & Natta [71]). The disk immediately beyond the puffed-up inner edge is shadowed and is not directly irradiated from the star. Fig. 1.3 shows a sketch of the disk structure and of the inner edge of the dust for a passive disk (from Isella, Testi & Natta [72]).

From the analysis of the infrared color of a number of HAEBE stars it was found that there exist disks of two categories: group I and group II (Meeus et al. [108]). Group I disks have strong mid-infrared flux. Group II objects have a reduced (compared to group I) mid-infrared flux. Figs. 1.4 show the typical SED of the two groups (from Dullemond & Dominik [37]). The difference in mid-infrared flux seems to correlate with the disk geometry. Disks belonging to Group I have flared geometry, that is, the scale height of the disk increases with the distance from the central star. Group II disks have flat geometry.

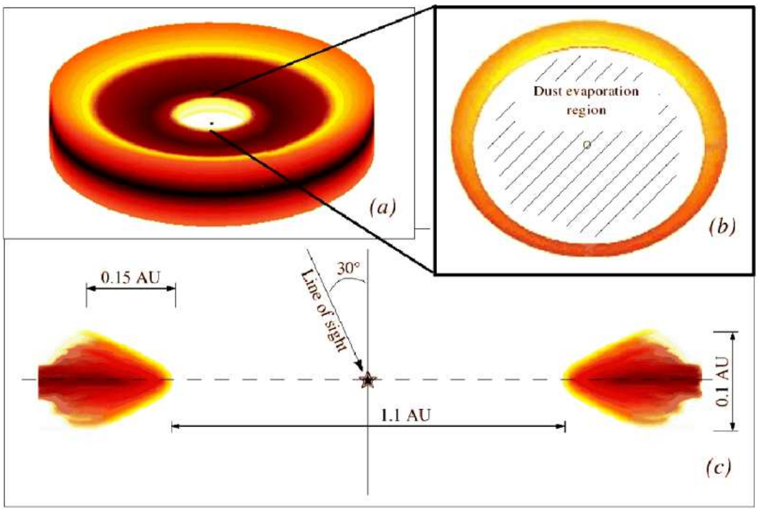

Figure 1.3: *From Isella, Testi & Natta [72]*: Sketch of the dust disk structure. A) Disk structure with an inner puffed up rim shadowing the outer part of the disk. The flaring disk emerges from the shadow at larger distance (5 - 10 AU); B) Image of the inner rim from Isella & Natta 2005 for a a disk inclination of 30°; C) Vertical (edge on) section of the inner rim. The curvature of the surface of the rim is caused by the variation of the dust evaporation temperature with the height above the disk midplane

This correlation is supported by the existence of the inner puffed-up rim. The shadow of the inner edge will prevents a flat disk from receiving stellar radiation. In the case of a flared structure instead, the disk will re-emerges from the shadow at large radial distance. Compared to Group II sources, a Group I disk is illuminated by the star not only at the inner edge but also at larger distance. This produces the extra mid-infrared luminosity in flared disks visible in Fig. 1.4. A pictogram of the two disk shape is shown in Fig. 1.5.

This bimodality might be in reality the consequence of a temporal evolution of the disk rather than a structural diversity of disks. The initial composition of the disk is similar to that of the interstellar medium (ISM), i.e. gas and dust. The ISM is mainly formed by small dust grains mostly amorphous silicates. Mid-infrared observations reveled the presence of much larger grain size and dust crystalline in circumstellar disk around HAeBe stars (e.g. van Boekel et al. [148]). Acke et al. [3] find a correlation between the size of the grain and the disk's geometry: disks with a flat geometry have larger grain size compared to their flared counterparts. This may suggest that as grain

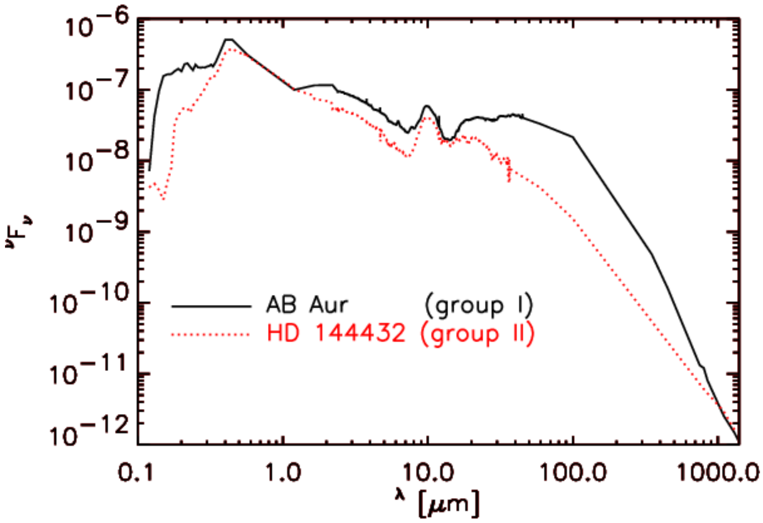

Figure 1.4: *From Dullemond & Dominik [39]*: Example of SED for a group I and group II source from Meeus et al. [108].

growth in size they tend to settle on the disk mid-plane and the disk, initially flared, becomes flat.

An important role in disk evolution is played by gas. The initial content of the disk reflects the ISM, that is dust is only a small percent of the disk mass. The bulk of the disk mass is in the gas (99 %). The relative mass ratio and the thermal coupling of dust and gas is important for the disk structure and evolution. In particular, in the upper layers of a disk the gas temperature may exceed the dust temperature and the two disk components tend to decouple. The dust settle very fast to the disk mid-plane and the dust-gas ratio in the disk interior increases. In turn, the dust settling favors the physical separation between gas and dust until all the dust settle towards the mid-plane leaving, eventually, a region of gas in the upper layers of the disk. In the disk mid-plane, as the dust-to-gas ratio increases, gravitational instability may lead to the formation of planetesimals (Johansen et al. [77]; Youdin & Shu [157]).

1.3.1 Disk dissipation and planet formation

When the star reaches the main-sequence, dust and gas forming the circumstellar disk are mostly dissipated. A remnant of the dust disk is sometimes visible as an excess beyond 10μm. In these objects the infrared excess can be fitted with a single temperature black body. These *debris disks* disks are

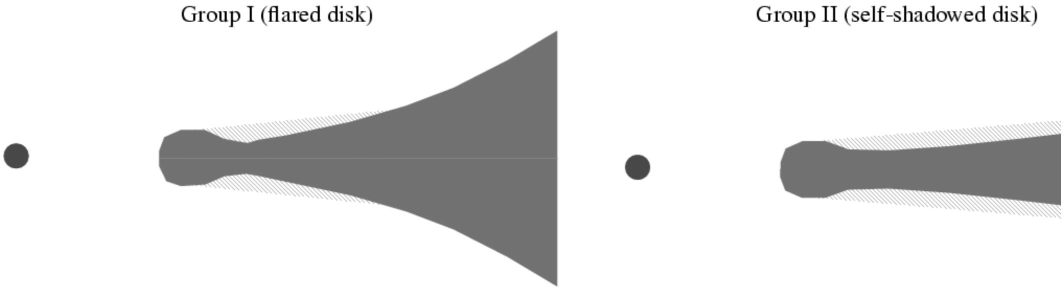

Figure 1.5: *From Dullemond & Dominik [39]*:Pictogram of a flared and flat disk geometry corresponding to group I and II respectively.

optically thin. How gas and dust dissipate is still unknown and is matter of debate between astronomers. From near- and mid-infrared surveys (e.g. Jayawardhana [74]; Haisch et al. [59]; Hillenbrand [68]) it was found that for star forming regions older than 1 Myr there is a steady decline with time in the fraction of stars showing excess emission (Fig. 1.7). Responsible for this emission are the small and warm dust grains present in the inner region. This means that the small dust grains component of protoplanetary disks is gradually dissipated as the system ages. Another interesting result comes from the analysis of Spitzer space telescope observations. Spitzer permitted the identification of a new category of circumstellar disk around young stars. These objects show less strong infrared excess, especially at shorter wavelength, compared to their counterparts. The frequencies of these disk is, to date, low, suggesting that they may represent a fast evolutionary stage of disk evolution. In this perspective, these objects are called *transitional* disks in the sense that they seem to be in a transition phase between the optically thick disk (Lada Class II) to the optically thin *debris* disk phase (Class III). Although in some cases this peculiar SED may result from a common disk around a binary system (e.g. CoKu Tau/4 Ireland & Kraus [70]), the lack of near-infrared flux in transitional disks suggests that dust is swept out by some mechanism. For this reason, transitional disks are an optimal astrophysical laboratory to study the dissipation of disks.

There are a number of phenomena which may be responsible for disk dissipation. These are: viscous accretion, photoevaporation, stellar encounters, outflow via stellar/disk winds and planet formation. Understanding these mechanisms and which of these is the main driver for the dispersion of gas and dust in disk is one of the goal of modern astrophysics.

1.4 From Disk to Planets

In 1995 Michel Mayor and Didier Queloz claimed the first discovery of an extrasolar-planet orbiting around a solar-like star (51 Pegasi B, [105]). More than 200 *exo-planets* have been discovered after 51 Pegasi B using both direct and indirect techniques. An interesting result is that planetary systems around other stars have different properties from those characterizing the Solar System. The diversity in orbital motion and properties of the known *exo-planetary systems* may reflect the diversity in the properties of the regions in which planets form. Circumstellar disks around young stars are the natural location where planet formation takes place. For this reason these disks are also named *protoplanetary disk*. Two main mechanisms are nowadays in competition in the theory of giant planet formation: the core accretion model (Pollack et al. 1996 Icarus 124, 62) and the gravitational instability model (Boss 2004 ApJ 610, 456). In the conventional *core accretion* planet formation model, a giant planet forms in a 3-step process: 1) a solid core forms by accretion of solid planetesimals which themselves were formed by sedimentation and coagulation of small dust grains; 2) as the core reaches a critical mass ($\sim$ 15-20 $M_\oplus$), gas falls onto the rocky core forming a gaseous envelope; 3) a runaway gas accretion occurs and the envelope is attracted onto the core. The time necessary to form a giant planet is 1 – 10 Myr.

1.5 Overview of this thesis

With this work we aim at helping the discussion on the structure and evolution of protoplanetary disks. We bring our contribution to three main topics: a) *the stability of protoplanetary disks*; b) *resolving the dust and gas distribution of the planet forming region*; c) *the evolution of mass accretion rate; setting the planet formation timescale*. Here we briefly introduce the scientific rationale of these projects.

1.5.1 Stability of protoplanetary disks

The first project of my PhD is a spectroscopic and photometric follow-up of a young eruptive star, V1647 Ori, suspected to be a FU Orionis object. The star is located in the L1630 Ori cloud within the Orion B molecular cloud complex. The observations were carried out between February 2004 and January 2006 with the *FOcal Reducer/low dispersion Spectrograph* (FORS2) at VLT in Paranal, Chile, and with the *Thermal Infrared Multimode Instrument* (TIMMI2) at ESO 3.6m telescope in La Silla, Chile. Although V1647 Ori cannot be classified as a “pure” FU Orionis object, these observations are in line with what is expected from a disk instability model.

In planet formation models usually the assumption is made that protoplanetary disks are “quiet” regions that slowly evolve, via steady state, to form a planetary system and then dissipate. The FU Orionis events statistics and the recent outburst of V1647 Ori suggest instead that disks are dynamically unstable systems. This finding has important consequence on the comprehension of disk’s evolution and future model of planet formation have to take this result into account.

1.5.2 Resolving the dust and gas distribution of the planet forming region

A protoplanetary disk may extended from 10^2 AU up to 10^3 AU, however, from the orbital properties of the more than 200 exo-planets discovered so far, we know that only the inner disk ($r < 50$ AU) is involved in the formation of planets (the solar system itself extends to ~ 40 AU). Despite its importance, the exploration of the inner disk is challenging at present mainly for the lack of spatial resolution of modern instrumentation. At the nearest star-forming region (distance of 150 pc), the angular scale subtended by the inner 50 AU of the disk is $\leq 0''.33$. Two techniques are very promising in the investigations of this region: high spectral resolution spectroscopy and infrared interferometry.

A second project that I developed during my PhD is an independent analysis of the gas and dust emission from the inner region of the protoplanetary disks in three Herbig AeBe stars (intermediate-mass PMSs). Investigations of the gas emission is based on spectrally resolved observations of the forbidden [O I] 6300,6363 Å lines with the *Ultraviolet and Visual Echelle Spectrograph* (UVES) at VLT. Investigation of the dust emission is based on spatially resolved observations of the 10μm silicate bump with the *Very Large Telescope Interferometer* (VLTI) in combination with the *Mid-Infrared Interferometric Instrument* (MIDI). Both the [O I] and the 10μm emission arises from the same surface layer of the inner disk where the opacity is $\tau \sim 1$ for the optical lines (Acke et al. 2005 A&A 436, 209), and the dust is heated enough by the stellar radiation (D’Alessio et al. 2001 ApJ 553, 321). As shown by Acke & van den Ancker (2006 A&A 449, 267), modeling the [O I] spectral line profile it is possible to calculate the intensity-versus-radius curve ($I(R)$) of the circumstellar disks directly from the gas emission. From this information we can deduce the spatial extent and shape of the [OI] emitting region. Fig. 1.6 shows $I(R)$ derived from the spectral shape of the [OI] 6300 Å line in the Herbig AeBe star HD 100546 by Acke & van den Ancker 2006. In this way it is also possible to detect gaps in the velocity distribution of the [O I] emission.

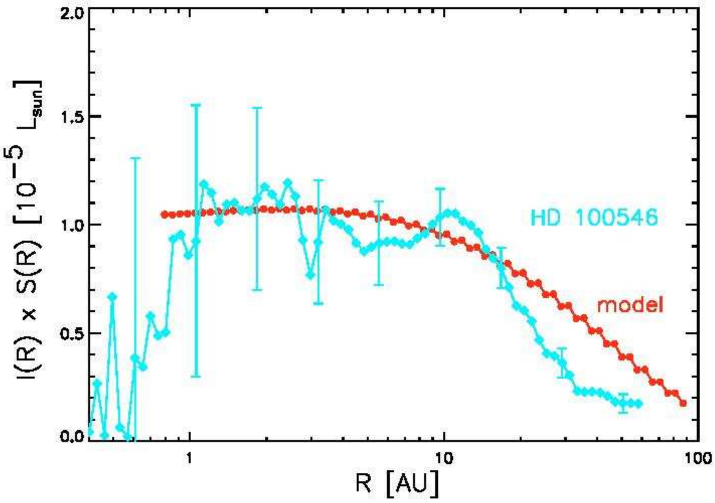

Figure 1.6: *From Acke & van den Ancker [5]*: Intensity-versus-Radius profile derived from the spectral shape of the [OI] 6300 Åline in the Herbig AeBe star HD 100546. The [OI] emitting region is more compact than the model (red) suggests.

Such structure could be explained with ongoing planet, or stellar companion, formation.

The high spatial resolution achievable with the VLTI ($\sim 0''.01$ at 10μm) and the spectral capabilities of the MIDI beam-combiner, allow us to compute $I(R)$ from the thermal dust emission in the spectral range 7-14 μm.

A further development of this project is to extend the observations to near-infrared wavelengths. The warm temperature ($T \geq 150$ K) and high density ($n = 10^9 - 10^{15}$ cm^{-3}) of the upper layer of the inner disk are expected to excite a rich near-infrared spectrum of molecular ro-vibrational transitions. High resolution near-infrared spectroscopy is then sensitive to such physical environment.

1.5.3 Tracing the evolution of mass accretion rate in PMSs: disk's lifetime

The dissipation timescale found so far – $5 \div 9$ Myr – is representative only for the dust. The bulk of the protoplanetary disks mass is however in the gas. In the interstellar medium (ISM) the gas to dust mass ratio is $\sim 99\%$. There is no reason to suspect that in disk the gas to dust mass ratio strongly differs from that observed in the ISM. The gas dissipation timescale is then the most stringent constraint on the formation of giant planets. An indirect measure of the gas dissipation time scale can be determined by tracing the time evolution of accretion, as traced by the Hα emission (see e.g. Jayawardhana et al. 2006, ApJ, 648, 1206). Our knowledge about the evolutionary timescales of protoplanetary disks have been based so far on small number statistics. The only way we have to investigate the evolution of these systems along the time axis is to observe many young star clusters in order to cover a relevant range in system's age. For this reason I started a spectroscopy campaign of a sample of young stellar clusters selected to cover the age interval between 1 to 100 Myr. This program is based on multi object spectroscopy with the *VIsible MultiObject Spectrograph* (VIMOS) at VLT (Paranal, Chile) of a large number (200-400) of stars in each cluster. The main goal of this program is to look for variations on the Hα emission, and then of accretion, with the age of the system. This will also allow to measure the accretion timescale and see whether accretion ceases at the (dusty) disk dissipation timescale.

These observations will provide the best constraint to date on the timescale for planet formation. The two main planet formation theories predict different formation timescale: few Myr for the gravitational instability model, ~ 10 Myr for the core accretion model. The result of this project may then directly rule out one of the two planet formation scenarios.

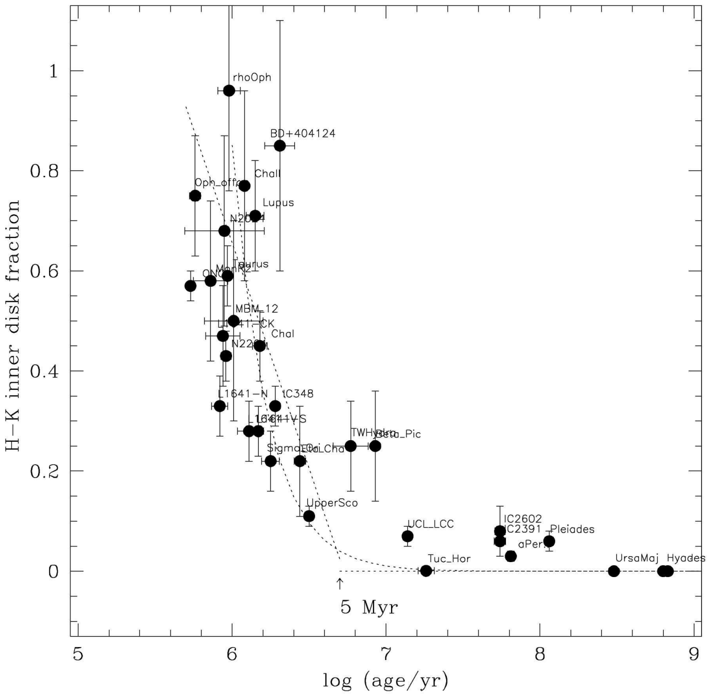

Figure 1.7: *From Hillenbrand [68]* : Inner disk fraction vs stellar ages inferred from H–K excess measurements. The linear and exponential fits were derived for ages < 30 Myr. The H–K excess shows a steady decline with the age of the cluster. This excess is due to the re-processing of stellar photons by the dust present in the inner part of the disk. The decline of the H–K excess suggest a progressive dissipation of the inner region of the disk.

2

Introduction to infrared interferometry

In this chapter we briefly summarize some basic concepts of infrared interferometry. We focus in particular on the application of interferometry to mid-infrared observations with the *MID-infrared Interferometric instrument* (*MIDI*) at the *Very Large Telescope Interferometer* (*VLTI*). The reader interested into a more detailed description of infrared interferometry is invited to consult other references (e.g. *Observing with the VLTI*, Perrin & Malbet [129]; *Principle of long baseline stellar interferometry*, Lawson [94]).

2.1 Introduction

The spatial resolution, θ, achievable with a generic telescope of (circular) aperture diameter D is:

$$\theta = 1.22\frac{\lambda}{D} \tag{2.1}$$

with λ the observing wavelength. This means that at, e.g., 2.2μm the *Hubble Space Telescope*, with an aperture of 2.4 m has a spatial resolution of $\sim 0\farcs23$. If we neglect the effect of the atmospheric turbulence, the 8.2 m diameter of the *Very Large Telescope* will have a spatial resolution of $0\farcs068$. An astronomical interferometer is formed by two or more telescopes and by a beam combiner which combines the light coming from the different apertures and send the combined signal to a detector. In this case, the spatial resolution is $\propto \lambda/B$, where B is the baseline length. Similarly to the case of the Young's experiment, the combined signal is a sinusoidal oscillation of the light intensity as a function of time or optical path difference (OPD): the *interferometric fringes*. The quantities measured by an interferometer are the contrast and the location of the fringes. The fringe contrast and location are equivalent to the amplitude and the phase of the *complex visibility*. The complex visibility, V, is the Fourier transform of the source brightness distribution:

$$\mathcal{V}(u,v) = \frac{\int_{\Delta\alpha}\int_{\Delta\beta} d\alpha d\beta I(\alpha,\beta) e^{-2\pi i(\alpha u+\beta v)}}{\int_{\Delta\alpha}\int_{\Delta\beta} d\alpha d\beta I(\alpha,\beta)} \tag{2.2}$$

with I(α,β) brightness distribution, α and β sky coordinates, u and v spatial frequencies. $V(u,v)$ is a two-dimensional function in the so-called u,v-plane, where u and v are the spatial frequencies in two perpendicular directions:

$$u = \frac{B_x}{\lambda} \qquad v = \frac{B_y}{\lambda} \tag{2.3}$$

with B_x and B_y orthogonal projections of the baseline vector $\vec{B}$. Due to atmospheric turbulence, however, the phase of this complex number is corrupted and cannot be retrieved. The amplitude of the complex visibility – the visibility – can be measured and is compared to the corresponding quantity of theoretical brightness distributions. For circularly symmetric emission, Equation 2.2 becomes:

$$V(r) = \frac{\int_0^\infty I(\rho) J_0(2\pi\rho r)\rho d\rho}{\int_0^\infty I(\rho) d\rho} \tag{2.4}$$

where:

$$\rho = \sqrt{\alpha^2+\beta^2} \tag{2.5}$$
$$r = \sqrt{u^2+v^2} \tag{2.6}$$

an J_0 the zeroth-order Bessel function of the first kind. Equation 2.4 is also known as the *Hankel transform*.

2.2 Simple brightness distributions

Equation 2.2 gives the relation between the brightness distribution ($I(\alpha,\beta)$) and the complex visibility ($V(u,v)$). We give here some examples of commonly used brightness distribution.

Point source

The simplest example of brightness distribution is the point source:

$$I(\alpha, \beta) = \delta(\alpha - \alpha_0, \beta - \beta_0) \tag{2.7}$$

with $\delta(x)$ Dirac function. In this case the complex visibility is pure phase:

$$V(u, v) = e^{-2\pi i(u\alpha_0 + v\beta_0)} \tag{2.8}$$

and the visibility (norm) is always equal to unity.

Uniform disk

The uniform disk is a first-order approximation of a spherical brightness distribution. The intensity ($I(\rho, \phi)$, ρ and ϕ polar coordinates) is constant and non zero within a radius $\theta/2$ and null outside:

$$I(\rho, \phi) = \begin{cases} I_0 & \rho \leq \theta/2 \\ 0 & \rho > \theta/2 \end{cases} \tag{2.9}$$

Given the azimuthal-symmetry $I(\rho, \phi) = I(\rho)$. Substituting Equation 2.9 in Equation 2.4:

$$V(u, v) = 2\frac{J_1(\pi\theta r)}{(\pi\theta r)} \tag{2.10}$$

with J_1 first-order Bessel function of the first kind.

Uniform ring

From the uniform disk model one can derive the complex visibility of a uniform ring. In polar coordinates the brightness distribution of the uniform ring is:

$$I(\rho) = \begin{cases} 0 & \rho < \theta_{in}/2 \\ I_0 & \theta_{in}/2 \leq \rho \leq \theta_{out}/2 \\ 0 & \rho > \theta_{out}/2 \end{cases} \tag{2.11}$$

with θ_{in} and θ_{out} inner and outer diameters of the ring. Given the linearity property of the Fourier transform, the visibility of the uniform ring is just the difference of the visibility of two uniform disks.

$$V(r) = \frac{2}{\theta_{out}^2 - \theta_{in}^2}\left[\theta_{out}^2 \frac{J_1(\pi\theta_{out} r)}{(\pi\theta_{out} r)} - \theta_{in}^2 \frac{J_1(\pi\theta_{in} r)}{(\pi\theta_{in} r)}\right] \tag{2.12}$$

In the extreme case of an infinitive thin ring with $\theta_{in} = \theta_{out}$, the visibility becomes:

$$V(\theta_{in}) = J_0(\pi\theta_{in} r) \tag{2.13}$$

Multiple components: double uniform ring

We may add a second component to the brightness distribution. If, e.g., both components are uniform rings (double uniform ring model), we have:

$$I(\rho) = \begin{cases} 0 & \rho < \theta_1/2 \\ I_0 & \theta_1/2 \leq \rho \leq \theta_2/2 \\ 0 & \theta_2/2 < \rho < \theta_3/2 \\ I_0 & \theta_3/2 \leq \rho \leq \theta_4/2 \\ 0 & \rho > \theta_4/2 \end{cases} \tag{2.14}$$

with θ_1, θ_2, θ_3 and θ_4 diamaters of the two uniform rings respectively. The visibility of such a model is:

$$V(r) = f_\lambda V_{in}^{UR}(\theta_1, \theta_2) + (1 - f_\lambda) V_{out}^{UR}(\theta_3, \theta_4) \tag{2.15}$$

with V_{in}^{UR} and V_{out}^{UR} visibility of uniform ring (Eq. 2.12) for the inner and outer component respectively and f_λ fractional contribution of the inner component to the total flux at wavelength λ.

Phase offset

In the case of multiple components, not always the different components have the same barycenter of emission (*photocenter*). A relative shift of the photocenter is "visible" in the complex visibility as a phase offset. Let's call V_1 and V_2 the complex visibility of two components, $f = f2/f1$ the flux ratio and $\vec{\rho}$ the separation vector of the two components. The complex visibility is:

$$V(u, v) = \frac{V_1^2 + f^2 V^2 + 2f|V_1||V_2|cos(2\pi/\lambda \vec{B}\vec{\rho})}{(1 + f)^2} \tag{2.16}$$

Inclined morphology

The visibility of a structure inclined by an angle i and rotated by an angle ϕ (position angle of major axis) can be obtained by rotating the u, v coordinates (e.g. Berger & Segransan [16]):

$$u' = u \cdot cos(\phi) + v \cdot sin\phi \tag{2.17}$$

$$v' = -u \cdot sin(\phi) + v \cdot cos\phi \tag{2.18}$$

and by applying a compression factor along the minor axis:

$$r = \sqrt{u'^2 + v'^2 \cdot cos(i)^2} \tag{2.19}$$

2.3 MIDI at VLTI

MIDI [1] (Leinert et al. [96]) is the mid-infrared ($8 - 13\ \mu$m) beam combiner of the *VLT* interferometer on Cerro Paranal, Chile. *MIDI* can combine the light of any pair of the 4 *ESO VLT* telescopes (UT, 8.2m) or the 4 *VLTI* auxiliar telescopes (AT, 1.8m). *MIDI* allows spectrally resolved observations, that is, the signal is dispersed by either a prism ($\Delta\lambda/\lambda \approx 30$) or a grism ($\Delta\lambda/\lambda \approx 300$).

The interferometric signal may be acquired in two modes: *High Sens* and *Sci Phot*. With the first mode, the photometric signal (i.e. the pure, not combined, $8 - 13\ \mu$m spectrum of the source coming from the two telescopes) is acquired soon after the interferometric signal. In *Sci Phot* mode, the two signals are acquired at the same time.

Due to the thermal background of the system, *MIDI* optics are enclosed in a cryostat cooled at 40 K and the *MIDI* detectors are cooled at 10 K. The OPD is time-modulated by dihedral reflectors mounted on a piezo. Each travel of the piezo form an interferogram, or “scan”. Typically, 5 frames per fringe and about 8 fringes per scan are taken. The number of scans varies from ~ 200 to 1000.

---

[1] www.eso.org/instruments/midi

3

The 2003-2006 Outburst of V1647 Orionis: Temporal evolution of the eruptive star

D. Fedele[1,2]***, M. E. van den Ancker***[1]***, M. G. Petr-Gotzens***[1] ***& P. Rafanelli***[2] ***2007, A&A, 472, 207.***
[1] European Southern Observatory, Garching bei München, Germany
[2] Dipartimento di Astronomia, Universitá degli studi di Padova, Padova, Italy

3.1 Introduction

One of the clearest pieces of evidence for disk accretion during early stages of stellar evolution are events like FU Orionis and EX Lupi outbursts (Herbig [64], Hartmann & Kenyon [56]). These outbursts are thought to be the consequence of a sudden and steep increase of the mass accretion rate onto the central star, which changes from those commonly found around T Tauri stars ($\sim 10^{-7}$ $M_\odot$ yr^{-1}) into values of 10^{-3}–10^{-4} $M_\odot$ yr^{-1}. Statistical studies suggest that young low-mass stars experience several FU Orionis-like outbursts during the early phase of stellar evolution. The emergence of a new pre-main-sequence outburst object is thus a unique opportunity to address the physical processes that occur in the disk's interior. For this reason, several astronomers have focused their attention on the recent outburst of V1647 Orionis.

V1647 Ori is a young eruptive star known to be the illuminating source of McNeil's Nebula, a reflecting nebula discovered by the amateur astronomer J.W. McNeil in January 2004 (McNeil et al. [107]). In the months following the discovery, the star, located in the L1630 cloud within the Orion B molecular cloud complex, showed an increase of its optical/IR brightness of up to 6 magnitudes. The outburst has been observed from the X-ray regime (e.g. Grosso et al. [55]) to infrared wavelengths (e.g. Muzerolle et al. [116], Andrews et al. [7]). In February 2004, 4 months after the onset of the outburst, the brightness rise stopped and the magnitude remained (relatively) constant. In November 2005, a communication by Kospal et al. [89] claimed the beginning of a fast fading phase in the optical light of V1647 Ori. The system is further characterized by a red energy distribution and by many emission lines in its optical and near-IR spectrum. Apart from the Brackett series (seen purely in emission), all the Hydrogen lines exhibit a P-Cygni profile, which indicates mass outflow in a wind. Vacca et al. [146] find that their near-IR emission line spectrum is consistent with a dense and ionized wind model where the optically thick H lines are produced. The same model is able to explain why the outburst has not been seen at radio wavelengths (Andrews et al. [7]). V1647 Ori is known to have experienced a previous outburst, as is clear from the appearance of the reflection nebula in 1996–1997 in the atlas of [104] and as recently confirmed by Aspin et al. [9]. Furthermore, its optical and near-IR spectrum does not resemble any other previous spectra of FUors or EXors objects (Reiburth & Aspin [132], Vacca et al. [146]). The 2-3 year duration of the outburst, its recurrence on a timescale of decades and the "peculiar" spectrum of V1647 Ori, are important clues for the comprehension of outburst events in pre-main-sequence stars.

From February 2004 to January 2006 we have followed the evolution of the outburst of V1647 Ori at optical (4700-7300 Å) and mid-IR (8-13 μm) wavelengths. Here, we present the results of our photometric and spectroscopic monitoring of the eruptive source. The analysis of the reflection nebula is presented in a Chapter 4 (Fedele et al. [43], hereafter paper I). Observations and data reduction are described in section 3.2. In section 3.3 we analyze the observations. A discussion of the results is presented in section 3.4. We draw the conclusions in 3.5.

3.2 Observations and data reduction

Observations were performed using FORS2 at ESO's Very Large Telescope in Paranal, Chile and TIMMI2 at the 3.6 m telescope at La Silla. FORS2 [8] is an optical facility (3000-10000 Å) which allows imaging in different bands and grism spectroscopy. TIMMI2 [82] is a mid-infrared (8-14 μm) multi-mode instrument including a low- and medium-resolution spectrograph. We have also included in our analysis some publicly available VLTI/MIDI observations of V1647 Ori taken from the ESO archive[1]. MIDI is the mid-infrared beam-combiner facility of the ESO VLT interferometer (Leinert et al. [96]).

3.2.1 Optical spectroscopy

12 long slit spectra of V1647 Ori were obtained with FORS2 and with the grism 1400V (4560-5860Å, $\lambda/\Delta\lambda \sim 2100$) between 2004 February 18 and 2005 December 27. Seven further long slit spectra were obtained between 2004 December 08 and 2006 January 29, with the grism 1200R (5750-7310Å, $\lambda/\Delta\lambda \sim 2100$). A detailed log of the observations is reported in Table 3.1.

A standard optical long slit spectrum extraction procedure was applied to reduce the raw data - bias subtractions, flat-fielding, wavelength calibration, cosmic rays and sky background removal and weighted average along the spatial axis. Observations of spectro-photometric standard stars during each night allowed us to compute the sensitivity function of the spectrograph. To flux-calibrate the spectra of V1647 Ori, the 1-dimensional extracted spectra were first multiplied by the sensitivity function – to compute the exact slope of the spectrum – and then scaled to the flux level measured from the acquisition images. This is straightforward for the red spectra since the acquisition images were taken with the same filter. For the blue spectra we have assumed $(V - R_C) \sim 1.8 \pm 0.2$ (as measured by McGehee et al. [106] in February-April 2004 and from Kospal et al. [89] in October 2005) from which we computed the absolute V flux level.

Differential aperture photometry of V1647 Ori has been computed over an aperture radius of $2\farcs52$ (10 pixels) from the acquisition images (R_C filter). In Chapter 4 we computed the R_C magnitude of two reference stars in the FORS2 frames which were used to calibrate the instrumental magnitude of the acquisition images discussed here. The two stars were found to be not variable and to have the following R_C magnitude: RA(J2000) = 05:46:09.71; DEC(J2000) = -00:03:31.1; $R_C = 20.08 \pm 0.09$ and RA(J2000) = 05:46:05.88; DEC(J2000) = -00:02:39.7; $R_C = 16.39 \pm 0.02$. The latter corresponds to the comparison star "E" in Semkov [139] and [140], who measured $R_C = 16.39 \pm 0.02$. The results are listed in Table 3.1.

---

[1] *http://www.eso.org/archive*

3.2.2 Mid-IR spectroscopy

TIMMI2

Low-resolution ($\lambda/\Delta\lambda \approx 200$) N'-band (7.7–13.0 μm) spectra of V1647 Ori (IRAS 05436−0007) were obtained on 2004 March 08 (JD 2453072.526) and 2006 January 10 (JD 2453746.663) using the TIMMI2 instrument on the ESO 3.6 m telescope at La Silla. Sky subtraction was achieved by chopping in the North direction with an amplitude of $10''$ followed by a nodding pattern with the opposite direction and amplitude. The total integration time was 25 minutes per spectrum. The slit, with a width of $1.''2$, was centered on a compact source detected in the N'-band acquisition image. A spectrum of the reference star HD 37160 (K0III) was obtained before or after each IRAS 05436−0007 observation. Data were reduced using the usual steps of residual background subtraction, spectral extraction, and wavelength calibration. Correction for the telluric ozone absorption bands, as well as absolute flux calibration, were achieved by ratio-ing the IRAS 05436−0007 spectrum to that of HD 37160, flux-calibrated using the spectral templates by Cohen et al. [30]. The resulting spectra are shown in Fig. 3.6.

VLTI/MIDI

We also analyzed interferometric observations of V1647 Ori obtained with VLTI/MIDI on 3 nights between 2004 December 30 and 2005 March 01. The interferometric data were previously analyzed by Abraham et al. [2]. Hence we will discuss here only the MIDI low-resolution (R=30) spectrum acquired on each night by the instrument after the interferometric observation. Using the MIA+EWS-1.3[2] software package, a fixed mask was applied to the MIDI chopped spectrum. The background was estimated from the off-source (sky) frames and then subtracted from the on-source frames. The one-dimensional spectrum was extracted. In the same way, spectra of MIDI calibrator stars were extracted.

Aperture photometry was computed from the acquisition images with a narrow filter centered at 8.7 μm adopting a fixed aperture of 12 pixel ($1.''0$). The throughput of the two MIDI channels are, for an unknown reason, different, and the aperture photometry differs for the two telescopes. We used the results from channel B which tend to be the more stable of the two. Conversion factors from counts to Jy were computed from the MIDI calibrators, whose 8.7 μm flux were evaluated from theoretical spectral energy distributions.

---

[2] *http://www.strw.leidenuniv.nl/ koehler/MIA+EWS-Manual*

Table 3.1: Log of spectroscopic observations with FORS2 of V1647 Ori.

Date (UT)	JD -2 450 000	FWHM ($''$)	Slit width ($''$)	Slit PA (°)	Spectral range (Å)	Exposure time (sec)	S/N	R_C (mag)
2004-02-18	3053.081	0.85	1.0	45.0	4560-5860	700	20	17.39 ± 0.10
2004-02-23	3058.090	1.25	1.0	45.0	4560-5860	700	19	17.31 ± 0.10
2004-03-13	3077.018	0.9	1.0	45.0	4560-5860	700	14	17.52 ± 0.10
2004-03-18	3082.011	1.15	1.0	45.0	4560-5860	700	13	17.42 ± 0.10
2004-03-27	3091.020	0.9	1.0	45.0	4560-5860	700	14	17.31 ± 0.10
2004-12-08	3347.315	1.2	0.7	90.0	4560-5860	500	9	17.23 ± 0.05
2004-12-21	3360.251	0.65	0.7	90.0	4560-5860	500	14	16.87 ± 0.05
2005-01-05	3375.180	1.35	0.7	90.0	4560-5860	500	10	17.07 ± 0.05
2005-02-18	3419.126	1.0	0.7	90.0	4560-5860	500	4	17.77 ± 0.05
2005-02-29	3430.114	0.65	0.7	90.0	4560-5860	500	9	17.12 ± 0.05
2005-03-15	3444.045	0.72	0.7	90.0	4560-5860	500	7	17.50 ± 0.05
2005-12-27	3731.215	1.33	0.7	90.0	4560-5860	4 x 1800	2	20.74 ± 0.11
2004-12-08	3347.322	1.15	0.7	90.0	5750-7310	500	20	17.23 ± 0.05
2004-12-21	3360.258	0.68	0.7	90.0	5750-7310	500	42	16.87 ± 0.05
2005-01-05	3375.187	1.08	0.7	90.0	5750-7310	500	26	17.07 ± 0.05
2005-02-18	3419.133	1.12	0.7	90.0	5750-7310	500	15	17.77 ± 0.05
2005-02-29	3430.121	0.62	0.7	90.0	5750-7310	500	23	17.12 ± 0.05
2005-03-15	3444.052	0.69	0.7	90.0	5750-7310	500	22	17.50 ± 0.05
2006-01-29	3764.122	0.73	0.7	90.0	5750-7310	4 x 1800	4	22.05 ± 0.11

Energy distributions were derived from the Cohen list [30] of infrared standard stars for the calibrator HD 37160 ($F_{8.7\mu m}$ = 11.5 Jy), and by matching the spectral type of the calibrator to stars in the Cohen list and scaling the spectrum by the ratio of their IRAS 12 micron fluxes for HD 107446 ($F_{8.7\mu m}$ = 37.9 Jy) and HD 50778 ($F_{8.7\mu m}$ = 28.9 Jy). The three calibrators were also used to compute the sensitivity function of MIDI (wavelength dependence of the instrument's response). The spectrum of V1647 Ori has been flux calibrated by multiplying it by the sensitivity function and by scaling it in order to match the 8.7 μm flux. The result is shown in Figure 3.6.

3.3 Results

3.3.1 Optical lightcurve

Figure 3.1 shows the light curve of V1647 Ori in the R_C band based on the data of Table 3.1 and on previous measurements by other authors. Due to the influence of McNeil's nebula on the computation of the stellar flux and subtraction of local background, measurements with different instruments may result in a different magnitude estimation. In particular, given the better spatial resolution of our data, we may better disentangle the contribution from V1647 Ori from that of the nebula. For this reason, an offset of -0.3 mag was applied to R_C measurements by other authors. Such an offset is not needed for the data of Acosta-Pulido et al. [6]. Three further R_C measurements from Chapter 4 are plotted in Figure 3.1.

Since measurements of R_C of the early outburst are not available in the literature, we estimated R_C from I_C measurements of Briceño et al. [21]. The $(R_C - I_C)$ color, as measured by various authors (McGehee et al. [106], Ojha et al. [124]), seems reasonably stable during the plateau and the fading phase, showing $(R_C - I_C) \approx 2.0$ with a scatter of 0.2 mag. With this we calculate the expected R_C magnitudes for the period October 2003 – February 2004 from the I_C measurements, assuming the same $(R_C - I_C)$ color for the rising phase. From Fig. 3.1, the optical light curve of V1647 Ori can be divided in three parts: i) from October 2003 to February 2004 – the rising period; ii) from February 2004 to August 2005 – the *plateau* phase and iii) from August 2005 to January 2006 – the fading period.

The rising part is very steep: from October 2003 to January 2004 the optical magnitude increased by more than 3 magnitudes in R_C. From the pre-outburst magnitude level, $R_C \sim 23.5$, computed by McGehee et al (inset in Fig. 3.1) total rise in brightness of V1647 Ori is > 6 mag in R_C. From the light curve in Fig. 3.1 we find a rate of increase of R_C of ~ 1.5 mag/month. Assuming that this rate remained constant during all the rising phase, we estimate that the outburst began around the middle of August 2003, slightly earlier than October-November 2003 as found by Briceño et al. [21].

During the *plateau* phase the optical brightness shows a slow decline with time ($\Delta R_C = 0.02$mag/month), on top of which R_C displays a non-periodic, flickered, oscillation on a short timescale. The light curve in Fig. 3.1 combines data from different works which have used different instruments and aperture sizes. This may result in a systematic scatter of the data from work to work. However, an intrinsic variation of the optical brightness on short time scales is clearly present. From our data we measure a variation of ~ 0.5 mag between 2004 Feb. 17 ($R_C = 16.90 \pm 0.05$, Chapter 4) and Feb. 18 ($R_C = 17.39 \pm 0.10$, Table 3.1). Thus, V1647 Ori at its maximum light shows an optical brightness variation on a time scale of 24 hours. For five nights we have two consecutive acquisition images (separated by a few minutes) from which we searched for even smaller time scale variations of R_C, however, no significant changes in optical brightness ($\Delta R_C > 0.1$ mag) are detectable from these measurements. The short timescale variability is of the same order as that found by other authors in the optical and near infrared (Ojha et al. [124], Walter et al. [153]) on a timescale of a week. The total duration of the *plateau* phase is less than 2 years.

Our photometry confirms the rapid brightness decrease announced by Kospal et al. [89]. Four months after the claimed onset of the fading phase (August 2005, when Orion reappeared in the sky, however from the light curve it is clear that it started before), the brightness of V1647 Ori was still diminishing. From August 2005 to January 2006 R_C dropped by 4 mag. On 2006 January

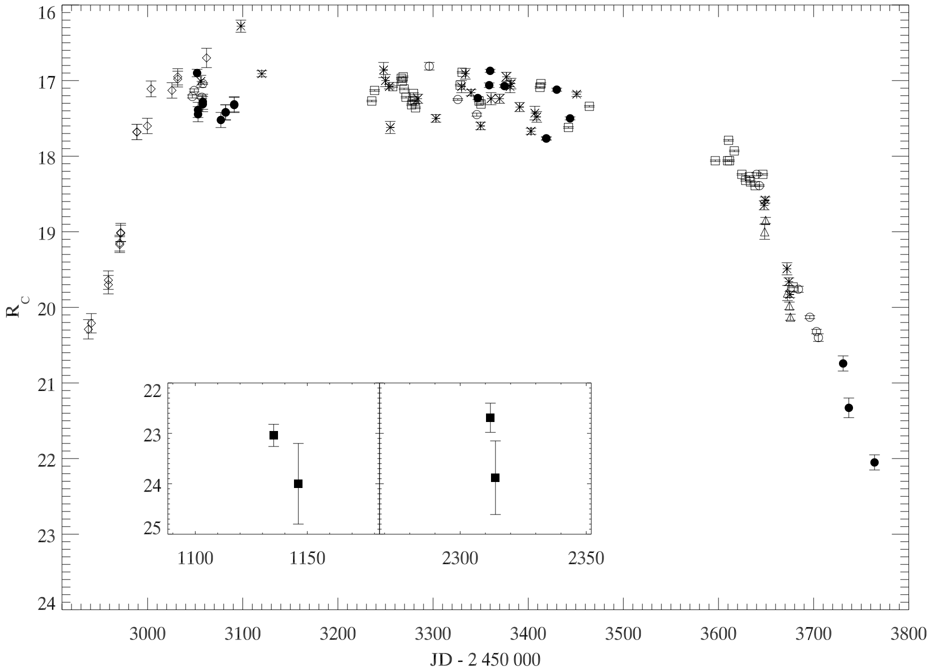

Figure 3.1: Optical, R_C, light curve of V1647 Ori. Data are from: filled circles this work; squares Semkov, E.H. [140], [139]; triangles Kospal et al. [89]; stars Acosta-Pulido et al. [6]; diamonds Briceño et al. [21]; filled squares McGehee et al. [106]; open circles Ojha et al. [124]. An offset of -0.3 mag was applied to the imported data (apart from those of [6]) in order to reach a similar magnitude level as our data. In the inset the pre-outburst magnitude level reported by McGehee et al. [106] is shown.

29, the last R_C measurements, we estimate $R_C = 22.05 \pm 0.11$ which is still more than 1 magnitude above the pre-outburst level of McGehee et al. [106]. From the light curve we estimate a fading rate of ~ 0.8 mag/month during this phase. Assuming a constant fading rate, R_C reached the pre-outburst level at the beginning of April 2006.

The light curve is not symmetric; the rising and fading phase have a different slope. From the two different rates we infer that the physical process which led to the beginning of the outburst is not simply the reverse of the process ending this outburst. The rates of brightness variation during the three phases are in agreement with those found by Acosta-Pulido et al. [6].

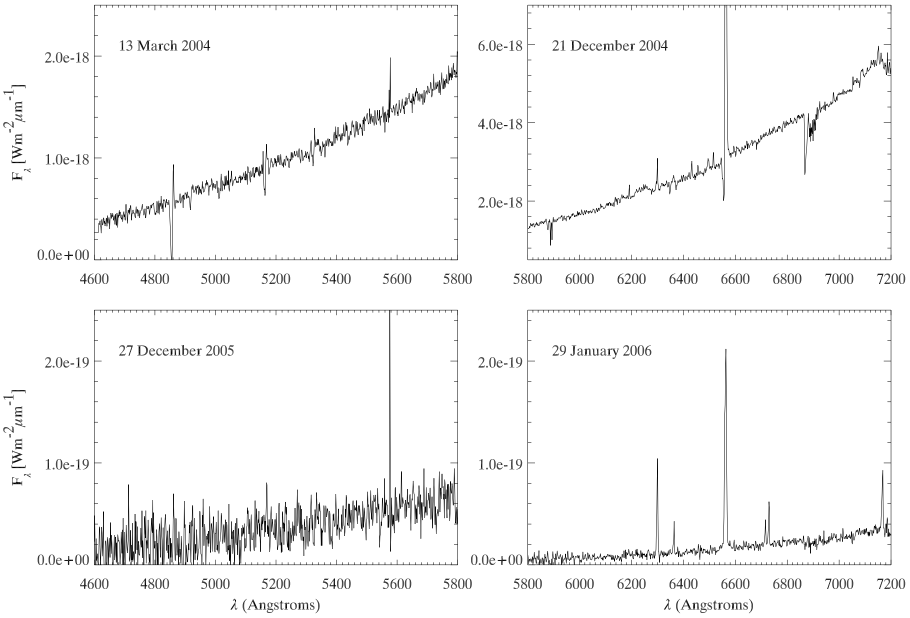

Figure 3.2: Examples of optical spectra of V1647 Ori obtained during the *plateau* phase (top two panels), and during the fading phase (bottom two panels). *Plateau spectrum*: the Hα and Hβ are clearly visibile with a P-Cygni profile, Fe I (5328, 6191, 6495 Å) and Fe II (5169, 6432, 6516 Å) lines and absorption from Na I D1 & D2 (5889, 5895 Å) and He I line (5875 Å). A residual of the data reduction is present at [O I] (6300, 5577 Å) due to bad pixel columns, and between 6870 - 6910 Å due to a non-perfect removal of telluric absorption. *Fading phase spectrum*: no lines are detected in the blue part ([O I] 5577 Å is a residual of the data reduction), while the red part is characterized by strong emission of Hα, [O I] 6300, 6363 Å, [S II] 6717, 6731 Å and [Fe II] 7172 Å.

3.3.2 Optical spectra

The positive slope of the optical spectrum of V1647 Ori (fig. 3.2) reveals a red energy distribution of the source. Clearly visible are the Hα and Hβ lines both characterized by a P-Cygni profile. The He I λ5875, Na I D1 & D2 doublet in absorption and Fe I and Fe II lines in emission (P-Cygni) are detected in the spectra taken during the *plateau* phase. Due to bad pixel columns at [O I] λ5577 and [O 1] λ6300 lines a residual of the data reduction is present in the spectra taken during the *plateau* phase. For this reason we cannot find evidence of any source features at these wavelengths.

During the *plateau* phase the optical spectrum shows only minor changes in equivalent width and line flux (discussion below). The overall shape of the spectrum remains “constant” during this period. The spectrum taken during the fading phase (blue – 2005 December 27, red – 2006 January 29, Fig. 3.2) is different to all the others: superimposed on a very faint continuum with a slightly positive slope there are very strong emission lines corrisponding to Hα, [O I] $\lambda\lambda$6300,6363, [S II] $\lambda\lambda$6717,6731 and [Fe II] at 7172 Å . The sky line [O I] λ5577 is saturated and it is not possible to find evidence of source emission at this wavelength.

From the flux-calibrated spectra, for each line detected, we computed the equivalent width (EW) and the line flux (F_l) multiplying EW by the continuum level at the line center (Tables 3.3 & 3.4). A major source of uncertainties in this computation is the determination of the continuum level, which in turn depends on the accuracy of the sensitivity function and of the aperture photometry from the acquisition images. The final accuracy is of the order of 10% on EW and of 15% on F_l.

The P-Cygni profile of Hα and Hβ is in both cases asymmetric with the emission components lacking the high velocity part (Figures 3.3, 3.4). This profile results from the deviation of the spherically-symmetric wind and is observed in FU Ori objects and T Tauri stars and can be explained by the presence of an opaque disk which occults part of the redshifted emission (e.g. Hartmann [61]). The profiles of the two lines differ significantly (figures 3.3 & 3.4): the Hβ has a strong and wide absorption and a “weak” narrow emission while the Hα has a large emission and a weak absorption. In both cases, the blue-shifted absorption shows at least two components: one at $\sim$ –450 km s^{-1}, and the other at $\sim$ – 150 km s^{-1}. While the low velocity component remains almost constant over all the *plateau* phase, the high velocity one is variable. In particular, the latter shows in both lines a progressive decrease in extension from February 2004 to March 2005 until the whole absorption disappears in the fading phase spectrum. Furthermore, on three nights (2005 January 05, February 18 and March 15) the bluest absorption component of the Hα is “replaced” by an emission. The emission component also varies from night to night, displaying a change in equivalent width and line flux.

P Cygni signatures are also displayed by Fe lines. However, due to the low S/N of the spectra, the absorption component is clearly detected only for the Fe II λ5169.08 transition. The maximum absorption is at $\sim$ – 370 km s^{-1} and has a terminal velocity of $\sim$ – 600 km s^{-1}. The other Fe emission lines show variation in equivalent width and line flux with time.

Thus, similar to what we have found for the continuum emission (R_C magnitude), the emission lines vary on time scales of months and weeks. If continuum and line emission are produced in the same region, then the flux of a generic emission line (F_l) is linearly proportional to continuum flux (F_R – R_C bandpass flux). In Fig. 3.5 we plotted the line flux of the strongest emission lines detected (Hα and Hβ) versus F$_R$. Arrows indicate upper limits. Assuming a power law dependence of the line emission from F$_R$ ($F_l \propto F_R^\gamma$) we searched for a correlation between line and continuum emission. The continuous line in figure 3.5 is the best fit to the data. We find $\gamma_{H\alpha} = 0.8$ and $\gamma_{H\beta} = 0.7$. The Hα best fit is more robust than the Hβ one (the Hα emission is much stronger and it is also detected during the fading phase). All the other emission lines detected are weak and strongly affected by the low S/N of the spectra. The power law model fit in this case is more uncertain and clear evidence of dependence of the line emission from the continuum emission cannot be found. The value of γ found for the H Balmer lines is close to unity. This means that the variation in line flux is correlated to the variation of the continuum emission. This evidence might suggest that the two emissions arise from the same region of the system, or at least, that the emission mechanisms are physically linked. Contrary to what was found by Acosta-Pulido et al. [6], we do not find any clear trend of the Balmer emission lines with time during the *plateau* phase. Both the EW and the line flux show a random variation with time in this period.

For the first time we detected optical forbidden lines in the spectrum of V1647 Ori taken during the fading phase (Fig. 3.2, bottom right). The spectrum clearly shows strong emission from [O I] $\lambda\lambda$6300,6363, [S II] $\lambda\lambda$6717,6731, [Fe II] λ7172 an Hα. These lines provide evidence for hot (a few thousand K) gas close to V1647 Ori. These are used as tracers of Herbig-Haro objects where a collimated jet from the central star collides with the ambient medium. The emission is produced by the cooling of the shocked gas. Eislöffel & Mundt [40] identified IRAS05436-0007 as the driving source of HH 23.

Similar and perhaps newly formed ejecta could be responsible for the forbidden emission lines seen here. None of these forbidden lines were previously detected in the *plateau* spectrum, most likely because of the overwhelming continuum.

3.3.3 Mid-Infrared spectra

The rise in brightness of V1647 Ori during the outburst has also been seen by others authors also at longer wavelengths (e.g. Andrews et al. [7], Muzerolle et al. [116], Abraham et al. [2]) . Our TIMMI2 spectra (Fig. 3.6) confirm the increased mid-infrared flux: from the pre-outburst level of 0.53 Jy at 12 μm (IRAS, Point Source Catalog) up to 7.6 Jy on 2004 March 08. The $8 - 14\mu$m spectrum is essentially featureless and flat all along the spectral range.

Table 3.2: Mid-infrared photometry of V1647 Ori from TIMMI2 and MIDI data. For comparison in column 3 and 4 we report the corresponding R_C magnitude and the R_C - N1 color, where N1 is the magnitude at 8μm converted to the ESO mid infrared photometric system [151].

DATE	$F_{8\mu m}$ [Jy]	R_C [mag]	R_C - $N1$ [mag]	Ref.
2004-03-07	6.4	16.8	14.4	Muzerolle et al.[116]
2004-03-08	6.5	16.8	14.4	this work (TIMMI2)
2004-03-11	4.3	16.8	14.0	Andrews et al. [7]
2004-12-31	2.3	16.7	13.2	this work (MIDI)
2005-01-03	2.5	16.7	13.3	this work (MIDI)
2005-02-21	2.3	17.1	13.5	this work (MIDI)
2005-03-01	2.5	17.2	13.7	this work (MIDI)
2006-01-10	0.5	21.0	15.8	this work (TIMMI2)

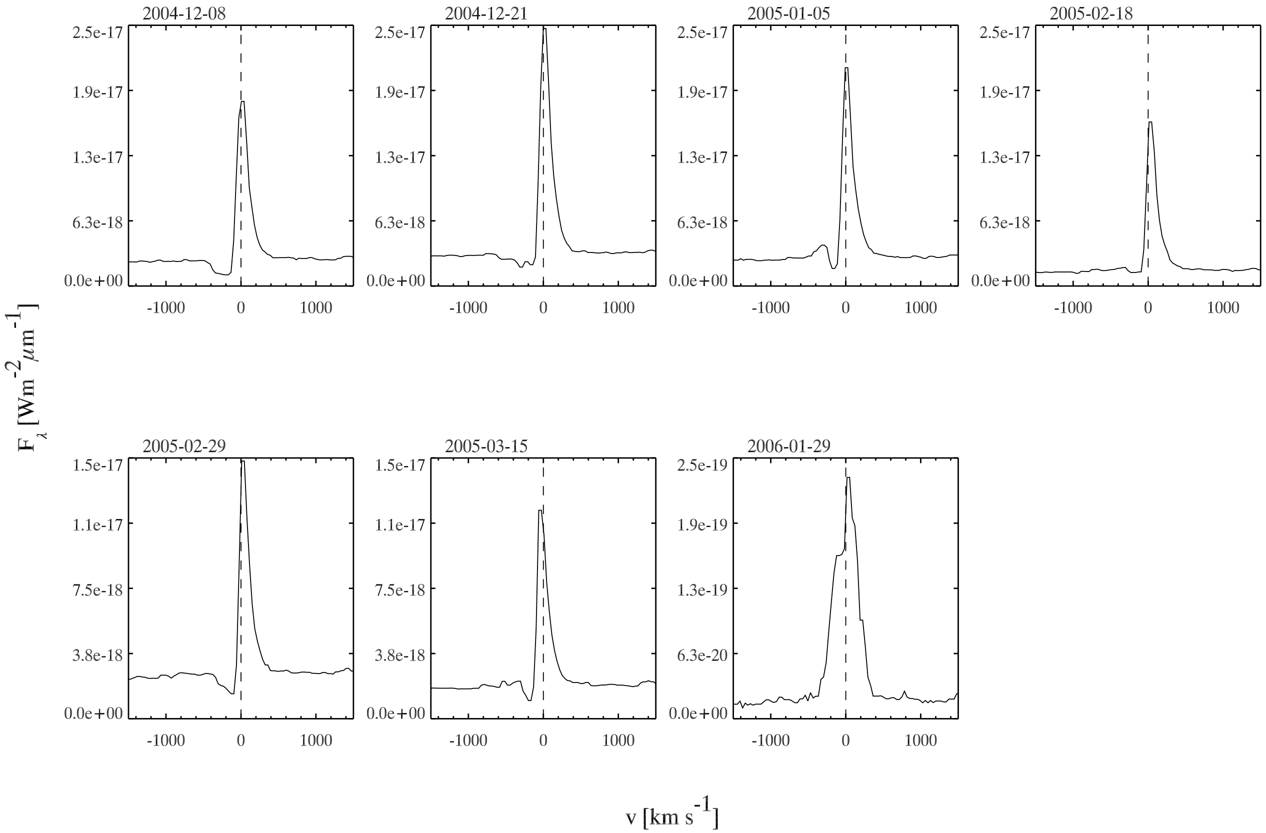

Figure 3.3: Time evolution of the Hα emission in the period December 2004 - January 2006. In all the "*plateau* spectra" the line has an asymmetric P-Cygni profile. In the "fading phase spectrum", the line is pure in emission with no trace of absorption.

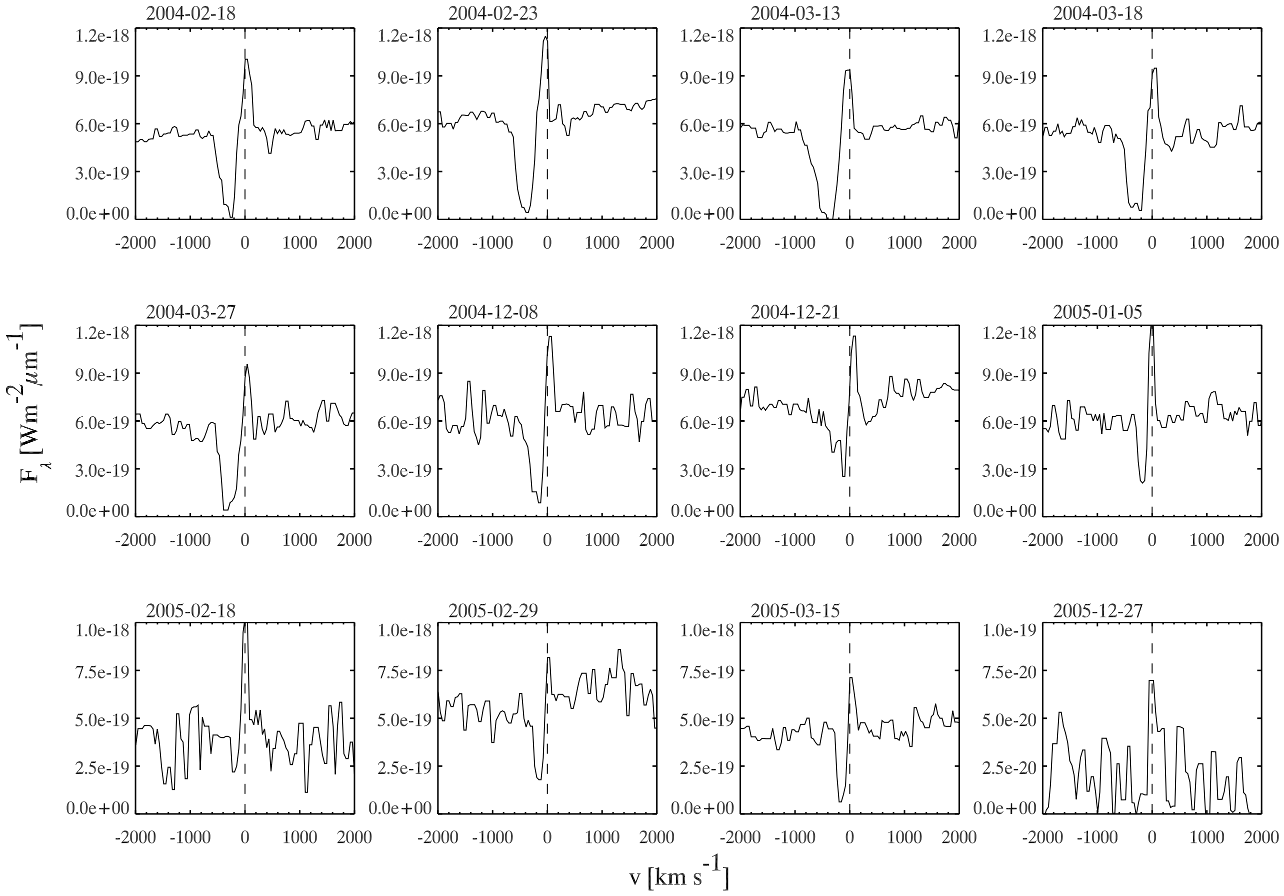

Figure 3.4: Time evolution of the Hβ emission in the period February 2004 - December 2005. As for the Hα, during the *plateau* phase the line has a P-Cygni profile. No Hβ emission is detected in the low S/N "fading phase spectrum".

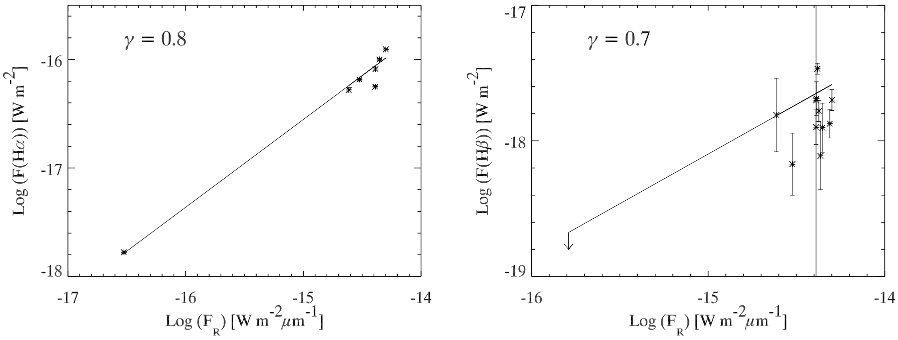

Figure 3.5: Line flux of Hα and Hβ versus continuum flux. The best power law fit is over-plotted.

This result is not consistent with the mid-infrared spectrum in Andrews et al. [7] taken with UKIRT/Michelle only three days after our TIMMI2 spectrum. Their measurement reveals a strong red energy distribution with the flux going from 4.0 Jy at 8 μm up to 12.0 Jy at 12μm. Our estimate of the mid-infrared flux is however consistent with the SPITZER/IRAC observations of Muzerolle et al. [116] taken on 2004 March 07. They measure a flux of 6.43 Jy at 8 μm, very close to our estimate. A residual of the data reduction corresponding to the strong atmospheric absorption bands centered at 9.6 (0_3) and 12.55 μm (CO_2) do not allow us to better analyze these two regions.

Ten months later, in December 2004, the mid-infrared flux of V1647 Ori revealed by the MIDI observations dropped by a few Jy. The spectrum is again flat and featureless. The MIDI spectra analyzed were all taken during the optical *plateau* phase (Fig. 3.6). They all reveal a flat and featureless spectrum. Within the accuracy of these spectra (10%), the flux level remains constant between December 2004 and March 2005. Thus, also in mid-IR the system experienced a *plateau* phase.

The rapid optical brightness fading is also experienced by the system in the mid-infrared: on 2006 January 11, the flux level of our TIMMI2 spectrum at 12 μm is 0.9 Jy, still considerably higher than the pre-outburst level. Also in this case the spectrum is flat and featureless.

The optical and mid-IR light curve of V1647 Ori are different. In the optical the brightness increases during the rising phase, remaining below the value of the *plateau* phase and finally decreases. On the other hand, the mid-IR brightness is higher during the "mid-IR rising phase" than during the "mid-IR *plateau* phase" (Fig. 3.7).

3.4 Discussion

Pre-main-sequence stars are known to be intrinsically variable objects. The variability mechanisms might be different: solar-like coronal activity, spots on the stellar surface, stellar pulsation, partial obscuration and subsequent clearing of the line of sight. These processes are however unable to generate the $\sim 44\ L_{\odot}$ luminosity increment produced by V1647 Ori and to produce the $\gtrsim 6$ optical magnitude burst lasting more than 2 years. To release such an amount of energy the existence of a secondary luminosity source is necessary. Similar brightening events from FU Orionis stars are explained by a sudden increase of the mass accretion rate from a circumstellar disk onto the central star. The increased accretion rate produces an accretion luminosity ($L_{acc} \propto \dot{M}$) which may overwhelm the stellar brightness. Such a process can explain both the dramatic brightening (from X-ray to the infrared) as well as the strong Hα emission observed in the recent outburst of V1647 Ori. Kastner et al. [80] confirmed that the X-ray evolution of V1647 Ori in outburst reflects the near-infrared evolution and is consistent with the hypothesis of an increased mass accretion rate. As a consequence of the enhanced accretion rate a strong wind develops from the disk's surface. The blue-shifted absorption components of Hα and Hβ in the spectrum of V1647 Ori are signatures of this wind. The disappearance of the absorption component in Hα during the fading phase is a confirmation that the strong wind ceased and that the system has been going back to a phase of slow accretion. In this system the origin of the H Balmer emission lines is controversial since both the wind and the mass infall might contribute to the line formation. The magnetospheric accretion predicts a further contribution to the line emissivity produced in the optically thin free-falling accretion columns.

The Fe II lines at 6432.68 and 6516.81 Å detected in the spectra of V1647 Ori both originate from multiplet 40. They are commonly also seen in emission in the spectra of strongly accreting young stars such as V380 Ori (Rossi [134]; Shevchenko [137]), Z CMa (Hessman et al. [66]; Garcia et al. [46]; van den Ancker et al. [149]), PV Cep and MWC 1080 (Hernandez et al. [65]) and are amongst the strongest emission lines in such environments. These Fe II lines appear to be absent from the spectrum of young stars showing lower accretion rates.

Table 3.3: Lines detected in the blue spectra of V1647 Ori between February 2004 and December 2005. EW is negative for emission lines and positive for absorption lines. In case of emission lines also the line flux is reported; EW are expressed in Å and line flux in 10^{-18}W m^{-2}. The accuracy on equivalent width and line flux is of the order of 10% and 15%.

Ident.	λ[Å]	2004-02-18		2004-02-23		2004-03-13		2004-03-18	
		EW	F_{line}	EW	F_{line}	EW	F_{line}	EW	F_{line}
Hβ(em)	4861	-2.91	1.6	-1.94	1.34	-5.38	3.12	-2.22	1.26
Hβ(ab)		5.45		5.91		11.48		5.68	
Fe II(em)	5169	-0.58	0.51	-0.17	0.18	-1.68	1.52	-0.37	0.32
Fe II(ab)		0.74		1.04		2.16		0.98	
Fe I	5328	>-0.7	<0.78	-0.32	0.39	-0.36	0.39	>-0.6	<0.7

Ident.	λ[Å]	2004-03-27		2004-12-08		2004-12-21		2005-01-05	
		EW	F_{line}	EW	F_{line}	EW	F_{line}	EW	F_{line}
Hβ(em)	4861	-1.22	0.75	-3.33	2.08	-2.75	2.02	-2.00	1.27
Hβ(ab)		5.53		5.23		6.05		2.15	
Fe II(em)	5169	>-1.2	<1.2	-0.70	0.62	-0.49	0.53	>-1.3	<1.2
Fe II(ab)		1.34		<1.9		<1.2		0.59	
Fe I	5328	-0.30	0.34	>-1.1	<1.2	-0.29	0.38	-0.54	0.62

Ident.	λ[Å]	2005-02-18		2005-02-29		2005-03-15		2005-12-27	
		EW	F_{line}	EW	F_{line}	EW	F_{line}	EW	F_{line}
Hβ(em)	4861	-4.22	1.53	>-1.5	<0.94	-1.61	0.70	>-11.1	< 0.2
Hβ(ab)		<6.2		2.55		2.83		<22.1	
Fe II(em)	5169	>-2.7	<1.5	>-1.2	<1.1	>-1.1	<0.8	>-4.9	<0.2
Fe II(ab)		<4.1		<1.9		<1.7		< 7.3	
Fe I	5328	>-2.2	<1.4	>0.8	<0.8	>-1.3	<1.0	>-4.5	<0.2

Table 3.4: Continuation of table 3.3 for red spectra between December 2004 and January 2006.

Ident.	λ[Å]	2004-12-08		2004-12-21		2005-01-05		2005-02-18		2005-02-29		2005-03-15		2006-01-29	
		EW	F_{line}	EW	F_{line}	EW	F_{line}	EW	F_{line}	EW	F_{line}	EW	F_{line}	EW	F_{line}
He I	5875	1.14		0.71		0.32		<1.6		<0.8		<1.1		<10.9	
Na I (D1)	5889	1.44		0.97		2.26		2.82		1.87		1.16		<9.1	
Na I (D2)	5895	1.01		0.70		1.17		2.88		0.87		1.51		<7.3	
Fe I (169)	6191	-0.31	0.54	-0.35	-0.74	-0.34	0.63	>0.1	<0.8	-0.24	0.44	-0.30	0.38	>-3.3	<0.03
[OI]	6300	–	–	–	–	–	–	–	–	–	–	–	–	-40.98	0.42
[OI]	6363	–	–	–	–	–	–	–	–	–	–	–	–	-6.92	0.08
Fe II	6432	-0.74	1.58	-0.44	1.17	-0.45	1.03	-0.48	0.58	-0.42	0.94	-0.54	0.85	>-2.7	<0.03
Fe I	6495	-1.08	2.46	-0.55	1.54	-0.73	1.76	-0.83	1.08	-0.52	1.23	-0.92	1.59	>-2.7	<0.03
Fe II	6516	-0.55	1.27	-0.43	1.24	-0.53	1.30	-0.69	0.93	-0.35	0.85	-0.52	0.92	>-2.7	<0.03
Hα(em)	6562	-26.6	66.3	-28.7	88.7	-30.3	80.4	-38.8	56.6	-17.3	44.7	-22.1	39.9	-108.3	1.66
Hα(ab)		3.30		2.55		0.74		<0.5		1.78		1.10		<3.9	
[SII]	6717	–	–	–	–	–	–	–	–	–	–	–	–	-4.52	0.09
[SII]	6731	–	–	–	–	–	–	–	–	–	–	–	–	-7.24	0.15
[FeII]	7172	–	–	–	–	–	–	–	–	–	–	–	–	-9.48	0.32

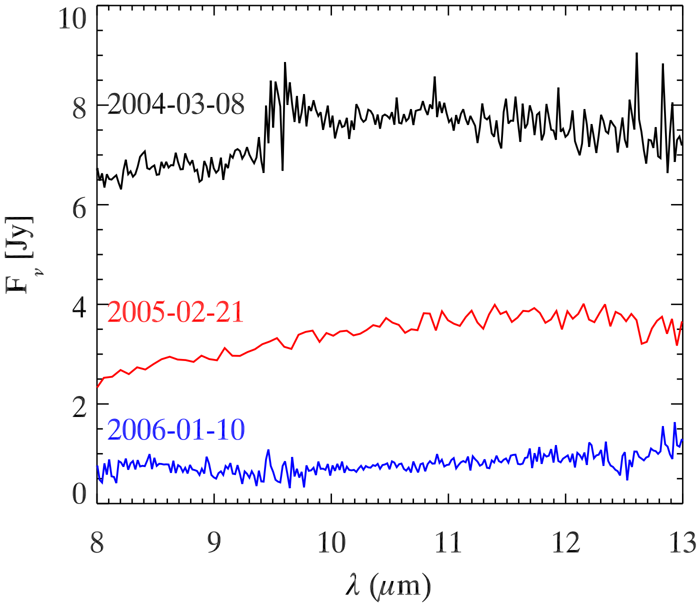

Figure 3.6: Time evolution of the mid-Infrared spectrum of V1647 Ori taken with TIMMI2 (black and blue lines) and MIDI (red line). The mid-infrared spectrum measured by MIDI remain constant, within the uncertainties (10%), between December 2004 and March 2005. Here, only the MIDI spectrum taken on 2005 February 21 is shown.

The presence of Fe I 6495.81 emission and the absence of strong Fe II lines from higher multiplets suggests that the iron-line forming region in V1647 Ori may be somewhat cooler than the typical electron temperatures of 10,000-20,000 K inferred in for example Z CMa (van den Ancker et al. [149]).

3.4.1 The circumstellar envelope and the puzzling mid infrared spectrum

The accretion disk alone is not able to produce the long wavelength ($\lambda \gtrsim 10$ μm) emission observed, unless it flares strongly over a large range of distance scales (e.g. Hartmann [61]). The sub-millimeter continuum flux during the outburst remains at its pre-outburst level and there are no signatures of flux changes in these wavelength regimes (Andrews et al. [7]). These findings are consistent with the presence of a dusty circumstellar envelope, probably a remnant of the infalling envelope. Intriguingly, Kenyon & Hartmann [85]

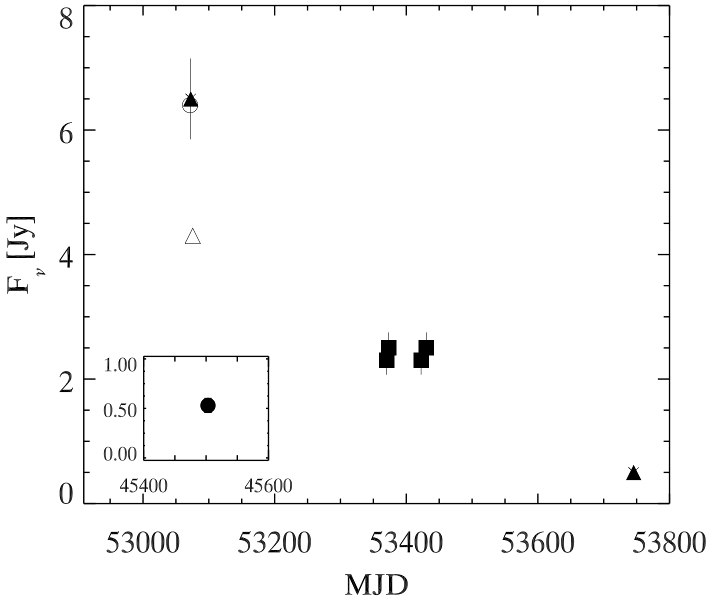

Figure 3.7: 8 μm light curve of V1647 Ori. Filled triangles - TIMMI2 data; filled squares - MIDI data; open circle - SPITZER/IRAC data from Muzerolle et al. [116]; open triangle - UKIRT/MICHELLE data from Andrews et al. [7]. The inset shows the pre-outburst IRAS measurements at 12 μm.

suggested the presence of the infalling envelope to explain the enhanced mid-infrared flux from FU Orionis objects in the eruptive phase.

Muzerolle et al. ([116], hereafter M04) attempt to reproduce the spectral energy distribution (SED) of V1647 Ori by means of a standard viscous accretion disk and of an optically thin envelope. Their model predicts a 10μm emission feature that is produced by silicate dust grains. However, our multi-epoch mid-infrared spectroscopy reveals a flat and featureless spectrum during the whole outburst duration (Fig. 3.6). This is highly unusual. In FU Orionis objects the silicate feature is seen sometimes in emission (V1057 Cyg, FU Ori, BBW 76, V1515 Cyg, Green et al. [54]) and sometimes in absorption (V346 Nor, Z CMA Green et al. [54], Acke & van den Ancker [3]). These differences are probably caused by differences in the optical thickness of the system (disk + envelope) at 10 μm.

The model proposed by Abraham et al. [2] adopts a simple viscous accretion disk model (without envelope). Their model predicts a flat and featureless mid infrared spectrum. However, the emission at longer wavelength ($\gtrsim 10\mu m$) requires an highly flared disk. In such a model the outer part of the disk is directly illuminated during the outburst producing a flux enhancement also in the (sub-)millimeter. This is not observed (Andrews et al. [7]). The stability of the (sub-)millimeter emission favors the presence of a dusty circumstellar envelope.

The excitation plot for the CO fundamental ro-vibrational lines (Rettig et al. [133]) and the detection of $\Delta v = 2$ CO band heads at $\sim 2.3\ \mu m$ (Vacca et al. [146]) indicate the presence of hot ($\sim$ 2500 K) and dense gas. Since the dust sublimes at $\sim$ 1500 K, such emission likely arises in regions free of dust. Our suggestion is that even in the mid infrared the bulk of the emission is produced by the gas in a dust-free region of the disk. Nevertheless we cannot exclude a contribution from the dust (e.g arising at larger radii in the disk). The emission at longer wavelengths is dominated by the dust in the envelope.

Fig. 3.7 shows the temporal evolution of the mid infrared flux during the outburst. The flux decay at these wavelengths is faster than the decay in the optical (compare with Fig. 3.1). The 8-14 μm flux drastically decreases from March to December 2004 while the optical continuum remains constant over the same period. This produces radical changes in the SED of V1647 Ori during the outburst. As can be seen from the R_C - N1 color (Table 3.2) the system is redder during the early outburst. A likely explanation is that in the earlier phases of the outburst the disk was hotter and a larger region of the disk contributed to the emission seen at 10 μm. However, a detailed modeling of the observations is necessary to explain which parameters (such as temperature, opacity, surface area) are responsible for the observed changes.

3.5 Conclusion

Outbursts in pre-main-sequence stars historically have been classified in two main groups based upon their similarity to the prototypes FU Orionis and EX Lupi (Herbig [64]) depending on outburst duration, maximum magnitude variation and spectral features at maximum light. Table 3.5 lists the main characteristics of the two groups and that of V1647 Ori.

Since the onset of the outburst of V1647 Ori it has been debated whether this system is either as FUor or an EXor object. V1647 Ori resembles some aspects of an EXor (outburst duration, recurrence of the outburst), and some aspects of an FUor (magnitude rise, SED). However the recurrence timescale of the outburst has an intermediate value between the two classes. Its emission line spectrum is clearly distinct from either the absorption line spectrum of an FUor or the T Tauri-like spectrum of an EXor (where the H lines show as inverse P-Cygni profile).

V1647 Orionis is not the only outburst PMS suspected of having a nature intermediate between the two main classes. OO Ser recently experienced an outburst that lasted ∼ 5-10 years (Kospal et al. [90]), too fast for an FUor and too slow for an EXor. The SED of OO Ser is typical of an FU Orionis object, and has roughly the same shape in quiescent and outburst phase.

A common denominator in all young eruptive stars detected so far seems to be the presence of circumstellar material as well as that of a reflection nebula. These structures are likely remnants of the infalling envelope. The infalling envelope is a potential reservoir of mass for the disk which experiences recursive outbursts. Assuming that L_{bol} during the outburst is dominated by the accretion luminosity, M04 estimate a mass accretion rate of $\sim 10^{-5}$ $M_{\odot}yr^{-1}$. Considering the 2-3 year duration of the outburst and the 37 year recurrence timescale, a constant envelope infall rate of $\sim 7{\cdot}10^{-7}$ $M_{\odot}yr^{-1}$ is necessary to replenish the disk after each outburst. The disk accretion rate during the quiescent phase is estimated to be $\sim 6{\cdot}10^{-7}$ $M_{\odot}yr^{-1}$ (e.g. M04).

Submillimeter maps reveal that FU Orionis stars have accretion disks that are larger and more massive than those of T Tauri stars (Sandell & Weintraub [136]) and are comparable in mass to those seen around Class I sources (i.e. young stellar objects with flat or rising infrared SED). The circumstellar material around V1647 Ori accounts for 0.04 ± 0.01 $M_{\odot}$ (Tsukagoshi et al. [145]) which is slightly larger than the disk mass of a T Tauri star (~ 0.01 $M_{\odot}$). All these findings suggest that outbursts occur in Class I sources, where the star is still embedded in the infalling envelope. The outburst duration and mass accretion rate during outburst seem to correlate with the infall rate (Table 3.5): objects with higher infall rates have longer outbursts and reach higher accretion rates while objects with smaller infall rates experience short-lived outbursts. The occurrence of short outbursts might suggest that the envelope is becoming thinner, i.e. that the system is in a transition phase of an embedded Class I source to an optically visible star surrounded by a protoplanetary disk (Class II).

The Orion Nebula Cluster (ONC) is subject to extensive observational campaigns. So far, roughly 1600 stars have been confirmed to be members of the ONC and 55% of these

Table 3.5: Typical value of outburst from pre-main-sequence stars. The outburst recurrence of FU Orionis objects has been estimated as the time needed to replenish the disk mass after an outburst with a constant infall rate.

	FUors	EXors	V1647 Ori
Outburst duration [yr]	> 10	~ 1	2.6
Outburst recurrence [yr]	> 200	5 – 10	37
Mass accreted during an outburst[M$_\odot$]	$> 10^{-3}$	$10^{-6} - 10^{-5}$	$2.5 \cdot 10^{-5}$
Magnitude variation [optical mag]	4 – 6	2 – 5	~ 6
Accretion Luminosity [L$_\odot$]	few 10^2	> 25	44
Outburst accretion rate [M$_\odot$ yr^{-1}]	10^{-4}	$10^{-6} - 10^{-5}$	10^{-5}
Envelope infall rate [M$_\odot$ yr^{-1}]	$5 \cdot 10^{-6}$	$10^{-7} - 10^{-6}$	$7 \cdot 10^{-7}$
Wind velocity [Km s^{-1}]	>300	200 – 400	300 – 400
Mass loss rate [M$_\odot$ yr^{-1}]	$10^{-6} - 10^{-5}$	$10^{-8} - 10^{-6}$	$4 \cdot 10^{-8}$
Spectral features	absorption spectrum F/G-type supergiant like deep CO absorption	emission line spectrum, T Tauri like, Hα inverse P Cyg CO abs./em., Brγ emission	emission line spectrum, strong Hα emission (P Cygni) CO abs./em., Brγ emission Forbidden lines in fading phase
Note			X-rays variability

(at least) posses a circumstellar disk (Hillenbrand et al. [67]). Assuming that Class I sources account for 20% of stars with disks (lower limit, equal to the Class I fraction found in the original paper of Lada & Wilking [91]), we expect to have more than 200 Class I sources in the ONC only. If all of these 200 sources experience FU Orionis-like activity, we would expect to see 10 – 40 (depending on outburst duration and recurrence of FUors, V1647 Ori and EXors) of these stars in outburst at any time in the ONC. The total number of young eruptive stars discovered so far in the whole Orion star forming region is only seven: three FUors (FU Orionis itself, V883 Ori and Reipurth 50), three EXors (NY Ori, V1118 Ori, V1143 Ori) and V1647 Ori. Not all of these are in outburst at the same time. It appears that there is a deficit of observed outbursts in Orion. We conclude that not all Class I sources undergo FU Orionis-like events for their entire lifetime. A possible solution to this problem is that we are over-estimating the number of "true" Class I sources in Orion. The spectral energy distribution of an isolated T Tauri source seen with a disk close to edge-on may mimic a typical Class I SED. An alternative solution is that outbursts occur only in a specific stage of early evolution, namely, in the transition phase of an embedded Class I source to an optically visible T Tauri or Herbig AeBe star.

We also caution that this result is based only on a small number of Class I sources in Orion, namely, those not embedded in high density regions. Recent Spitzer observations show that there is a large number of such sources which lie in regions of extremely high extinction (Megeath et al. [109]). An outburst in one of these objects could easily have been missed in the existing surveys of Orion. More regular infrared surveys of star forming regions are needed to investigate the number of FUor-like outbursts in these embedded sources.

3.5.1 Outburst mechanism

Instability mechanisms of different flavors have been proposed to explain the FU Orionis phenomenon. The gravitational forces of a companion star may perturb the disk, enhancing accretion (e.g. Bonnell & Bastien [17]). Gravitational instability has been also proposed but, for this instability to occur the disk has to be cold and massive. The most accepted mechanism to trigger such outbursts is via thermal instability in the inner disk (e.g. Lin & Papaloizou [99]; Clarke et al. [28]; Kawazoe & Mineshige [81]; Bell et al. [14]). A key point of this model is that of a high accretion rate in the outer disk, of the order of few $\times$ 10^{-6} $M_\odot$ yr^{-1}. According to this model, outbursts will occur as long as mass is deposited in the outer disk at such a high rate. This implies that the outbursts will become shorter in time and smaller in amplitude as the infall into the disk ceases. An alternative explanation for eruptive events has been suggested by Gammie [45]. He suggested that "dead zones" of decreased accretion may develop in the case of magnetic viscosity. Material from the outer part of the disk may accumulate at the edge of such dead zones until high-accretion-rate episodes occur.

One way to explain the different outburst properties of FUors, EXors and V1647 Ori is by introducing a different outburst mechanism for each of these classes of objects. However, the data collected so far in all young eruptive stars raise the possibility of the existence of a unique class of outburst objects. In this scenario, the different types of outburst are produced by a continuum variation of one or more of the parameters involved in the instability, rather than a variation of physical mechanisms. For instance, the presence of a remnant of the infalling envelope and the estimated infall rate (Table 3.5) might favor thermal instability as the only model to explain the three groups. If this is the case, the different outburst durations between an FU Orionis, V1647 Ori and an EX Lupi might be explained by the difference in the infall rate. The thermal instability model indeed predicts shorter and smaller amplitude outbursts as infall ceases below 10^{-6} $M_\odot$ yr^{-1}, to approach typical T Tauri disk accretion rate of $\sim 10^{-7}$ $M_\odot$ yr^{-1}.

The same model is also able to explain the diversity in spectral features of the three classes of objects. The mass accretion rate reached during the outburst is (also) dependent on the envelope infall rate. When very high accretion rates and disk temperatures are reached, as in the case of FUors, the disk's interior may become hotter than the disk surface and the emitted spectrum will show absorption lines. If the accretion rate is not high enough to invert the temperature gradient in the disk's interior, the final spectrum will be dominated by emission features which are produced in the disk's wind and/or in the magnetospheric accretion columns. In this case we will see EXors or V1647 Ori-like spectra.

4

The 2003-2006 Outburst of V1647 Orionis: The reflection nebula associated to V1647 Orinis

D. Fedele [1,2]***, M. E. van den Ancker***[1]***, M. G. Petr-Gotzens***[1]***, N. Ageorges***[3] ***& P. Rafanelli***[2] ***2007, A&A, 472, 199***
[1] European Southern Observatory, Garching bei München, Germany
[2] Dipartimento di Astronomia, Universitá degli studi di Padova, Padova, Italy
[3] European Southern Observatory, Santiago, Chile

4.1 Introduction

In late 2003 the young eruptive star V1647 Orionis in the L1630 cloud in Orion went into outburst. In the following 4 months the star brightened up to 6 magnitudes in the I_C band. The rapid and strong brightness rise resembles that of a FU Orionis object. In these pre-main-sequence stars the outburst is thought to be triggered by a disk instability which leads the stellar accretion rate to increase by more than four orders of magnitude on a time scale of months (e.g. Kenyon & Hartmann [85]). The outburst of V1647 Ori produced the appearance of a reflection nebula known as McNeil's nebula (McNeil [107]). The nebula is also visible in archival data during a previous outburst of V1647 Ori in 1966-1967 (Aspin et al. [9]). The shape of the nebula in the optical is cometary with V1647 Ori at its apex. In the near infrared

McNeils's nebula has an arc-like morphology. This is a common feature of nebulae associated with FU Orionis-like objects. In these objects, it is usually thought that the nebular emission is produced by scattering in the lobe of a bipolar structure (Goodrich [51]). In the case of McNeil's nebula only the lobe oriented toward us is seen while the opposite lobe is probably obscured by circumstellar dust. Reipurth & Aspin [132] suggested that the bipolar structure might be produced by powerful outflow activity from the central star. The outflow opens a cavity in its surroundings which is illuminated by the central star at the occurrence of an outburst. An alternative scenario is that the elongated morphology is due to the relative motion of the star trough the parent cloud (Goodrich [51]). In this case there is only a single cavity, as often seen.

We present here an analysis of optical/near infrared imaging and near infrared imaging polarimetry of McNeil's nebula and discuss the nature of this structure.

4.2 Observations and data reduction

We observed V1647 Ori and McNeil's nebula in the optical and near infrared using FORS2 and NACO at ESO's Very Large Telescope in Paranal, Chile. FORS2 [8] is an optical facility (3000-10000 Å) equipped with two 2k4k MIT CCDs. It allows imaging in different bands and grism spectroscopy. NACO ([135]; [98]) provides adaptive optics assisted imaging, imaging polarimetry, coronography and spectroscopy, in the $1-5$ μm range. NACO's infrared camera (CONICA) is equipped with an Aladdin 1024×1024 pixel InSb array detector.

4.2.1 Optical photometry

Photometry of V1647 Ori and McNeil's nebula in five different optical filters (B, V, R_C, I_C and z_{Gunn}) was performed with FORS2 on 2004 February 17, December 20 and 2006 January 02 (no V-band photometry was done on this night). Photometric conditions were registered during the three nights. Multiple short ($5-10$ sec) and long (30 sec) exposures were taken dithering the telescope in the North-South direction with an amplitude of $30''$. A log of the observations is reported in table 4.1. We performed a standard data reduction process (bias subtraction, correction for flatfield and cosmic rays) using IRAF. The magnitude was computed using differential aperture photometry adopting an aperture radius of $2\farcs52$ (10 pixels) centered at the stellar position. The sky has been computed within an annulus with inner and outer radius respectively of $3\farcs02$ and $4\farcs28$ and subtracted from the aperture photometry. The computation of the stellar flux and subtraction of the local background are affected by the presence of McNeils's nebula. This leads to slightly different magnitude estimates of V1647 Ori depending on the telescope and instrument used. In particular, given the better spatial resolution of our data compared with previous data, we may better disentangle the contribution from V1647 Ori from that of the nebula.

To convert the FORS2 instrumental magnitudes to the standard photometric system, photometry of standard star fields (SA98 and PG0231) was performed in the B, V, R_C and I_C bands during the three nights. The zero point level was measured using the standard stars field. The first order color dependence and atmospheric extinctions coefficients were assumed equal to the mean FORS2 values provided by ESO[1]. For the z_{Gunn} filter, spectrophotometric standard stars were observed during the three nights: S83 in [CS62] E5 (Stetson [144]), Feige 110 and LTT 3864. For Feige 110 and LTT 3864 the calibrated z_{Gunn} magnitude was computed convolving their tabulated flux distribution[2] with the response of the filter+CCD combination[3]. For the standard star S83 in [CS62] E5, we computed the z_{Gunn} magnitude from the empirical correlation between z_{Gunn} and the VRI bands (Smith et al. [143]). We find a z_{Gunn} magnitude of 15.49 for the star E5-S83, 12.81 for Feige 110 and 12.09 for LTT3864. The aperture photometry of V1647 Ori is reported in Table 2. The surface brightness of McNeil's nebula has been computed in two different apertures centered respectively on RA=05:46:13.051 DEC=–00:05:56.25 (aperture radius = $7\overset{''}{.}56$) and on RA=05:46:14.025 DEC=–00:05:31.81 (aperture radius = $6\overset{''}{.}3$). These two locations refer respectively to blob B and C defined by Briceño et al. (2004). The sky background has been evaluated far from the nebula and subtracted from the surface brightness of the two structures. The result is reported in Table 4.2.

4.2.2 Near infrared observations

K_S-band imaging was obtained with NACO on 2005 April 08. Short exposures (DIT = 0.375 s, NDIT = 80) were acquired with the S27 camera (pixel scale 27.15 mas/pixel, FOV $28'' \times 28''$) dithering the telescope at different position. The total exposure time is 18 minutes. Thanks to the infrared wavefront sensor of NACO, the observation was adaptive optics assisted. A Strehl ratio of 0.18 was achieved resulting in an angular resolution of $0\overset{''}{.}13$. Observation of a photometric standard star (HD60778) was also taken.

---

[1] *http://www.eso.org/observing/dfo/quality/FORS2/*

[2] *http://www.eso.org/instruments/fors/tools/*

[3] *http://www.eso.org/instruments/fors/inst/Filters/*

Table 4.1: Log of FORS2 photometric observations. The image quality refers to the seeing measured on unresolved point-sources in the images. Multiple short (5 – 10 sec) and long (30 sec) exposures were taken applying an offset along the North-South direction.

		Exposure time [sec] & Image Quality [$''$]									
Date (UT)	MJD	B		V		R_C		I_C		z_{Gunn}	
2004-02-17	53052.082	10,3 x 30	0.91	10,3 x 30	1.18	5,3 x 30	0.85	5,3 x 30	0.65	5, –	0.67
2004-12-20	53359.258	10,5 x 30	0.75	10,5 x 30	0.60	5,5 x 30	0.50	5,5 x 30	0.48	5, –	0.53
2006-01-02	53737.253	10,5 x 60	0.73	–	–	10,5 x 60	0.58	10,5 x 60	0.50	10, 5 x 60	0.50

The reduction was carried out with the ESO pipeline V. 1.3.5[4]. The raw frames were corrected for bad pixels and flatfield. The sky has been subtracted from the dithered images which were then shifted and co-added to obtain a final mosaic.

Polarimetric observations were performed with NACO on on March 01 2006 in K_S-band with the S27 camera. 10 multiple dithered exposures (DIT = 25 s, NDIT = 2) were taken with a four wire grid analyzer at four different angles (0°, 45°, 90°, 135°). After calibration (bad pixels removal, flat fielding and sky subtraction) the dithered frames were shifted and added. The calibrated images were combined to create the Stokes parameters images (I,Q and U) and the linear polarization module (P) and position angle (θ). The error associated with the polarization values in McNeil's nebula purely from shot-noise considerations are of the order of 10 - 30 % for both degree of polarization and position angle. The measured polarization of McNeil's nebula was calibrated using the standard star HD 38563C (Whittet et al. [156]), for which the degree of polarization is known. Knowing the intrinsic polarization of HD 38563C we measured the degree of instrumental polarization and the zero point of position angle adopting an aperture of $1\farcs08$ diameter.

4.3 Results

4.3.1 Optical imaging

Figure 4.1 shows a color composite image of McNeil's nebula and of V1647 Ori taken with FORS2 on 2004 December 20. Blue, green and red colors correspond respectively to the B, R_C and z_{gunn} photometric bands. The nebula has a typical cometary shape extending to the North with V1647 Ori at its apex. Despite the red energy distribution of the illuminating source, the nebula emits mainly in the optical. The emission within McNeil's nebula is not uniform in intensity or in color. There are two main "blobs" of higher emission (respectively source B and C in Briceño et al. [21], see Fig. 2): the first is close to the star extending to North-West. It is very bright in all the three bands. The second blob is farther away from the star in direction North-East at a distance of $\sim 35''$. This structure emits mainly in B and R_C bandpasses and is spatially coincident with the knot A of the Herbig-Haro object HH 22. South-West of V1647 Ori the source 2MASS 05461162-0006279, which is a visual binary, is clearly visible.

In Figure 4.2 we show a temporal sequence of images of V1647 Ori and McNeil's nebula in 4 photometric band-passes: B, R_C, I_C and z_{gunn}, taken on

---

[4] *ftp://ftp.eso.org/pub/dfs/pipelines/naco/*

Figure 4.1: Color image of V1647 Ori and McNeil's nebula obtained with FORS2 on 2004 December 30. The blue, green and red colors correspond respectively to the photometric bands B, R_C and z_{Gunn}. The dimension of the image is $2\overset{\prime}{.}07 \times 1\overset{\prime}{.}88$. North is up, East is left.

2004 February 17, December 20 and 2006 January 02. The pixel values were converted in surface brightness and are expressed in mag/arcsec^2. During the first two epochs V1647 Ori was at the maximum light of the outburst (*plateau* phase). On January 2006 the star was quickly fading returning at the quiescent phase. The brightness temporal evolution of MCNeil's nebula follows that of the outbursting star: the nebular emission remains unchanged during the *plateau* phase, as is clear from the top and middle rows of Figure 4.2. In early 2006 the nebula has mostly disappeared. It is no longer visible in B, where also V1647 Ori was not detected up to a limiting magnitude of $B = 24.9$. A faint emission from blob B and C is still visible in the R_C, I_C and z_{Gunn} filters. The R_C bandpass reveals a clumpy structure of the northern blob never seen before. The brightness level is of the same order as that of V1647 Ori. Given the spatial coincidence with HH 22A, such emission is likely produced by Hα and forbidden lines (all falling in the R_C bandpass) within the Herbig Haro knot. Figure 4.3 shows a blow-up of the R_C band image taken on January 2006. Apart from a diffuse emission, three main clumps are visible in the knot A of HH 22 (clumps C1, C2 and C3).

We compared the appearance of McNeil's nebula in the period February 2004 – January 2006. The images were spatially matched using four different (point-like) stars as reference objects. This gives us an accuracy of roughly half a pixel ($0\farcs13$). The overall morphology of the nebula (including the substructures B and C) does not show major changes during such period. Given the FWHM of the FORS2 images ($< 0\farcs85$ in R_C) and the nearly two years of time interval, we conclude that no evidence of spatial motion was identified within McNeil's nebula down to a resolution of $0\farcs43$ yr^{-1}, corresponding to an upper limit to the projected expansion velocity of 800 km s^{-1} at the adopted distance toward V1647 Ori of 400 pc.

4.3.2 NACO imaging

Figure 4.4 shows the K_S-band image of V1647 Ori and McNeil's nebula taken on 2005 April 08. Compared to the optical image, the nebula in the K_S band appears much more compact. It has a slightly flattened morphology in the North-South direction, being more elongated in the direction perpendicular to the optical emission. An arc-like tail is visible from the East side of the compact nebulosity extending in direction North-East. Figure 4.5 is a blow-up of the small spatial scale of McNeil's nebula. Apart from the diffraction patterns, another tail extends from the central star in direction North-West. This is fainter than the NE one and less extended. Compared to previous observations at equal wavelength (Reipurth & Aspin [132]; Ojha et al. [123], [124]; Acosta-Pulido et al. [6]), all taken between February and November 2004, the morphology of McNeil's nebula is overall unchanged. However, in our NACO image the nebula is fainter and less extended. Despite the better angular resolution of this observation compared to previous work we could not find evidence of small spatial scale structure within the central $1\overset{''}{.}5$, or 600 AU assuming a distance V1647 Ori of 400 pc. The magnitude of the system (star+nebula) within an aperture diameter of $16\overset{''}{.}3$ is $K_S = 8.97 \pm 0.01$.

A point-source $21\overset{''}{.}2$ North of the nebula is clearly visible in figure 4.4 (RA(J2000) = 05:46:13.75, DEC(J2000) = -00:05:44.5). We will discuss the nature of this source in Appendix A.

4.3.3 NACO polarimetry

In our K_S-band polarimetric observation (Fig. 4.6) we detect a compact polarized emission centered on V1647 Ori. We do not detect polarized emission at radii $> 1\overset{''}{.}6$ from V1647 Ori. The images were binned in 2×2 square bins. Alignment and subtraction residuals are present in the inner region as well as along the diffraction pattern of the nebula. The polarization values go from 10 – 20 %. The vectors are well aligned with a mean position angle of 90° ± 9° East of North. The highest values are detected North and South of V1647 Ori. The most likely reason for not detecting extended polarized light from McNeil's nebula could be that we did not integrate deep enough in the four exposures. Acosta-Pulido et al. [6] have indeed measured large scale polarized emission from the nebula in their LIRIS/WHT J band observations.

4.4 Data interpretation

Following the method of Magnier et al. ([103], hereafter MA99), we can use the color dependence of scattered light to probe the distribution of material inside the nebula and in the vicinity of V1647 Ori. As in MA99, our basic assumption is that the light from V1647 Ori is coming directly to the earth from the central star without being scattered but only partially extinguished. On the other hand the light from the nebula that reaches the earth is also scattered. The effect of scattering would be that the observed colour of V1647 Ori is bluer than the colour of V1647 Ori seen by the nebula. As a consequence, the nebula would appear redder than V1647 Ori. Since there are no parts of McNeil's nebula which are redder than V1647 Ori we believe that our assumption is a good one. We have:

$$f_*(\lambda) = f_{*,0}(\lambda)10^{-0.4A_{V,1}(\frac{A_\lambda}{A_V})} \tag{4.1}$$

$$f_{neb}(\lambda) = f_{*,0}(\lambda)10^{-0.4A_{V,2}(\frac{A_\lambda}{A_V})}\Gamma\big(\frac{\lambda}{\lambda_0}\big)^{-\gamma} \tag{4.2}$$

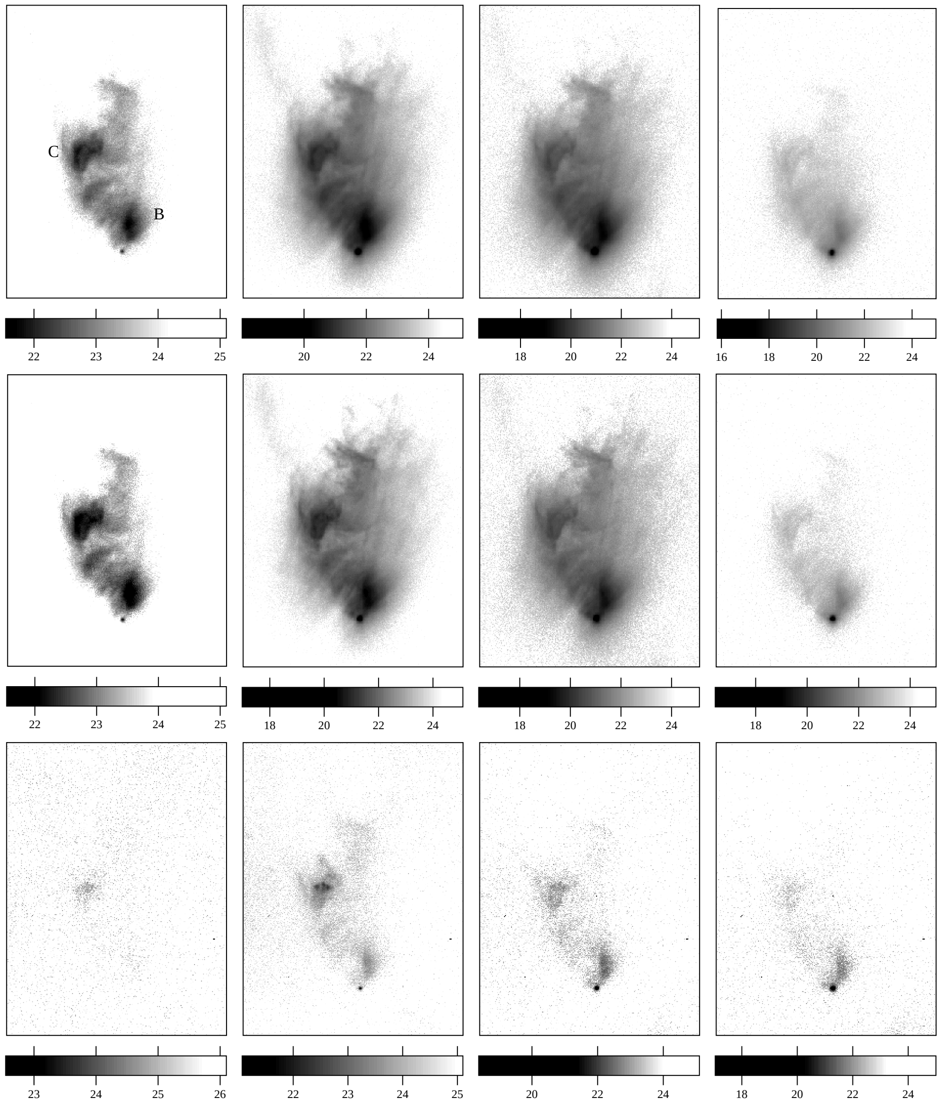

Figure 4.2: FORS2 images of V1647 Ori and McNeil's nebula taken on 2004 February 17 (top row), 2004 December 20 (central row) and 2006 January 02 (bottom row). The four columns corresponds to the photometric bands (from the left): B, R_C, I_C and z_{gunn}. The images are expressed in mag/arcsec^2. North is up, East is left. All images have the same dimension of $76''$x $101''$.

Table 4.2: FORS2 aperture photometry of V1647 Ori and surface brightness of blob B and C.

Date	MJD	B	V	R_C	I_C	z_{Gunn}
			V1647 Ori			
		(mag)	(mag)	(mag)	(mag)	(mag)
2004-02-17	53052.075	20.66 ± 0.10	18.80 ± 0.05	16.90 ± 0.05	15.07 ± 0.03	13.90 ± 0.10
2004-12-20	53359.248	20.75 ± 0.12	18.82 ± 0.05	17.06 ± 0.03	15.11 ± 0.04	13.95 ± 0.10
2006-01-02	53737.245	> 24.9	–	21.33 ± 0.13	18.95 ± 0.08	16.29 ± 0.10
			Blob B			
		(mag/arcsec^2)	(mag/arcsec^2)	(mag/arcsec^2)	(mag/arcsec^2)	(mag/arcsec^2)
2004-02-17	53052.075	22.45 ± 0.05	21.45 ± 0.03	20.69 ± 0.03	19.71 ± 0.02	20.96 ± 0.10
2004-12-20	53359.248	22.90 ± 0.06	21.87 ± 0.03	21.05 ± 0.03	20.11 ± 0.02	22.19 ± 0.10
2006-01-02	53737.245	>24.9	–	24.21 ± 0.13	23.20 ± 0.10	22.53 ± 0.10
			Blob C			
		(mag/arcsec^2)	(mag/arcsec^2)	(mag/arcsec^2)	(mag/arcsec^2)	(mag/arcsec^2)
2004-02-17	53052.075	22.59 ± 0.04	21.91 ± 0.03	21.41 ± 0.03	20.82 ± 0.03	22.37 ± 0.10
2004-12-20	53359.248	22.83 ± 0.06	22.08 ± 0.03	21.52 ± 0.03	20.99 ± 0.03	23.35 ± 0.10
2006-01-02	53737.245	>24.9	–	23.86 ± 0.10	23.49 ± 0.10	23.29 ± 0.10

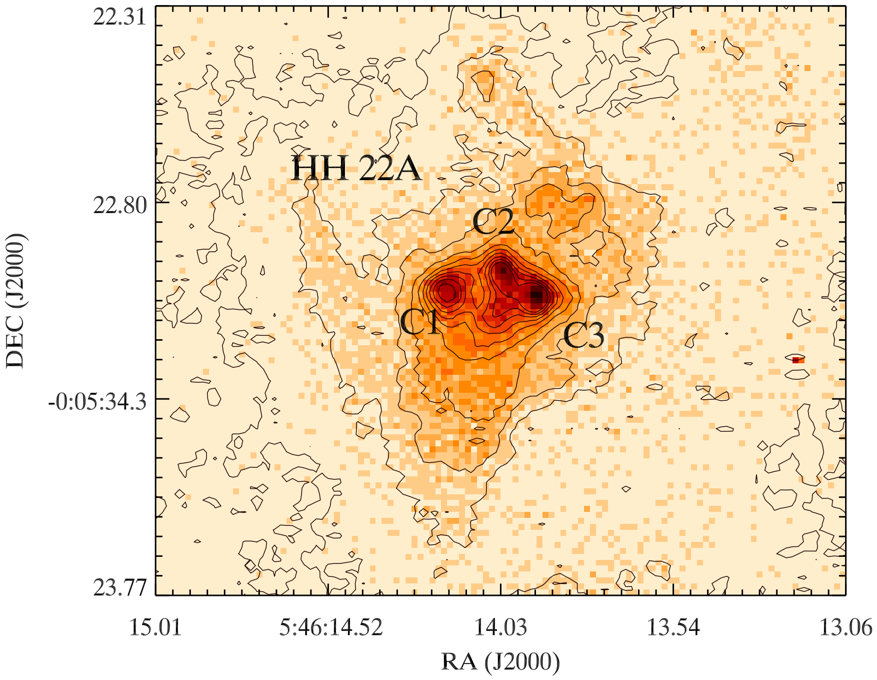

Figure 4.3: Blow-up of the R_C-band image taken on 2006 January 01 showing the presence of three clumps (labeled C1,C2 and C3) in the vicinity of HH 22A.

where f_* and f_{neb} are the observed flux of V1647 Ori and of the nebula, Γ is a normalization factor which takes into account the amount of scattered light and γ the wavelength dependence of the scattering process. For Rayleigh scattering $\gamma = 4$. Simulations of other types of scattering processes (such as Thomson or Mie) produce values close to 4 (MA99). From the ratio of the two observed fluxes we have:

$$log\Big(\frac{f_{neb}(\lambda)}{f_*(\lambda)}\Big) = +0.4\Delta A_V \frac{A_\lambda}{A_V} + log\Gamma - \gamma log(\frac{\lambda}{\lambda_0}) \tag{4.3}$$

Equation 4.3 can be solved to determine ΔA_V, i.e. the difference between the extinction towards the line of sight of V1647 Ori ($A_{V,1}$) and the extinction towards any direction of McNeil's nebula ($A_{V,2}$). All images were smoothed and binned in order to have the same PSF and to increase the S/N in the nebula (final pixel scale 0.″5 / pixel). Counts were converted in flux units (Jy) using the appropriate magnitude-flux relation. The standard extinction law, E(B-V) = 3.1 A_V has been applied to compute A_λ. Finally we performed a linear least-squares in the five images on a pixel by pixel basis to determine ΔA_V. Figure 4.7 shows the result. The background image is the V image

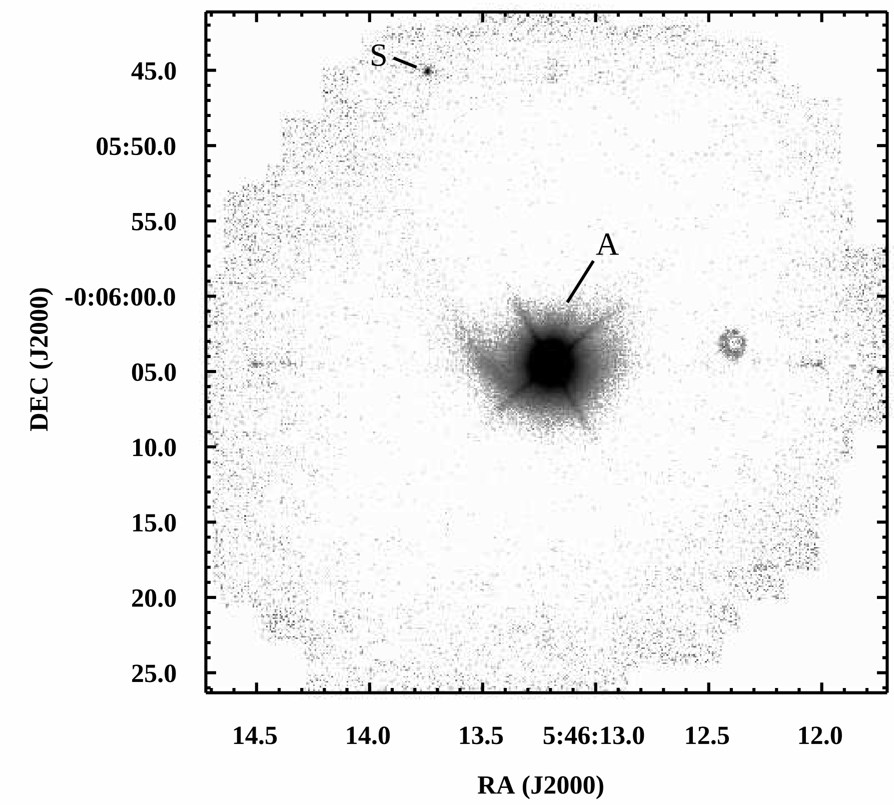

Figure 4.4: NACO K_S band image of V1647 Ori and McNeil's nebula taken on 2005 April 04. The nebula (A) appears much more compact than in the optical with a slightly flattened morphology in direction North-South. An arc-like structure is also detected. A point-like source (S, RA = 05:46:13.75, DEC = -00:05:44.5) is detected 21.″2 North-North East of the nebula. The circular spot West of V1647 Ori is a ghost image caused by the brightness of V1647 Ori.

of McNeil's nebula. The contour plot is the differential extinction. The extinction is not uniform in the nebula. Close to V1647 Ori and at the base of the nebula ΔA_V is lower. Moving from the star to the North-East, a region of higher extinction shows up. In correspondence of the northern knot, the method used here to compute the extinction may not be valid as it is coincident with knot A of the Herbig-Haro object HH 22 which is intrinsically bright. The total optical extinction in the direction of V1647 Ori caused by material within McNeil's nebula is $\sim$ 6.5 mag. As this estimate does not include foreground extinction, it is a lower limit to the total optical extinction towards V1647 Ori.

The differential extinction map shows some similarities with the K-band image of McNeil's nebula (Fig. 4.4). The contours of ΔA_V in the vicinity of V1647 Ori show an arc-like geometry. Moreover, the region of higher extinction in the nebula mimics the tails seen in the NACO image. The opening angle between the two tails of higher extinction is $\simeq 95°$. The asymmetry in the spatial distribution of dust in McNeil's nebula may be indicative of an outflow activity with the material moving away from the star towards the North.

The result does not change if we apply the Cardelli et al. [24] extinction law with larger values of R_V up to 5. This is not surprising beacuse changing the value of R_V has a significant effect only on the shape of the ultraviolet extiction and produces only small changes in the optical/NIR.

Our K band polarization map of V1647 Ori reveals a compact region of aligned vectors with high degree of polarization. At larger scales the polarization pattern is centro-symmetric as found by Acosta-Pulido et al. [6]. Such structures are often seen in near-infrared polarimetric map of Class I YSOs with circumstellar nebulae. These systems show a region of aligned vectors, known as a "polarization disk", at the location of the central source, and a gradual transition to a centrosymmetric pattern of vectors in the surrounding nebula. The polarization disc is often attributed to multiple scattering in cases where the optical depth toward the central source is too high for direct observation (e.g Whitney & Hartmann. 1993; Bastien & Menard 1988). Multiple scattering, however, is not able to reproduce high polarization (> 15 %) measured sometimes in low optical depth regions (Lucas et al. [101] and references therein). The aligned vectors of the polarization disk are usually parallel to the disk plane. Interestingly, the position angle of the observed polarization in the vicinity of V1647 Ori (90°± 9°, Fig. 4.6) is perpendicular to the major axis of the reflection nebula seen in the optical. If the large scale reflection nebula can be interpreted as being shaped by a wind or outflow from the central star, the polarization vectors would indeed be aligned with the disk plane.

Moreover, the high percentage of linear polarization observed toward V1647 Ori may suggest that the central (proto-)star is obscured even at 2.2 μm.

4.5 Discussion and conclusions

Young stars are often surrounded by optical or infrared nebulae (e.g. Padgett et al. [125], Zinnecker et al. [159]). Given the complexity of the star formation process there are many mechanisms to produce such nebulae and their nature

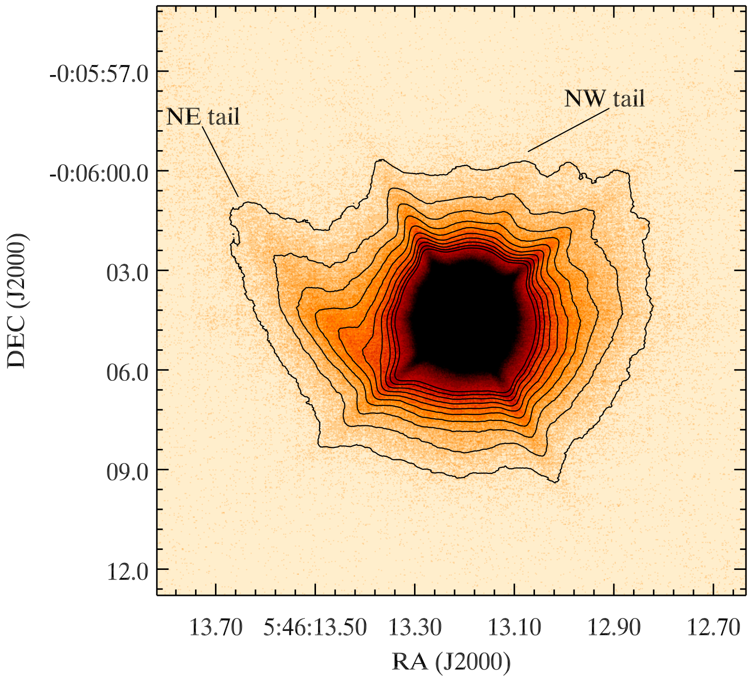

Figure 4.5: Blow-up of the K_S band image of V1647 Ori and McNeil's nebula taken on 2005 April 04. The two tails characterizing the ark-like structure are showed. On spatial scales smaller than $1\farcs5$ no deviation from circular profile is detected.

is not unique. Strong outflow activity from the central star is responsible for the typical Herbig Haro objects which emit mainly in forbidden lines as the shocked gas cools. Strong UV flux from a massive star ionize all the circumstellar environment producing an H II region. Also wind from a young star might produce large scale nebular emission. In the case of McNeil's nebula, the energy distribution and the temporal evolution of the nebula mimics that of the illuminating source. The polarization pattern and extinction map do agree with dust scattering taking place in a circumstellar environment.

All these findings suggest that McNeil's nebula is a pure-reflection nebula where the light from the central star and the accreting disk is scattered by pre-existing material in the vicinity of V1647 Ori.

The morphology of McNeil's nebula resembles that of FU Orionis-like objects, which often show an arc-like morphology (Goodrich [51]). The prevalent theory about the nature of these objects (Goodrich [51]) is that the nebular emission mimics the lobe of a bipolar structure in which one of the lobe is oriented toward the observer. The secondary lobe may be obscured by the

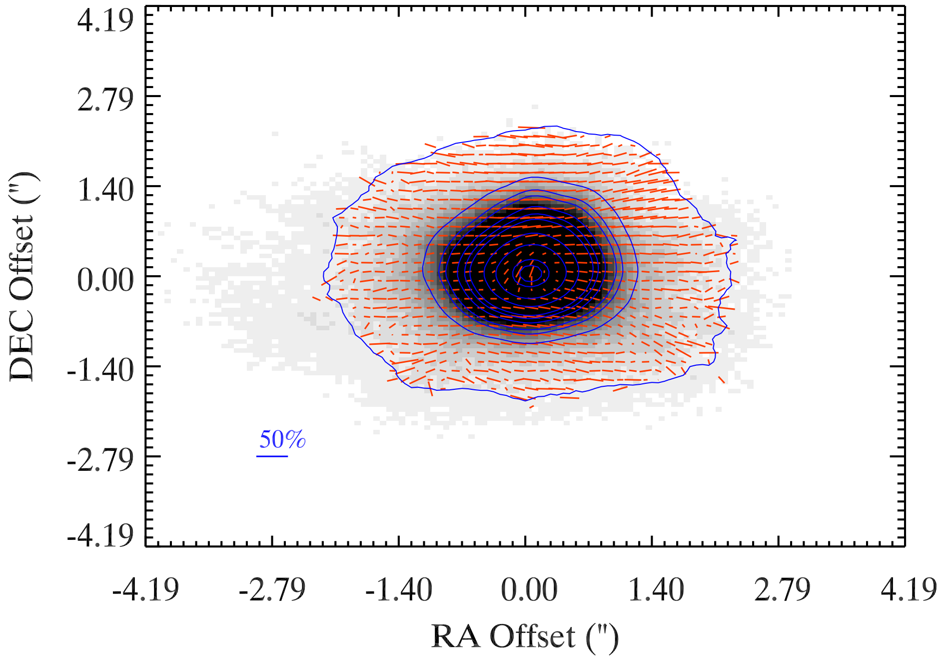

Figure 4.6: K_S band imaging polarimetry of V1647 Ori and McNeil's nebula taken on 2006 March 01. Polarization vectors are superimposed upon total intensity map and contours. Alignment and subtraction residuals are present the inner region as well as along the diffraction pattern of the telescope. The polarization values go from 10 – 20 %. The highest values are detected North of V1647 Ori. The mean position angle of the vectors is 90° ± 9°. North is up, East is left.

circumstellar disk and/or envelope. The nebula will always have an arc-like morphology unless it is observed pole-on. In this case the nebula will appear ring-like. Reipurth & Aspin [132] suggested that the bipolar structure might be produced by powerful outflow activity from the central star. The outflow opens a cavity in its surroundings which is illuminated by the central star at the occurrence of an outburst. The arc-like structure seen in the K-band image and its similarity with the extinction map suggest that an outflow travels roughly from the star to the North (slightly twisted to North-West). The current asymmetry in the distribution of material within McNeil's nebula could be the result of the clearing of pre-existing material (perhaps left over from the original cloud) by a previous outflow.

It is worth to note that from an optical spectrum of V1647 Ori taken on January 2006 (when the star was quickly returning to its pre-outburst flux level), Fedele et al. [44] found strong emission from forbidden lines which may

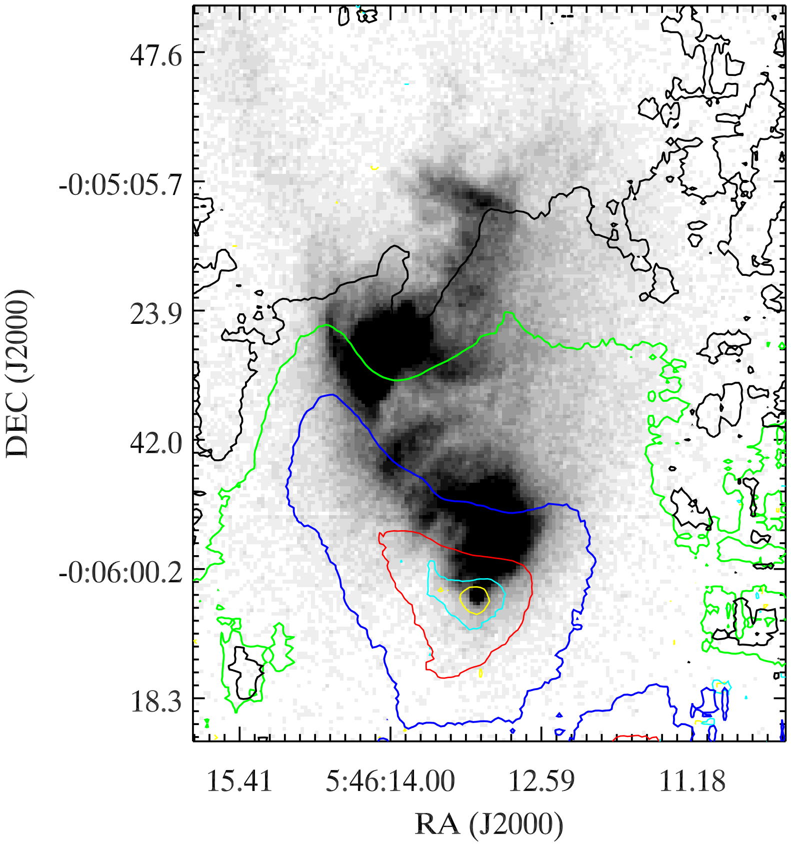

Figure 4.7: Differential extinction map of McNeil's nebula. The grayscale shows the V-band image of the nebula. Overplotted are the ΔA_V contour level 1.5 (yellow), 2.5 (cyan), 3.5 (red), 4.5 (blue), 5.5 (green), 6 (black) magnitudes. The extinction increases gradually as the line of sight from the star to the nebula tilts towards the East.

indeed indicate ongoing outflow activity. From our multi-epoch imaging of McNeil's nebula we derive an upper limit to the motion of material within McNeil's nebula of 800 km s^{-1}.

4.6 On the nature of the red source North-East of V1647 Ori.

The point-like source $21\farcs2$ North North-East of V1647 Ori (RA = 05:46:13.75, DEC = -00:05:44.5, Fig. 4.4) is not visible in any of our optical images up to a R_C limiting magnitude of $\simeq 24.5$. From the NACO observation we compute a magnitude of $K_S = 16.63 \pm 0.13$ within an aperture diameter of $1''\!.08$. Acosta-Pulido et al. [6] detected the source only in the K band, but not in the J band and only barely in the H band. They estimate magnitudes of $J > 19$ and $H > 16$. The same object is clearly visible in the SPITZER/IRAC 4.5 μm image of Muzerolle et al. [116], although they don't give an estimate of its magnitude.

An unreddened stellar photosphere of any temperature has a $J-K$ color of < 1 mag (e.g. Kenyon & Hartmann [86]). We derive $J-K > 2.37$. To redden a colour of $J-K=1$ to the observed lower limit an extinction of $A_K = 0.5$, or equivalently $A_V = 6.9$, is needed. Thus, if we assume that this object is located in the background of the Orion cloud, its absolute K-band magnitude would be < 16.1 mag. This excludes the possibility that it is a main sequence star. It may be an highly reddened background giant star, although the space density of these stars makes the a priori chance of finding such an object low.

The very red energy distribution of this source ($R_C - K_S > 7.9$) is also compatible with either a brown dwarf (for which $R-K > 6$ mag, Kirkpatrick et al. [87]) or a protostar still embedded in its infalling envelope. Assuming that it is located in Orion, just behind McNeil's nebula, we can estimate its foreground optical extinction from the extinction map of figure 4.7. The position of this source is within the $\Delta A_V = 4$ contour level, i.e. the extinction due to McNeil's nebula toward this direction is $\mathrm{A}_V \simeq 1.5$ mag. Assuming a further contribution of $\mathrm{A}_V = 1.5$ mag due to the foreground interstellar medium, the total optical extinction is $\mathrm{A}_V \simeq 3$ mag (or $\mathrm{A}_R \simeq 2.3$ mag). The corrected energy distribution is still very red ($R_C - K_S > 5.7$ mag) and both the brown dwarf and protostar hypothesis are still valid.

Whatever its nature, embedded protostar, brown dwarf or highly reddened background giant, this source located close to V1647 Ori is an unusual object which deserves further study.

5

Spatially resolved dust and gas distribution of three Protoplanetary Disks.

D. Fedele^{1,2,3}***, M. E. van den Ancker***^{3}***, B. Acke***^{4}***, G. van der Plas***^{3,5}***, R. van Boekel***^{1}***, M. Wittkowski***^{3}***, Th. Henning***^{1}***, J. Bouwman***^{1}***, G. Meeus***^{6}***, & P. Rafanelli***^{2} ***2008 A&A submitted***
[1] Max Planck Institut für Astronomie, Heidelberg, Germany
[2] Dipartimento di Astronomia, Universitá degli studi di Padova, Padova, Italy
[3] European Southern Observatory, Garching bei München, Germany
[4] Instituut voor Sterrenkunde, Leuven, Belgium
[5] Sterrenkundig Instituut 'Anton Pannekoek', University of Amsterdam, Amsterdam, The Netherlands
[6] Astrophysikalisches Institut Potsdam, Potsdam, Germany

5.1 Introduction

Many pre-main-sequence stars are characterized by excess infrared emission above the stellar photospheric level which, depending on the evolutionary state of the system, may start in the near infrared (1 – 5 μm) or at longer wavelengths. Responsible for this emission is the dust distributed around the young star. The dust particles absorb a large amount of the short wavelength stellar photons and re-emit them at infrared wavelengths. This dust is believed to be confined to a disk-like structure which forms in the early phase of star formation as a result of the conservation of the angular momentum of the parental cloud. Disk formation is followed by a longer phase of disk accretion during which disk material accrete onto the young star at a typical accretion rate of $10^{-7} - 10^{-10}$ $M_\odot$ yr^{-1}. The interstellar dust and gas which form the disk undergo changes in its composition and size. Infrared surveys show that after a mean age of 3 Myr the inner part of the disk is cleared of dust. Viscous accretion, photo-evaporation and planet formation are the likely mechanisms responsible for this phenomenon (see review in Henning [62]).

A circumstellar disk is believed to be the locus where planet formation takes place. The large number of recently discovered exo-planetary systems and the variety of such systems raised many new questions about the structure and evolution of *protoplanetary* disks. Of particular interest for the understanding of disk evolution and planet formation is the coupling of gas and dust in disks. A main assumption underlying essentially all proto-planetary disk models is that dust and gas are thermally coupled. It is an open question whether this assumption holds in the disk surface and efforts have been made to improve disk models by taking into account the dust-gas decoupling (e.g. Kamp & Dullemond [83]). While gas and dust are thermally coupled in the disk interior, in the low density environments of the disk surface layer, the two components may decouple.

The detailed structure of the disk surface temperature in the presence of gas-dust decoupling was studied by Jonkheid et al. [79], Kamp & Dullemond [83] and Nomura & Millar [121]. Different heating/cooling processes act at different heights in the disk. In particular, very high in the atmosphere, with particle densities as low as $n < 10^5\text{cm}^{-3}$ ($A_V \lesssim 10^{-3}$ mag), the gas temperature is set by the balance of photoelectric heating and fine structure line cooling of neutral oxygen (Jonkheid et al. [79], Kamp & Dullemond [83]). In the upper layers of a protoplanetary disks the gas temperature may exceed the dust temperature. At small radii (< 50 AU) the temperature of the gas above the disk photosphere may reach up to $\sim 10^4$ K. At larger radii (> 50 AU) the gas can become as hot as few hundred Kelvin (Kamp & Dullemond [83]). However, it is not obvious that such a hot and tenuous disk atmosphere can remain as a stable structure of a disk. The difference in gas and dust temperature as well as other processes (e.g. disk wind, disk evaporation, dust coagulation and settling) may lead to a physical decoupling of gas and dust in disks. In this chapter we present the first direct comparison of the dust and gas emission of three pre-main-sequence stars: HD 101412, HD 135344 B and HD 179218. These are intermediate-mass (1.7 - 2.7 $M_\odot$) stars belonging to both group I (flaring disk: HD 135344 B and HD 179218) and group II

Table 5.1: Properties of programme stars. Column "Meeus group" gives the classification in *flared* (group I) and *self-shadowed* (group II) disks by Meeus et al. [108]. Column "[O I] extent" reports the extent (minimum and maximum radius) of the [O I] emitting region as derived in paper I. Disk position angle (PA) and inclination are taken from paper I.

Star	RA (J2000)	DEC (J2000)	Sp.T	M_{star} [$M_\odot$]	$F_{12\mu m}$ [Jy]	Distance [pc]	Meeus Group	PA [°]	Inclination [°]	[O I] extent [AU]
HD 101412	11:39:44.46	-60:10:27.7	A0IIIe	2.3	3.22	160	II	–	30	0.15 - 10
HD 135344 B	15:15:48.44	-37:09:16.0	F4Ve	1.7	1.59	140	I	100	45	0.1 - 100
HD 179218	19:11:11.25	+15:47:15.6	B9e	2.7	23.4	240	I	10	40	0.4 - 50

(flattened disk: HD 101412) according to the classification of Meeus et al. [108]. van der Plas et al. [150] (hereafter paper I) presented high resolution spectroscopy of the optical [O I] 6300.304Å line with VLT/UVES of these three stars. Here we present N-band interferometric observations obtained with VLTI/MIDI aimed at spatially resolving the mid-infrared emitting region of the disk. We will also compare the thermal coupling between dust and gas in the disks surroundings our three targets by comparing the MIDI observations to a simple phenomenological model derived from the [O I] data. The properties of the programme stars are reported in Table 5.1. The paper is organized as follow: section 5.2 briefly summarizes the results of paper I; section 5.3 contains information about observations and data reduction; in section 5.4 and 5.5 we report respectively an analysis of the interferometric measurements and the the comparison with the optical data of paper I. Discussion and conclusions are summarized in section 5.6.

5.2 [OI] emission: paper I

High resolution optical spectroscopy with VLT/UVES revealed a double peaked line profile of the [O I] 6300.30Å line for HD 101412 and HD 179218 and a single peaked profile for HD 135344 B. This emission is thought to be caused by photodissociation of the OH molecule by stellar UV photons. A fraction of the resulting excited oxygen atom is in the upper state ($^1D_2$) of the 6300.30Å transition. The [O I] 6300.30Å line is thus non-thermal and strongly sensitive to the UV radiation from the central star (Acke et al. [4]). For this reason, the oxygen line traces only the surface layers of the disk which are directly exposed to the stellar radiation field.

The Doppler broadened oxygen emission profile was translated into an amount of emission as a function of distance from the central star. The resulting radial profile of the [O I] emission is in agreement with the expected disk shapes as derived from their spectral energy distribution (SED) according to the phenomenological classification of Meeus et al. [108]. Evidence of a self-shadowed disk is found for HD 101412 while the disk around HD 179218 and HD 135344 B appear to have a flared structure. However, the [O I] radial profile is more complex. For all targets the oxygen emission starts at velocities corresponding to their dust sublimation radius and extends up to radii of 10 – 90 AU. The normalized intensity [O I] radial profiles for the three stars are shown in Figs. 5.8, 5.9 and 5.10.

5.3 Observations and data reduction

MIDI[1] (Leinert et al. [96]) is the mid-infrared (8 – 13 μm) beam combiner of the VLT interferometer on Cerro Paranal, Chile. MIDI can combine the light of any pair of the 4 ESO VLT telescopes (UT, 8.2-m). MIDI allows spectrally resolved observations, that is, the signal is dispersed by either a prism ($\Delta\lambda/\lambda \approx 30$) or a grism ($\Delta\lambda/\lambda \approx 300$). For our project we used the low resolution (prism) mode and two nearly perpendicular baselines: UT1–UT2 ($B = 57$m, PA $= 26°$) and UT3–UT4 ($B = 62$m, PA $= 111°$). Taking advantage of the earth rotation (which modifies the projection of the baseline on the sky) we observed our targets at different sidereal time, to optimize the coverage of the *(u,v)* plane.

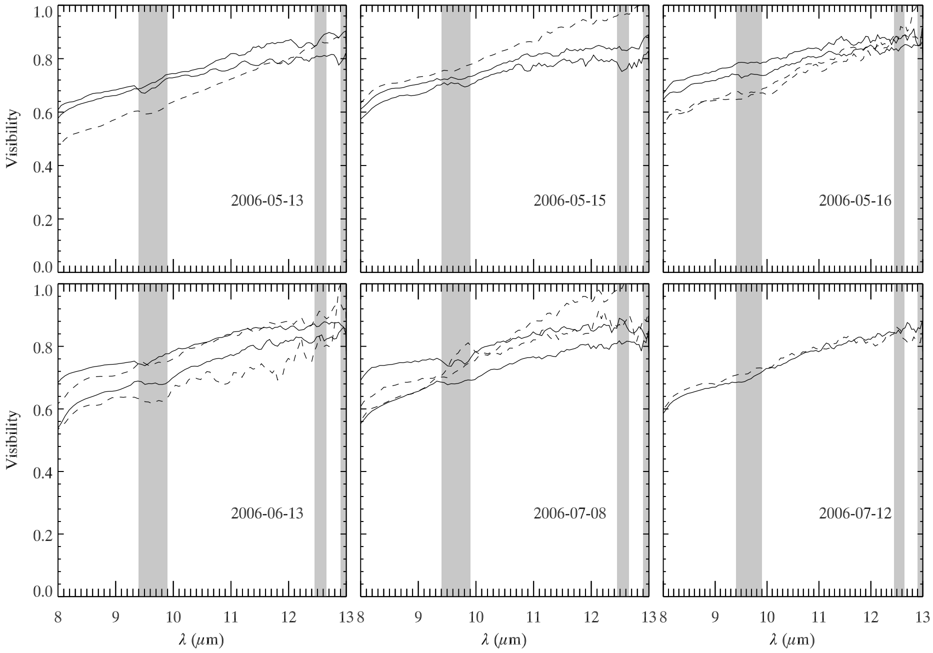

Figure 5.1: Transfer function of VLTI/MIDI. For each night, the different lines correspond to different calibrators observed with the prism in both modes (HS and SP). The overall shape of the transfer function, for a given mode, does not drastically change during the night .

Two modes are available for the acquisition of the interferometric signal: "High Sens" and "Sci Phot". With the first mode, the photometric signal (i.e. the pure, not combined, 8 – 13 μm spectrum of the source coming from

---

[1] www.eso.org/instruments/midi

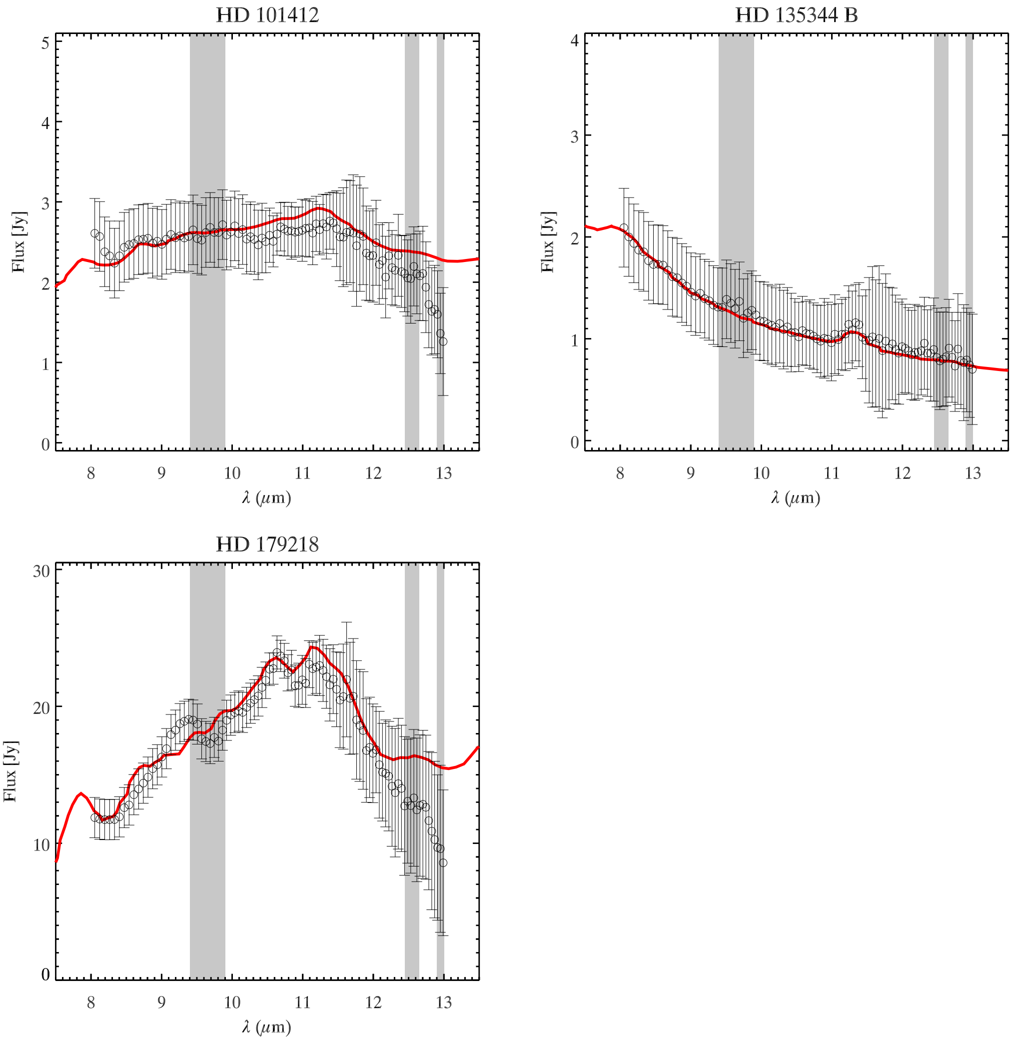

Figure 5.2: MIDI spectra (diamonds) of HD 101412, HD 135344 B and HD 179218. The MIDI spectra were scaled to match the Spitzer IRS spectra (red line) at 9 μm. The vertical grey regions are characterized by strong atmospheric absorption bands. Residual of the data reduction may be present within these regions.

the two telescopes) is acquired soon after the interferometric signal. In Sci Phot mode, the two signals are acquired at the same time. We used both modes depending on the N-band luminosity of the source. The log of MIDI observations is reported in Table 5.2. The data were reduced with the standard

Table 5.2: Summary of VLTI/MIDI observations. Column "Mode" indicates the beam combination mode of the interferometric signal: High-Sens (HS) or Sci-Phot (SP). Columns "$B_\perp$" and "PA" list the length of the projected baseline and its position angle (east of north).

Night	UT [hh:mm]	Mode	$\lambda/\Delta\lambda$	Baseline	$B_\perp$ [m]	PA [°]	Airmass	Calibrator
				HD 101412				
2006-05-15	23:38 - 00:02	SP	30	UT3-UT4	59	102	1.2	HD 107446
2006-05-16	01:55 - 02:18	SP	30	UT3-UT4	62	110	1.3	HD 107446
2006-06-13	00:18 - 00:34	SP	30	UT1-UT2	43	30	1.3	HD 107446
				HD 135344 B				
2006-05-13	04:32 - 05:15	HS	30	UT3-UT4	62	112	1.0	HD 129456
2006-06-13	23:26 - 23:52	HS	30	UT1-UT2	56	27	1.3	HD 129456
2006-07-12	03:14 - 03:47	HS	30	UT1-UT2	47	10	1.3	HD 129456
				HD 179218				
2006-05-16	05:25 - 05:44	SP	30	UT3-UT4	58	128	1.7	HD 188512
2006-06-13	06:42 - 06:56	SP	30	UT1-UT2	48	42	1.3	HD 188512
2006-06-13	08:07 - 08:25	SP	30	UT1-UT2	53	40	1.5	HD 188512
2006-07-08	06:45 - 07:03	SP	30	UT3-UT4	44	84	1.6	HD 188512

data reduction software MIA+EWS v1.5.2[2,3] using the Expert Work Station (EWS). Detailed documentation on the reduction procedure might be found in Ratzka [131] and Jaffe [73] or at the cited web pages.

Standard stars (HD 107446, HD 129456 and HD 188512) were observed close in time and in airmass to the science targets. The angular diameter of these stars is well known and they can be used as calibrators for the transfer function of the instrument. Other calibrators observed during these nights were used to check the stability of the transfer function. The error on the calibrated visibility of the science targets is the standard deviation resulting from calibration with different calibrator stars for each night. Fig. 5.1 shows the transfer function (i.e. the instrumental visibility of the calibrators) for the six nights of observations. For each night, all the calibrators observed with the prism in both modes (HS and SP) are plotted. The overall shape of the transfer function with wavelength varies by less than 10% during the night. The standard stars were also used to flux calibrate the mid-infrared spectrum of the science targets. Conversion factors from counts to Jy were computed from theoretical spectral energy distributions (SED). Energy distributions were derived by matching the spectral type of the calibrators to stars in the Cohen list (Cohen et al. [30]) and scaling the spectrum with the ratio of their IRAS 12 μm fluxes.

---

[2] www.mpia-hd.mpg.de/MIDISOFT

[3] www.strw.leidenuniv.nl/ koehler/MIA+EWS-Manual

The averaged MIDI spectra of the three targets are shown in Fig. 5.2. The Spitzer spectrum is plotted for comparison. Each spectrum was scaled in order to match the Spitzer spectrum at 9 μm. MIDI and Spitzer spectra agree well. A systematic deviation of the MIDI spectrum from the Spitzer one is visible at the red edge of the N-band. This is due to a non-perfect correction of the MIDI spectrum for atmospheric absorption.

5.3.1 Note on the data reduction of HD 135344 B

The data reduction process of HD 135344 B deserves a more detailed description. The brightness of this target is close to the sensitivity limit of the instrument. To check for the quality of the data we used both the coherent (EWS) and incoherent (MIA) method. Given the faintness of the source, we used a higher threshold for the “good scans” in MIA (60 – 70 %). In all cases, small differences at the level of 10 – 20 % in the calibrated visibility are present. In particular, on the night of 2006 July 12, EWS yields a lower visibility at short wavelengths. After different checks, the problem seems to be the fixed mask used to extract the signals with EWS. Both the bidimensional interferometric and photometric signal are slightly offset compared to the position of the EWS mask. For this reason we preferred to adopt the mask computed by MIA. With this procedure the two data reduction packages produce very similar results which are consistent with a precision of $\lesssim$ 10%.

5.4 Data analysis

The quantity measured by an interferometer is the Fourier transform of the brightness distribution, i.e. the complex visibility. Due to atmospheric turbulence, however, the phase of this complex number is corrupted and cannot be retrieved. The amplitude of the complex visibility – the visibility – can be measured and is compared to the corresponding quantity of theoretical brightness distributions. The visibility is a two-dimensional function in the so-called u, v-plane, where u and v are the spatial frequencies B/λ (B is the baseline length between the two telescopes, and λ the wavelength) in two perpendicular directions. In the case of VLTI/MIDI, a single observation covers a range of spatial frequencies due to the spectral capability of the beam combiner. However, one should keep in mind that the brightness distribution of the target may vary from wavelength to wavelength.

Figs. 5.3, 5.4 & 5.6 show the calibrated MIDI visibilities of HD 101412, HD 135344 B and HD 179218 respectively. We plot the visibility versus spatial frequency rather than wavelength, in order to make a direct comparison to the spatial distribution of the [O I] emission measured at 6300Å. For convenience, we plot the MIDI wavelength scale at the top of the figure. The slope of the visibility curve in the N-band depends on: 1) the increase in spatial resolution with decreasing wavelength and 2) the wavelength-dependence of the brightness distribution.

The [O I] visibility curves (dashed line) are calculated from the radial intensity profile presented in paper I and are discussed later in the text. The comparison of MIDI observations and [O I] visibility is presented in Sec. 5.5. In this section we use a simple geometrical model aimed at deriving the geometrical properties (inner and outer radius, inclination and position angle) of the (mid-infrared) dust emitting region in the three protoplanetary disks.

5.4.1 Uniform ring model

In first approximation the brightness distribution of a protoplanetary disk might be described by a uniform bright ring (UR). The formalism of the UR model is described in Chapter 2. We emphasize that the UR model is a simple geometrical approximation of the dust emitting region. This model does not take into account the physical properties of the circumstellar disk (e.g. dust sublimation radius, disk outer radius, temperature gradient) neither the dust properties (e.g. grain size). Such a model has been extensively used as an analytic model for near-infrared interferometric observations of disks around young stars (e.g. Millan-Gabet et al. [110], Eisner et al. [41], [42]) as well as mid-infrared interferometric data of planetary nebulae (Chesneau et al. [27]). The MIDI visibilities were fitted using an inclined uniform ring (UR) model.

We have searched for the best set of model parameters by minimizing the χ^2 of the visibility measurements. The values of the best fit parameters and associated errors were computed using a Monte Carlo simulation. Assuming a normal error distribution of the measured visibility, we simulated 100 random datasets around the observed values. The best fit parameters and errors correspond to the mean and the standard deviation of the 100 fits.

5.4.2 HD 101412

HD 101412 (Fig. 5.3) is barely resolved at all epochs. Along all the three baseline position angles the visibility is lower at short wavelength and increases from 8 μm to 9 μm – 10 μm. Differences in the absolute value and shape in the three measurements may suggest an asymmetric emission. In particular, HD 101412 is more resolved (i.e. shows a more extended emission) with the shortest baseline, 43 m at 30°. Along this direction the visibility goes from

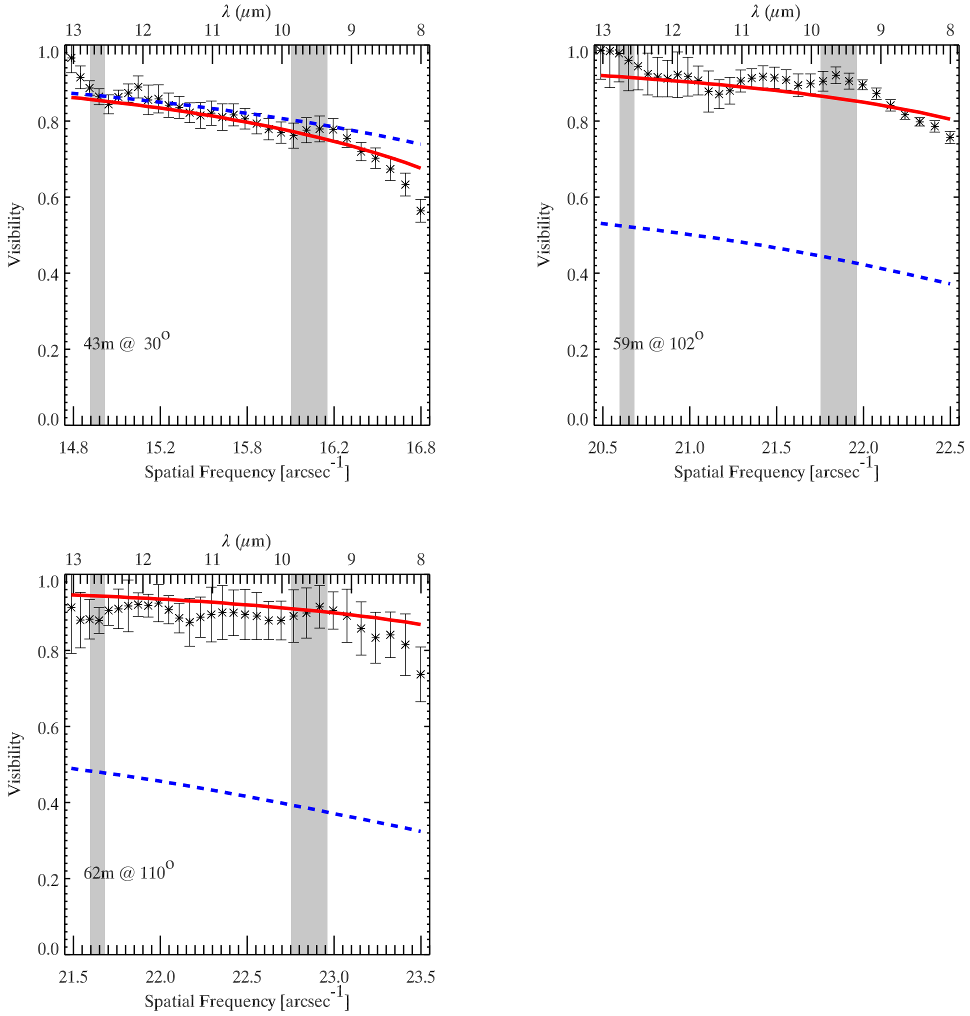

Figure 5.3: Calibrated visibility amplitude at different baselines for HD 101412. The dashed line in the visibility panel represents the visibility computed from the intensity-versus-radius profile of the [O I] 6300Å emission line. The solid line is the best fit of the inclined UR model. Visibility errors are computed as standard deviations resulting from calibrations with different calibrator stars.

0.55 at 8 μm to 0.9 at 13 μm. Around 11.3 μm the disk appears larger than at adjacent wavelength (small dip in visibility). This coincides with a PAH emission. The high visibility values suggest a compact (mid-infrared)

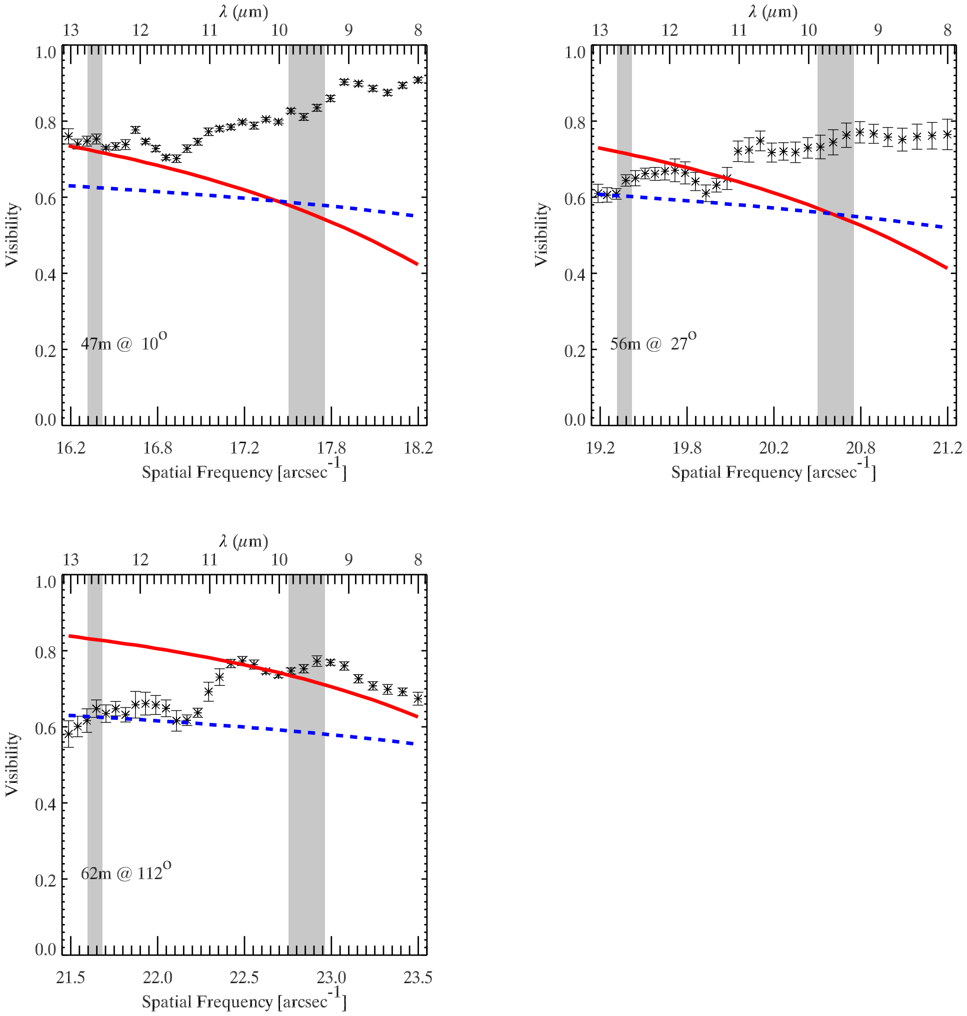

Figure 5.4: Same as Fig. 5.3 for HD 135344 B.

dust emission. The decreasing visibility with decreasing wavelength is due to the increase in spatial resolution. The three visibility measurements of HD 101412 are best fitted by a UR model (Fig. 5.3, solid line) of inner and outer radius respectively of 0.4 and 1.9 AU, an inclination of 80° and position angle of the disk major axis of 38°. The almost edge-on orientation found here explains why the [O I] line profile shows structures which are not seen in other [O I] profiles of Herbig stars; thanks to the high inclination, the projected velocities are close to the real velocities, and the Doppler-induced

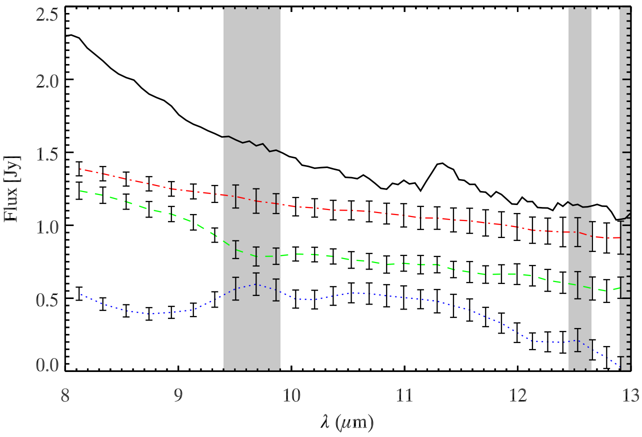

Figure 5.5: Correlated spectrum of HD 135344 B measured on 2006 May 13 (dotted), 2006 June 13 (dashed) and 2006 July 12 (dot-dashed). The spectra were shifted for clarity. The mean, single telescope, spectrum is also plotted (solid line). The absence of the PAH emission feature at 11.3 μm in the correlated spectrum is a signature of spatially extended PAH emission compared to the continuum emission.

spread in the spectrum is optimal.

According to the classification of Meeus et al. [108], the SED of HD 101412 suggests a self-shadowed disk geometry. In this case the mid-infrared disk emission is expected to arise only from the inner rim of the disk. This is consistent with the small size measured with MIDI.

5.4.3 HD 135344B

HD 135344 B is resolved with all baselines (Fig. 5.4). Along the 47 m baseline (position angle 10°) the visibility decreases with wavelength. Along the second and third baselines, 56 m and 62 m respectively, the visibility shows a similar shape: nearly constant between 8 μm – 11 μm with a small bump around 9.2 – 9.4 μm, a drop at 11.3 μm and almost constant at longer wavelength. Despite the higher resolution, the source is less resolved at short wavelengths. This means that at longer wavelengths the target is significantly more extended due to emission of the colder outer disk which only starts to show up at these wavelength. This specific pattern is sometimes observed in mid-infrared interferometric observations of young, PMS stars (e.g. V1647 Orionis, Abraham et al. [2]; FU Orionis, Quanz et al. [130]). Reasonable

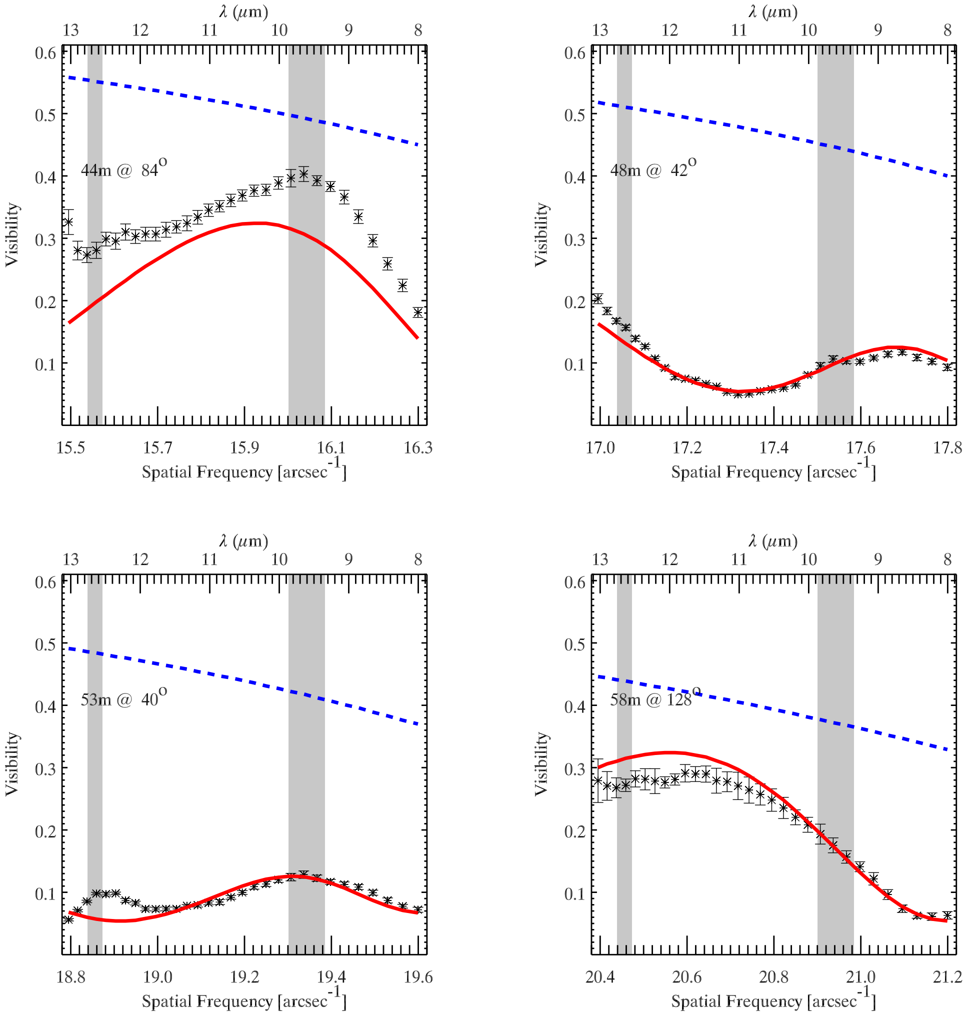

Figure 5.6: Same as Fig. 5.3 for HD 179218. The continuous line here represents the best fit two-component disk model.

fitting of this visibility shape is obtained with a (physical) Keplerian, flared disk model where temperature and surface density are prescribed by a broken power law distributions ($T \propto r^{-q}$; $\Sigma \propto r^{-p}$), i.e. the disk's surface is cooler at larger radii. The result of the UR model (Fig. 5.4, solid line and Table 5.3) are: inner radius 0.05 AU, outer radius 1.8 AU (assuming a distance of 140 pc van Boekel et al. [148]), inclination 60 ° and position angle of the disk major axis 180°. The inclination found here is slightly higher than the result

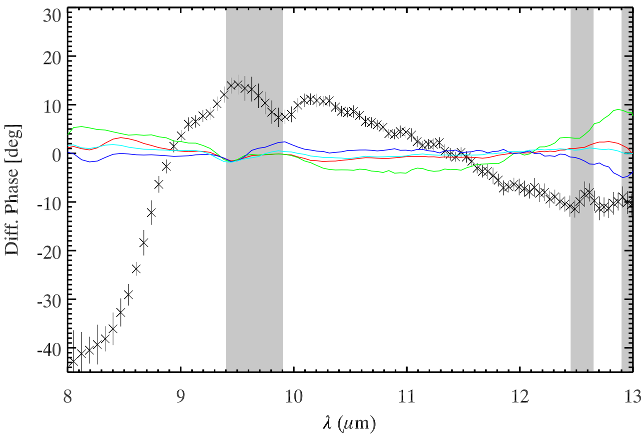

Figure 5.7: Differential phase of HD 179218 measured on 2006 May 16. A 55° phase variation is detected at short wavelength. The four continuous lines are the differential phases for four different calibrators observed during the same night. The plotted phases are not corrected for the effect of water vapor in the delay lines of the VLTI. See Sec. 4.4.1 for details.

of Doucet et al. [35] (45°), obtained with direct imaging at 20.5 μm. Dent et al. [33] modeling the J=3-2 transition of ^{12}CO find a smaller disk inclination (11°, disk nearly face-on). Nevertheless, the UR model is not able to reproduce the decreasing visibility observed with MIDI and the disk parameters are not well constrained.

We converted the MIDI visibility to the Gaussian full-width-half-maximum (FWHM) at each spatial frequency. The FWHM represents the extent of the emitting region and is defined as:

$$\theta = \sqrt{\frac{ln(V(sf))}{-3.56 sf^2}} \tag{5.1}$$

where $V(sf)$ is the MIDI visibility at spatial frequency sf. We want to stress that a Gaussian distribution is only a crude approximation of the real brightness distribution valid at high visibilities. Similarly to Quanz et al. [130], we also fitted the FWHM measured on each baseline with an ellipse wavelength by wavelength. The best-fit ellipse parameters at three reference wavelengths (9 μm, 11 μm, 12.5 μm) are listed in Table 5.4. As expected, the disk looks larger at longer wavelength. The ellipse semi-major axis increases from 1.1 AU at 9 μm to 1.9 AU at 12.5 μm. Inclination and position angle varies by $\sim$ 5° and $\sim$ 9°respectively from 9 μm to 11 μm. The 11 μm and

12.5 μm ellipses have similar (within $\sim 3°$) inclination and position angle. The geometry of the mid-infrared dust emission derived with the UR model and the ellipse fitting are consistent between each other.

The SED of HD 135344 B is characterized by a relatively low infrared excess over the stellar photosphere up to 13 μm and by a strong infrared excess beyond 14 μm. Moreover, the mid-infrared spectrum (Fig. 5.2) lacks silicate features and only weak PAH emission is detected. Such an SED is peculiar among group I sources and suggests a more complex disk structure. The missing near- to mid-infrared excess and the fast increase at longer wavelength has been attributed to the presence of a large dust-free gap by Brown et al. [22]. They proposed a so-called "cold disk" structure for the material around HD 135344 B. In their model the disk is devoid of dust between 0.45 AU – 45 AU (in radius). According to Brown et al., warm dust is present in an inner ring between 0.18 AU – 0.45 AU. The MIDI observations presented here are consistent with this model. The Gaussian FWHM, if scaled to the distance adopted by Brown et al., yields an emitting region between 0.4 – 0.7 AU. Although these radii are larger than those found by Brown et al. (note that we used a simple Gaussian model), the two estimates agree within the uncertainty of the data and the analysis.

Because MIDI is only sensitive to dust emitting at 10 μm, our data set does not allow us to claim the presence or absence of cold matter beyond the inner warm disk. The shadow of the inner disk may obscure a large portion of the disk which re-emerges only at large radii. Both the SED and MIDI observations are only sensitive to the dust emitting in the mid-infrared, both the SED and our MIDI observations are not able to distinguish between a (partially) self-shadowed disk and a disk with a gap.

The correlated spectrum of HD 135344 B for the different measurements is plotted in Fig. 5.5. At all epochs the correlated spectrum mimics the total (single-telescope) spectrum, although deviations are visible. The 11.3 μm PAH emission detected in the total spectrum is not present in any of the correlated spectra which indicates that the PAH 11.3 μm emission regions is completely resolved out at the angular resolution of our measurements.

5.4.4 HD 179218

Despite being the most distant object of our sample, HD 179218 is the most spatially resolved source of the three objects. The visibility varies with the position angle of the baseline and is always below 0.4. Along the first baselines the visibility increases rapidly from 8 to 9 μm and decreases afterwards. Along the second and third baselines (48 and 53 m), the visibility is much lower and shows a characteristic sinusoidal modulation. In the last case, the visibility increases from very low value, 0.05 at 8 μm to 0.27 at 11.7 μm an decreases afterwards.

A sinusoidal pattern of the visibility is produced if the brightness distribution of the target displays sharp edges, e.g. in the case of a ring, uniform disk or a binary with two unresolved components. A smooth emission region, such as a Gaussian disk, would not produce such variations. We can immediately exclude the binary hypothesis: the MIDI observations of HD 179218 cover a range in position angles over 90° and the visibility always shows a sinusoidal pattern. In case of a binary, the pattern is PA dependent and completely disappears when the PA of the baseline and that of the binary axis are aligned. We attempted to fit the MIDI visibility with the UR model but although this model is able to reproduce the sinusoidal modulation of the visibility, it fails to reproduce the visibility at the position of the local "minima". In correspondence of the minima the ring model is zero while the observed visibility reaches a minimum value of $V = 0.05$. If these were "true" zeroes of the visibility, i.e. the location between two adjacent lobes of visibility curve, we would have measured a contrast of $V \sim 0.0076$[4]. We then attempted to fit the data with a two-component model. The first component represents the disk emission at small radii and the second component represents the disk surface at larger radii. Our simulations showed that the first component is only barely resolved. We used a uniform ring for both the internal and external component. Using a different brightness distribution for the internal component does not improve the model fitting. The fractional flux contribution of the first component, f_{int}, was left as a free parameter in the fit. For simplicity, f_{int}, was assumed to be constant at all wavelengths. The best fit parameters are listed in Table 5.5. Inclination and position angle are in agreement with those found with the single ring model ($i = 57°$, PA = 198°). The inner component contributes 20% of the total mid-infrared flux. According to this model, the disk around HD 179218 is either truncated or obscured by its own shadow between 3.2 and 14.5 AU radii from the star (Table 5.5).

Previous infrared interferometric observations of HD 179218 have been carried out by by Leinert et al. [97] and Liu et al. [100] in the mid-infrared and by Monnier et al. [113] in the H-band. Leinert et al. also measured low visibilities with an 80 meters baseline length. Monnier et al. [113] measured a squared H-band visibility of the order of 40%, corresponding to a Gaussian FWHM of 3.8 AU. This is in good agreement with our two-component model, where the inner component extend up to 3.5 AU from the star. Liu et al.

---

[4] This value, given the finite band-width of the MIDI wavelength bins, corresponds to the visibility null reachable by the interferometer in low spectral resolution (PRISM).

modeled MMT nulling interferometric data by means of a ring of diameter 27 ± 5 AU. This large ring is, within uncertainties, consistent with the outer ring of our two-component model.

The agreement between the MIDI data with the simple geometrical model proposed here is quite good. However, deviations from the model are clearly visible. Concerning the nature of the gap, similarly to HD 135344 B, we caution the reader that our observations are not able to distinguish between a real gap (i.e. a region free of material) and a shadowed region.

Differential phase

As a byproduct of the EWS data reduction software, the relative phase between the different spectral channels of MIDI can be retrieved. This so-called differential phase is the real differential phase of the target on the sky, modulated by the atmosphere. The largest effect of the latter is an offset of the differential phases, which is linear with respect to wavenumber ($\propto \lambda^{-1}$). The EWS software subtracts the best-fit linear component of the measured differential phase, as this information is lost anyway. Secondary atmospheric effects remain: the two light beams, coming from the two telescopes, pass through different amounts of air and water vapor before they reach the MIDI beam combiner. However, these smooth variations in the measured differential phase are of the order of a few degrees. For all targets the differential phase is nearly constant with wavelength and centered at zero degrees. The only exception is the measurements of HD 179218 on 2006 May 16 (Fig. 5.7). Along this baseline, a large phase variation is detected at short wavelengths. The phase varies by 55° between 8 and 9 μm. A flip of 180° is expected when the visibility amplitude crosses a null, i.e. when the spatial frequencies covered by the observations are located between two adjacent lobes of the visibility curve. In the case of HD 179218 the phase variation is smooth with lower amplitude. The phase variation is then ascribed to a shift of the photo-center of the emitting source. This suggests a deviation from centro-symmetric emission along this direction.

The differential phase plotted in Fig. 5.7 was not calibrated for the effect of water vapor that is present in the delay line tunnel of the VLT interferometer. The two light beams most likely pass through a different amount of air and water vapor before to reach the MIDI beam combiner. This difference introduces an instrumental differential phase. Fig. 5.7 also shows the differential phase measured with four different calibrators observed during the same night with the same acquisition mode (SCI PHOT). Since calibrators are (usually) point-like their differential phase should be zero. The deviation from zero degree in this case is produced by the water vapor. The effect of water vapor

Table 5.3: Best fit parameters of the UR model for HD 101412 and HD 135344 B. R_{in} and R_{out} are the inner and outer ring radii and are given in milliarcsec (first row) and AU (second row). The last column lists the value of the reduced χ^2. Value close to one indicates a good agreement between model and observations.

Star	R_{in} [mas]/[AU]	R_{out} [mas]/[AU]	i [°]	ϕ [°]	$\tilde{\chi}^2$
HD 101412	2.5 ± 0.6	11.9 ± 0.6	80 ± 7	38 ± 5	0.4
	0.4 ± 0.1	1.9 ± 0.1			
HD 135344	0.35 ± 1.79	12.8 ± 1.4	60 ± 10	180 ± 60	3.9
	0.05 ± 0.25	1.8 ± 0.2			

Table 5.4: Best-fit ellipse parameters for HD 135344 B. The ellipse is fitted to the FWHM measured on the three baselines. Ellipse axis are computed assuming a distance of 140 pc.

Wavelength	9 μm	11 μm	12.5 μm
Semimajor axis [AU]	1.1	1.5	1.9
Semiminor axis [AU]	0.6	0.8	0.9
Inclination [°]	53	58	61
Position angle [°]	171	163	163

is present, but very small compared to the phase variation observed toward HD 179218.

The variation in the differential phase along the 58 m baseline is caused by asymmetric emission. This is in agreement with the inclination of the disk (57°) and its flared structure. Due to the flaring, the far side of the disk emits more light in the direction of the observer. This means that the photo-center of this emission (described here by the ring) is no longer coincident with the photo-center of the almost unresolved inner disk. It is difficult to derive a quantitative estimate for this offset, mainly due to the loss of the linear differential phase information. Estimating from the magnitude of the differential phase variation (∼60°), it must be around 4±2 mas.

5.4.5 Extended PAH emission

Emission from Polycyclic Aromatic Hydrocarbons (PAHs) is typically detected towards disks around Herbig stars (e.g. Meeus et al. [108]; Acke & van den Ancker [3]; Sloan et al. [142] & Geers et al. [48]) and in some T Tauri stars (e.g. Geers et al. [47], [48]). PAHs are heated by UV-photons

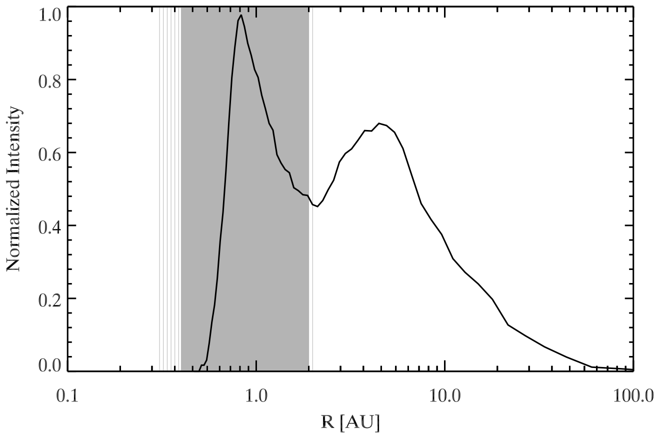

Figure 5.8: Normalized [O i] 6300Å intensity profile for HD 101412. $I_{[OI]}$ $(R) \times S(R)$ is the total [O i] line luminosity in a ring at distance R from the star. This was obtained averaging the result of observation $B1$ and $B2$ of paper I. In the specific case of HD 101412 $I_{[OI]}$ (R) was recomputed with an inclination of 80°. The filled region represents the position of the dust emission region as determined by MIDI. The striped regions indicate the uncertainty on the latter.

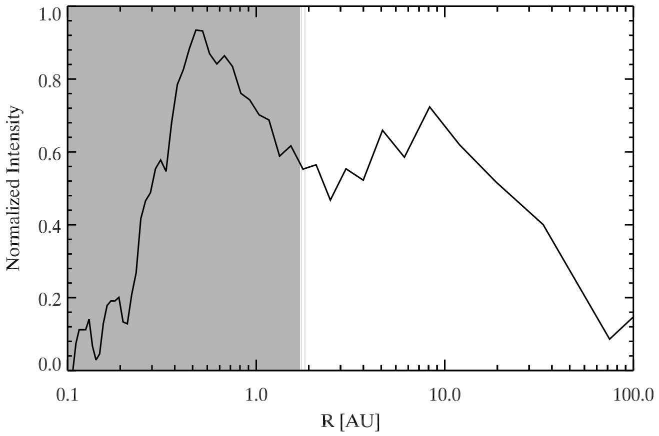

Figure 5.9: Same as Fig. 5.8 for HD 135344 B.

Table 5.5: Best fit parameters and standard deviation of the two-component disk model for HD 179218. Radii are given in AU assuming a distance of 240 pc. Inclination and position angle of the two components were assumed to be equal for both structures. f_{in} is the fractional contribution of the inner component to the total flux in the mid-infrared.

HD 179218	
1^{st} component: R_{in} (AU)	0.3 ± 0.1
1^{st} component: R_{out} (AU)	3.2 ± 0.1
2^{nd} component: R_{in} (AU)	14.5 ± 0.5
2^{nd} component: R_{out} (AU)	22.6 ± 0.4
inclination (°)	57 ± 2
PA (°)	23 ± 3
f_{in}	0.2 ± 0.02

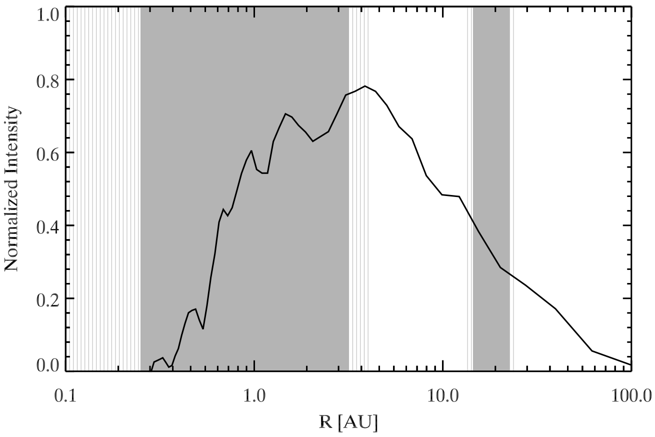

Figure 5.10: Same as Fig. 5.8 for HD 179218.

from the central star. In many cases, the PAH emission is found to be spatially extended (e.g. van Boekel et al. [147]; Habart et al. [57], [58]; Visser et al. [152]; Doucet et al. [34] & Boersma et al. [18]). In particular, in Herbig stars, the PAH emission is more extended than the continuum (at similar wavelengths) and can be as extended as the total size of the disk (Visser et al. [152]). In disks around less massive stars, given the lower UV flux, the emission is weaker and more compact around the central star. Three PAH emission features are present in the spectral range covered by our observations centered respectively at 8.6 μm, 11.3 μm and 12.7 μm. All the three sources we study here show evidence of emission of (at least one of) these features (e.g. van Boekel et al. [148] and figure 1). The PAH emitting region may be much larger than the continuum/silicate one (Sect 4.2). As a consequence, at the position of the PAH emission there are (at least) two visibility components which contribute to the MIDI observed visibility. Depending on the relative contribution of PAH emission to the total flux at a specific wavelength, the total visibility tends to be lower due to the presence of the extended PAH emission. Given the contamination of telluric absorption in correspondence of the 12.7 μm emission band, we will not take this feature into account in our analysis. The main findings that emerge from the analysis of the MIDI visibility and correlated flux are:

PAH 8.6 μm feature

1. **HD 101412**: The visibility increases monotonically between 8 μm and 9 μm and the disk appears slightly more extended shortward of 9 μm than at 10 μm. This may be a signature of extended PAH emission

2. **HD 135344 B**: No evidence of 8.6 μm emission in the total spectrum nor in any of the correlated spectra

3. **HD 179218**: The visibility is systematically low shortward of 9 μm. However, it is not clear whether this just reflects the characteristic sinusoidal modulation of the “ring-like” structure or whether it is the PAH emission that causes this effect

PAH 11.3 μm feature

1. **HD 101412**: A drop in the visibility of HD101412 around 11.3 μm is detected along the second baseline (59 m, 102°). This is also the observation with the best signal-to-noise ratio for HD 101412. A similar trend is visible along the third baseline (62 m, 110°), although the large error bars make this detection uncertain. HD 101412 is classified as a group II (self-shadowed) disk. The detection of PAH emission more extended than the dust emitting region is peculiar for such a disk structure. The UV-excited PAH molecules should lie in a dust-free surface layer of the disk. This source has a strong [O I] 6300 Å emission – equally unusual for a group II source – which led van der Plas et al. [150] to consider HD 101412 to be somewhat transitional in character between group I

and group II.

2. **HD 135344 B**: A clear drop in visibility in the vicinity of 11.3 μm is detected with MIDI with all baselines. This is even more clear in the correlated flux (Fig. 5.5): no emission is detected in the four measurements of the correlated flux, indicating that the 11.3 μm PAH emission comes from spatial scales larger that those resolved by MIDI.

3. **HD 179218**: No detectable variation of the visibility is visible in the MIDI observations of HD 179218 around 11.3 μm. This disk is classified as a group I source (flared). The flaring geometry and the large dimension found for the dust emitting region may suggest that in this case dust and PAHs have a similar extent.

5.5 Comparison to the optical gas emitting region

In paper I very high resolution optical spectra of HD 101412, HD 134355B and HD 179218 were presented. In all three targets, we spectrally resolve the [O I] 6300.304Å emission line. Assuming that the disk is in Keplerian rotation, the [O I] emission line profile can be translated into a radial profile, i.e. the Intensity-versus-Radius, $I_{[OI]}$ (R), curve of the oxygen line emission. Figs. 5.8, 5.9 and 5.10 show the normalized [O I] radial profile derived in paper I: $I_{[OI]}$ $(R)\times S(R)$, where $S(R) = \pi(R_{out}^2 - R_{in}^2)$ and R_{out} and R_{in} outer and inner radius of the ring at radius R. $I_{[OI]}$ $(R) \times S(R)$ is the total luminosity in a ring at distance R from the central star. The [O I] radial profile shown here is based on the average of the spectra presented in Paper I. In the case of HD 101412, $I_{[OI]}$ (R) was recomputed using a disk inclination of 80° to be consistent with the result of Sec. 5. Using a larger inclination has the effect to shift the emission further away from the star as can be seen comparing Fig. 5.8 with Fig. 11 of paper I. The filled region represents the position of the dust emission region as determined by MIDI. The striped regions indicate the uncertainty on the latter.

In order to compare the [O I] result with the dust one we need to provide a visibility model to the MIDI observations. From $I_{[OI]}$ (R), it is possible to derive a brightness distribution ($I_{[OI]}$ (α, β), with α and β angular distance from the central star) assuming that the line emission from the disk surface is axis-symmetric. Using $I_{[OI]}$ (α, β) as brightness distribution, the visibility model ($V_{[OI]}$ (u, v)) was computed. The expected visibility at the spatial frequencies mapped with MIDI was computed interpolating $V_{[OI]}\ (u, v)$ at the corresponding positions in the uv-plane. The dashed line in Figs. 5.3, 5.4 & 5.6 is $V_{[OI]}\ (u, v)$ at the spatial frequency covered by MIDI observations.

5.5.1 HD 101412

As shown in Fig. 5.3, $V_{[OI]}\ (u, v)$ is similar to the observed visibility along the first baseline (43 m, 30°) and is clearly lower than along the other two directions. This is more clear when looking at Fig. 5.8. The dust emission is located within ~ 2 AU, while the gas emission appears more extended with a bright peak at $\sim 5 - 6$ AU. In terms of radial extent, this means that the [O I] emission extends to larger radii than the mid-infrared emission. Beyond the first peak the [O I] intensity drops off as one would expect for a self-shadowed disk. The second peak at larger radii may be due to the presence of a gas layer above the dust disk. The gas in the disk appears to emerge from the shadow at larger radii, while the dust disk does not.

5.5.2 HD 135344 B

The main difference between model and observations is the shape of the visibility. As shown in Fig. 5.4, $V_{[OI]}\ (u, v)$ increases with wavelength, while the observed visibility is always decreasing. However, despite the difference in shape, the absolute values of model and observations do not differ from each other significantly and in some cases are consistent. The bulk of the oxygen emission is produced within few AU from the central star similarly to the mid-infrared dust emission (Fig. 5.9). A tail of the gas emission is visible at larger radii, but the intensity is much lower.

5.5.3 HD 179218

As shown in Fig. 5.6, the [O I] model is not able to reproduce the observed visibility of HD 179218. The observed visibility is in all cases lower than $V_{[OI]}$. Moreover, the oxygen model increases with wavelength while the observed visibility shows a sinusoidal variation. The [O I] intensity peaks at 3 – 4 AU (Fig. 5.10) and decreases outwards. According to our two-component disk model, emitting dust is present within the "oxygen peak". A further contribution to the mid-infrared emission, 80% in terms of flux, comes from a ring located between $\sim 15 - 23$ AU. At this distance, the [O I] line intensity is reduced. The more compact gas emission might be due to a true absence of gas in the surface layers of the outer disk, or to chemical effects which reduce the abundance of the OH molecule. The [O I] intensity depends on the OH abundance. If OH is efficiently destroyed through the gas-phase chemistry occurring in the upper layers of the disk, we would not see [O I] emission, whereas plenty of gas could still be present. A contrast effect of the [O I] emission may also play a role. In this case the [O I] emission is much stronger in the inner disk and it may outshine the [O I] from the outer disk.

Our result is consistent with a flared geometry for the disk around HD 179218; the inner, curved, rim is represented by the inner UR while the outer UR may represents the flared disk surface at larger radii. The two dust emission regions are separated by a “dark” (non emitting) region.

5.6 Discussion and conclusion

In this paper we presented the first direct comparison of gas and dust emission from the surface of three protoplanetary disks. This work present the state-of-the-art of observational techniques in this field. The comparison of high optical spectroscopy with infrared interferometric observations gives some insight on the relative size and shape of the gas and the dust emitting region. Only in one case (HD 135344 B) we find the two regions to overlap. In the other two cases (HD 101412 and HD 179218) clear differences are found. In this section we summarize the main results of this analysis and discuss them in context of disk structure and evolution.

A good agreement between the MIDI visibility and the oxygen model was found for HD 135344 B. The visibility computed from the [O I] emission line matches the observed 8-13 μm visibility. In particular the dust emitting region measured with MIDI is rather compact. This result is consistent with the “cold disk” model proposed by Brown et al. [22]. Given the similarity with the MIDI visibility, the bulk of the gas emission and of the mid-IR emission are likely produced in a ring-like structure close to the star (within ~ 1.8 AU). Evidence of extended PAH emission is found. Fig. 5.11 shows a sketch of the disk around HD 135344 B. Beyond the inner, hot, ring of dust and gas the disk is characterized by a large gap. The disk flares up at larger distance, as shown by direct imaging at 20 μm.

For HD 179218 we found that the oxygen emitting region is more compact than the mid-IR emitting region, dominated by dust. The four MIDI visibility amplitudes presented here reveal a disk structure much more complex than the simple ring model. The sinusoidal modulation of the visibility amplitude and the large phase variation ($\sim 60^\circ$) are in good agreement with a flared disk structure with a gap in between the hot inner disk and the flared outer parts. From our dataset we are not able to determine whether the difference between gas and dust emitting regions reflects a real different structure for the two components or whether this is caused by others effects such as: 1) the action of chemical processes which reduce the abundance of OH in the outer part of the disk (in this case plenty of gas may still exist but we are not able to see it) or 2) a contrast effect of the [O I] emission. In the latter case the [O I] emission is much stronger in the inner disk and it may outshine the [O I] from the outer disk. The sketch drawn in Fig. 5.11 shows the structure of the disk around HD 179218. The disk is large and flared. A gap – or shadowed region – is also present.

In the case of HD 101412, we find that the gas emitting region is larger than that of the dust. The same result is found for the PAH emission. According to the phenomenological classification of Meeus et al. [108], HD 101412 is a group II source, i.e., the disk is flat and self-shadowed. At the truncation radius, the disk is puffed-up and shadows the outer disk. The shadowed region is not reached by the stellar UV radiation. The intensity versus radius profile of the [O I] 6300 Å line (Fig. 5.8) is consistent with such a disk geometry. Nevertheless, the presence of a second bump in the oxygen emission (beyond the inner rim) is not expected for a self-shadowed disk. This, together with the MIDI result might be the signature of a different scale height, and hence vertical structure, between gas and dust in the shadowed region. This means that – in this object – gas and dust are decoupled in the surface layers of the disk allowing the gas to emerge from the shadow of the inner rim. This is shown in the schematic diagram of Fig. 5.11. The dust-depleted surface layer of the disk combined with the dust grains settling, increases the dust-to-gas ratio in the midplane. This observational evidence strengthens the hypothesis of van der Plas et al. (paper I) that HD 101412 is a transitional object between groups I and II.

The gas-dust decoupling may have an important role in disk evolution, as this may be a self-enhancing process. Once the gas and dust start to decouple in the upper surface layers, the dust-gas ratio in the midplane of the disk increases. In turn, this enlarges the region where gas and dust are decoupled. This scenario would transform a group I (flared) disk into a group II (flat) disk. This is shown in Fig. 5.11. We thus suggest that HD 179218, HD 135344 B and HD 101412 may form an evolutionary sequence. The disk is initially flared. Once gas and dust decouple in the disk surface layer, the dust grains settle towards the mid-plane. This may lead to the formation of transitional disk structure such as that of HD 135344 B. The dust settling favors the physical separation between gas and dust until all the dust settle towards the mid-plane (Dullemond & Dominik [38]) leaving, eventually, a region of gas in the upper layers of the disk similar to HD 101412. Interestingly, Acke et al. [3] already found that cold grains in the mid-plane of the disk have grown to considerably larger sizes in Meeus et al, group II sources than in group I sources, suggesting that disks may evolve from a flared to a self-shadowed geometry. Similarly Bouwman et al. [20] find a correlation between the strength of the amorphous silicate feature and the shape of the SED, consistent with the settling of dust as a consequence of grain growth. What we add here to this picture is a completely independent piece of evidence supporting this and perhaps the identification of the driving mechanism of this process. Finally, we note here that the gas-dust coupling may be crucial for the formation of planetesimals. If the dust-to-gas ratio is higher than a critical value (2-10 times the typical value of the interstellar medium), planetesimals may form by gravitational instability (Johansen et al. [77]; Youdin & Shu [157]). Youdin & Shu [157] also find that colder disks with less pressure support, such as the shadowed region, require less enhancement of the dust-to-gas ratio to trigger gravitational instability.

Although the sample of systems studied here is too small to be able to draw firm statistical conclusions, it appears that that the degree of gas-dust decoupling in the surface layers of the disk varies from object to object. In particular, the decoupling may have a crucial role in the disk evolution and on the formation of planetesimals by gravitational instability. Next generation disk evolution and planet formation models should take into account this phenomenon.

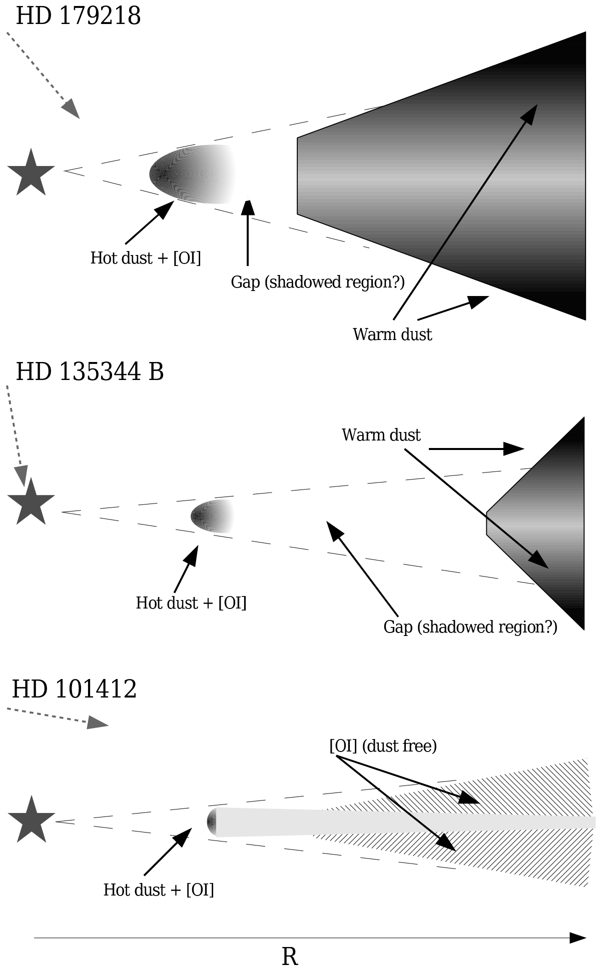

Figure 5.11: Simplified sketch of the disk around the three program stars. The regions where the dust and [O I] emissions are expected to arise are indicated. The inclination of the disk with the line of sight is shown by the dashed arrow at the upper-left corner. The vertical arrow on the left indicates the direction of the disk evolution. *HD 179218*: the disk is large and flared. A gap (or shadowed region) is located beyond 3 and 15 AU from the central star. Most of the silicate mid-infrared emission arise from the warm dust located in the surface layers of the outer part while the gas emission is mainly confined to the inner, curved, rim of the disk. *HD 135344 B*: the disk is seen almost face-on. The bulk of the dust and gas ([O I] 6300Å) emission comes from a compact ring close to the star. A large gap (or shadowed region) separate the inner ring from the outer disk. The latter is responsible for the infrared excess beyond 14 μm. *HD101412*: a compact dust ring which faces directly the star is responsible for the mid-infrared excess visible in the SED. The [O I] 6300Å line arises from the same region. Beyond this ring, the disk is shadowed. A dust-free flaring layer emerges from the shadow at larger radii. In all three cases, gas is likely present within the dust sublimation radius.

6

The Timescale of Gas Dispersion in Protoplanetary Disks: How Long Does It Take to Form a Planet?

This chapter presents the preliminary results of an optical spectroscopic campaign of young stellar clusters (3 - 80 Myr) aimed at tracing the evolution of mass accretion in PMS stars. This study is fundamental to understanding the evolution of viscous accretion during the pre-main-sequence stellar evolution. Measuring the time at which mass accretion ceases, allow to constraint the timescale for gas dissipation in disks, and in turn, on the time available to form planets.

6.1 Introduction

Star forming regions show a steady decline with time in the fraction of stars having infrared excess emission (e.g. Bouwman et al. [19]; Haisch et al. [60], Fig. 1.7). The growing consensus, based on infrared observations, is that the inner disk is cleared of the the small, warm dust grains within the first 5÷9 Myr (τ_{dust}). There is evidence that accretion onto the central star sometimes continues after the inner disk is cleared of dust (e.g. *transitional disks* in Tr 37, Sicilia-Aguilar et al. [138]). This means that gas may still be present in the inner disk also after τ_{dust}. If this is confirmed, the natural question is: why gas and dust have different lifetime in disks? If photo-evaporation and viscous accretion are responsible for disk dispersion, we may expect gas and dust to “disappear” at the same time. However, if coagulation of dust grains in cm-size particles and planetesimals is responsible for dust clearing, then the gas can survive also after τ_{dust}. Little is still know about the timescale for the dissipation of gas (τ_{gas}), even though gas accounts for $\sim 99\%$ of the disk mass and is crucial for building giant planets.

The science goal of this project is to measure the mass accretion timescale in PMS stars. This will result in a strict upper limit on the time available to form planets. Once τ_{acc} is known, the comparison with τ_{dust} give some insight on the role of planet formation in disk dispersion. The fraction of systems with near infrared excess after 5 Myr is $\lesssim 20\%$ (Fig. 1.7). Which is the fraction of accreting objects at the same epoch? For instance, if accretion continues also after the inner disk is cleared of dust, this may suggest that the dust clearing is driven by planet formation. While, if accretion stops at the same age of dust dissipation, then viscous accretion and photo-evaporation may be stronger than planet formation in removing disk material.

The mass accretion timescale (τ_{acc}), i.e. the time at which the disk accretion phase ceases, is a strong constraint on τ_{gas}. Gas may still be present after τ_{acc}, however, the amount of remaining gas, and hence of disk mass, may be too low to be able to form giant planet(s). Two main features are produced during the disk accretion phase: an UV excess and UV/optical emission lines (Sec. 1.2). Both may be used to find evidence of mass accretion. The UV excess may be measured with optical photometry in the U-band. This method is certainly highly efficient because it requires a small amount of telescope time to observe a large number of stars. However, it requires the knowledge of the spectral type of the stars to measure the excess U-band flux. On the other hand, measuring the spectrum of each stars allow a direct and unambiguous identification of ongoing mass accretion in PMS stars. Moreover, the U-band excess is less sensitive than spectroscopy and is applicable only for the younger clusters where disk accretion is expected to be higher.

Among the UV/optical lines, Hα is the strongest line produced in the magnetospheric accretion columns and is easy to detect also for weakly accreting objects. Stars with chromospheric activity may also show Hα emission even without mass accretion. However, chromospheric Hα emission line is limited in strength by the limited amount of gas present, and in width by the stellar rotation and turbulent motion in the chromosphere. On the other hand, the region where mass accretion occur is characterized by higher temperature and velocities (line width is broader).

6.2 Method

In order to measure the timescale of disk accretion in PMS stars in a secure way, we performed an optical spectroscopic survey of a large number of stars towards five different young stellar clusters. Optical spectroscopy allow to detect and measure the Hα emission produced in young stars by accretion of material from the disk. Once the fraction of stars with signature of mass accretion is computed for each cluster, the evolution, and hence, the accretion timescale can be traced. This technique has the advantage that is an empirical estimation and do not require model fitting.

6.2.1 Cluster sample

The following criteria were adopted for the sample selection:

- **age**: the clusters are young ($<$ 100 Myr) and have ages covering the interval 3 – 80 Myr. This age is thought to be relevant for gas (and dust) dispersion in disks as well as for planet formation;
- **distance and extinction**: nearby and optically-visible systems were selected to ensure detection of low mass stars down to spectral type M2 - M4;
- **angular radius**: only clusters with angular size comparable to the total *VIMOS* FOV were considered. This is needed to minimize the number of stellar contaminant within the *VIMOS* FOV.

Table 6.1 lists some properties of the five clusters selected for this project. Apart from the youngest cluster (σ Orionis) the rest of the sample (Bochum 11, ASCC 58, Collinder 65 and NGC 2353) was extracted from the galactic open clusters database WEBDA[1]. The physical parameters (age, distance, diameter and extinction) for σ Orionis were taken from the extensive literature on this cluster. For the remaining clusters, the parameters collected in WEBDA were adopted.

An exception to the selection rules listed above is Bochum 11. Bochum 11 is located in the Carina complex. The distance to the cluster is 3.5 Kpc (Patat & Carraro [126]). The cluster is characterized by a moderate extinction (A_V = 1.8) and diffuse nebular emission. This do not allow us to study the low-mass stellar population of the cluster.

For each cluster an area of $16' \times 18'$ was investigated in order to find stars with ongoing mass accretion.

---

[1] http://www.univie.ac.at/webda/, operated at the Institute for Astronomy of the University of Vienna

Table 6.1: Properties of the young stellar clusters observed with *VIMOS* . From left to right: equatorial and galactic central coordinates of *VIMOS* observations, age, distance and extinction towards the cluster.

Cluster	RA(J2000) [HH:MM:SS]	DEC(J2000) [DD:MM:SS]	l [deg]	b [deg]	Age [log(t(yr))]	Distance [pc]	A_V [mag]
σ Orionis	05:38:00	-02:37:00	206.7411	-17.5088	6.3	360	0.15
Bochum 11	10:47:15	-60:05:00	288.0250	-0.8560	6.7	2412	1.80
ASCC 58	10:15:07	-54:58:12	281.7116	1.3281	7.0	600	0.28
Collinder 65	05:26:05	+15:41:59	188.8613	-10.8582	7.4	310	0.40
NGC 2353	07:14:30	-10:16:00	224.6854	0.3842	7.9	1119	0.22

6.3 Observations and data reduction

6.3.1 Multi-object spectroscopy

Multi-object-spectroscopy (*MOS*) with the *VIsible MultiObject Spectrograph*[2] (*VIMOS*) at *VLT* (Le Fevre et al. 2003 [95]) was performed. *VIMOS* is a visible (360 to 1000 nm) wide field imager and multi-object spectrograph. The instrument is made of four identical arms with each a field of view of $7' \times 8'$ with. The pixel scale is $0\farcs205$. the chips are separated by a gap of $\sim 2'$. The total field of view (FOV) of *VIMOS* is $\sim 16' \times 18'$. However, due to inter-chips gaps, the effective FOV is $14' \times 16'$. Each of the four *VIMOS* arm is equipped with 6 grisms providing a spectral resolution range from $\sim$ 200-2500 and with one EEV CCD 4k×2k. Multi-object spectroscopy is carried out using masks (one per quadrant). We used the grism HR-Orange which covers the spectral range between 520 nm - 760 nm. A maximum number of 40 - 45 slits per (quadrant) may be positioned.

The observations were carried out during the semester October 2006 - March 2007. Three masks per observed regions were used. Each mask contains from 45 up to 152 objects (all quadrants), depending on the stellar density of the observed sky area. For each clusters optical spectra of $\sim$ 200 - 400 representative objects were acquired. The aim of these observations is not at providing a spectrum of each cluster member, but instead at producing a large ($\gtrsim 50$), unbiased sample of cluster members within one field of each cluster.

Single and dithered exposures of 200, 300, 400 and 600 seconds were taken. The mean seeing was $0\farcs86$. A slit width of $1\farcs0$ was selected which gives a spectral resolution of $\lambda/\Delta\lambda = 2150$. Due to distorsion of the instrument, night time wavelength calibration exposures were taken. The log of the observations is reported in Table 6.2.

---

[2] http://www.eso.org/sci/facilities/paranal/instruments/vimos/

Table 6.2: Log of *VIMOS* spectroscopic observations. For each clusters three different slit masks were created.

night	Cluster	mask	exptime [sec]	N_{exp}	seeing [″]	Slit width [″]	$\lambda/\Delta\lambda$	N_{slit}
12 - 13 November 2006	σ Ori	M3	600	3	0.6	1.0	2150	66
25 - 26 November 2006	σ Ori	M1	400	1	1.2	1.0	2150	55
26 - 27 November 2006	σ Ori	M2	600	3	0.8	1.0	2150	95
18 - 19 December 2006	Coll 65	M1	300	2	0.4	1.0	2150	45
22 - 23 December 2006	Coll 65	M2	600	3	1.0	1.0	2150	101
17 - 18 January 2007	Coll 65	M3	600	3	0.7	1.0	2150	52
27 - 28 December 2006	NGC 2353	M2	300	2	0.9	1.0	2150	106
14 - 15 December 2006	NGC 2353	M1	600	3	0.6	1.0	2150	88
18 - 19 January 2007	NGC 2353	M3	600	3	0.9	1.0	2150	122
9 - 10 March 2007	ASCC 58	M1	200	2	1.4	1.0	2150	78
22 - 23 March 2007	ASCC 58	M3	300	3	1.1	1.0	2150	140
23 - 24 March 2007	ASCC 58	M2	300	3	0.9	1.0	2150	152
24 - 25 March 2007	Bochum 11	M1	200	2	1.1	1.0	2150	114
25 - 26 March 2007	Bochum 11	M3	300	3	0.5	1.0	2150	134
–	Bochum 11	M2	300	3	0.6	1.0	2150	145

6.3.2 Data Reduction

The data reduction was performed with the *ESO FORS* pipeline[3] appropriately modified to reduce *VIMOS MOS* data (similar to *FORS MXU* data). The *FORS* pipeline is based on pattern matching technique. The reduction of *VIMOS* multi-object spectroscopy data consists of two steps:

I Finding a model that reproduces the distortion of the instrument in the spatial and dispersion direction;

II Apply the distorsion model to the scientific frames and extract the spectra.

A detailed description of the data reduction procedure may be find in the *FORS* pipeline manual[4]. A brief overview of how the distorsion model is created is provided here:

1. Subtract bias and background from all frames;
2. Run a 1D peak-detection task to produce a list of reference arc lamp lines candidates;
3. Run a 1D pattern-recognition task to identify a number of lines among the input reference line list (not all the lines are used at this stage);

---

[3] http://www.eso.org/sci/data-processing/software/pipelines/

[4] ftp://ftp.eso.org/pub/dfs/pipelines/fors/fors-manual-1.2.pdf

4. Apply a preliminary wavelength calibration;
5. Search for the CCD position of a reference wavelength (all the previous steps are done row by row);
6. Run a 2D pattern-recognition task to match the physical positions of the slits on the focal plane with the positions found on the CCD for the reference wavelength;
7. Trace the edges of each flat field spectrum and fit the trace with a low-degree polynomial;
8. Extract the arc lamp spectra reading the measured spectral curvature;
9. Run a 1D peak-detection task on all extracted spectra to produce a list of reference arc lamp lines candidates from the whole spectral range;
10. Run a 1D pattern-recognition task to identify the lines among the input reference line list;
11. Find the wavelength calibration solution.

The distorsion model is created. In this model each CCD pixel corresponds to a wavelength and to a position on the telescope focal plane. The scientific spectra are extracted applying the distorsion model. Since the instrument is not stable, it is important to acquire the flat-field and arc-lamp exposures as much as possible with the same telescope/instrument configuration as the scientific exposures.

From this point on the data reduction proceeds as in the case of standard long-slit spectroscopy: bias subtraction, wavelength calibration, background removal and spectrum extraction using the Horne optimal extraction method (Horne, K., [69]).

6.4 Data Analysis

The *VIMOS* spectra are generally of good quality. Moderate signal-to-noise ratio (S/N $\gtrsim$ 10) are usually obtained. However for the faint objects (R $\gtrsim$ 18 mag) the S/N is lower ($\sim$ 4). This may prevent the detection of weak Hα emission line in faint stars. However, for a given stellar cluster, the faintest stars are also the lowest-mass one. Due to the contrast effect the equivalent width of Hα for low-mass accreting stars is usually high (Fig. 6.8). Even for the low S/N spectra we should be able to detect stars with ongoing accretion.

Figs. 6.1 – 6.7 show the spectra with detected Hα emission in each cluster. The number of stars with Hα emission varies from region to region: 13 in Sig-Ori, 3 in Bochum 11, 3 in ASCC 58, 1 in Collinder 65 and 7 in NGC 2353.

The data reduction of the *VIMOS* spectra of Bochum 11 are complicated by diffuse nebular emission of the Carina nebula. Some background lines (Hα, [N II] 6548,6583 Å, [S II] 6717,6731 Å) are very strong and the background subtraction often leaves some artifacts.

6.4.1 Star counts

In order to trace the temporal evolution of mass accretion, the number of accreting stars has to be normalized by the number of cluster members. For this purpose we performed star counts. Star counts is a simple statistical analysis widely used to search for region of stellar over-density by simply comparing the stellar density within a sky area and in an offset reference region. For each cluster, a fraction of objects observed with *VIMOS* is formed by field stars belonging to the different sub-structures of the Milky Way. In our case, the main contribution of contamination are stars belonging to the Galactic thin and thick disks.

For each cluster we counted all the stars within a radius of $9'$ centered on the *VIMOS* fields (Table 6.1). For this purpose we used the DENIS[5] catalog. DENIS is a Southern sky survey in the optical $Gunn - i$ (0.82μm) and two near-infrared J (1.25μm) and K_s (2.15μm) bands. The survey was performed with the 1m *ESO* telescope at La Silla (Chile) and is limited to objects with declination $< +2°$. The limiting magnitude are 18.5, 16.5 and K_s=14 mag respectively. The CMD of Bochum 11, ASCC 58 and NGC 2353 shows a second, red, main sequence (Figs. 6.11, 6.12 and 6.15). These three clusters are located in the Galactic plane. The red sequence is likely formed by background stars dimmed by further extinction along the line of sight beyond the cluster. Given its high declination, Collinder 65 is not included in the DENIS database. For this cluster, the CMD was computed from the R and J band using the NOMAD[6] catalog. NOMAD is a collection of optical astrometric and photometric data from various catalogues. It is also supplemented by 2MASS near-infrared photometry, whenever available. Figs. 6.10 – 6.15 show the color magnitude diagram (CMD) of the five *VIMOS* regions.

The equivalent area of the "photometric" survey (254 arcmin^2) is slightly larger than equivalent *VIMOS* field-of-view ($= 4 \cdot 7' \cdot 8' = 224$ arcmin^2). Compared to the *VIMOS* spectra, the CMD are less deep in magnitude by $\sim$ 1 – 2 mag. Apart from that, the two group of stars formed by 1) the *VIMOS*

---

[5] http://webviz.u-strasbg.fr/viz-bin/VizieR-2?-source=B/denis

[6] http://webviz.u-strasbg.fr/viz-bin/VizieR-2?-source=I/297

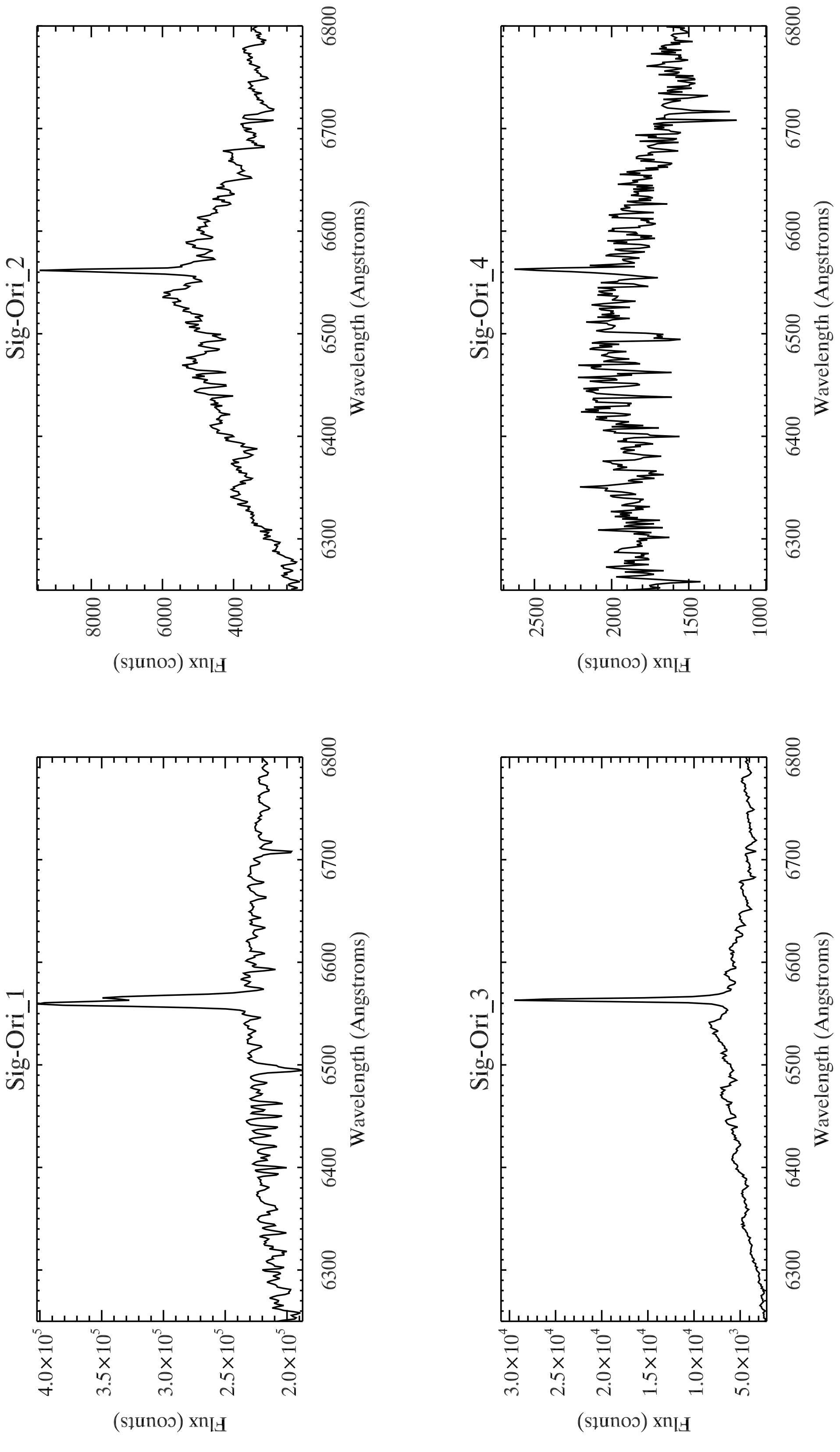

Figure 6.1: *VIMOS* spectra of stars with Hα emission.

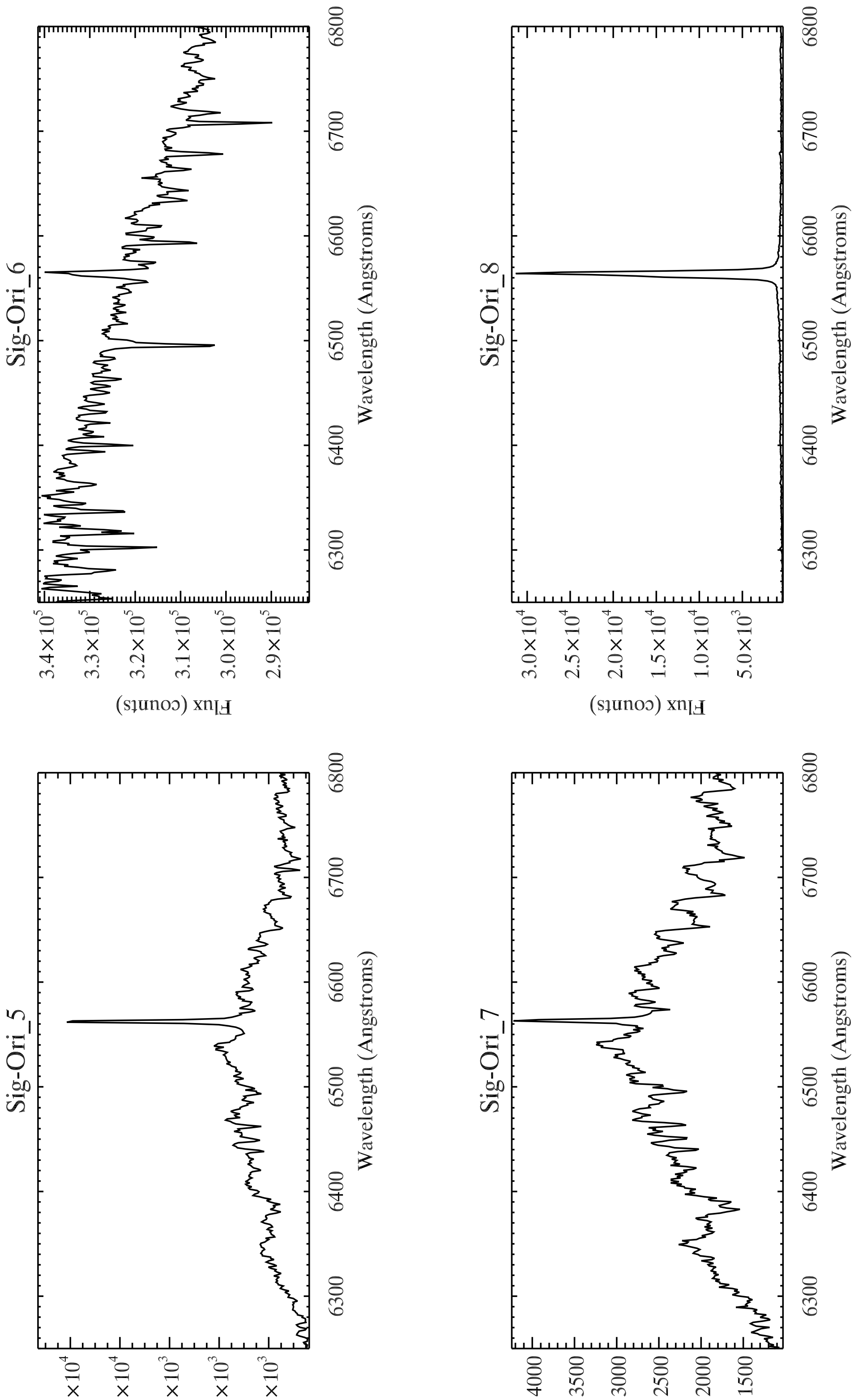

Figure 6.2: Continuation of Fig. 6.1

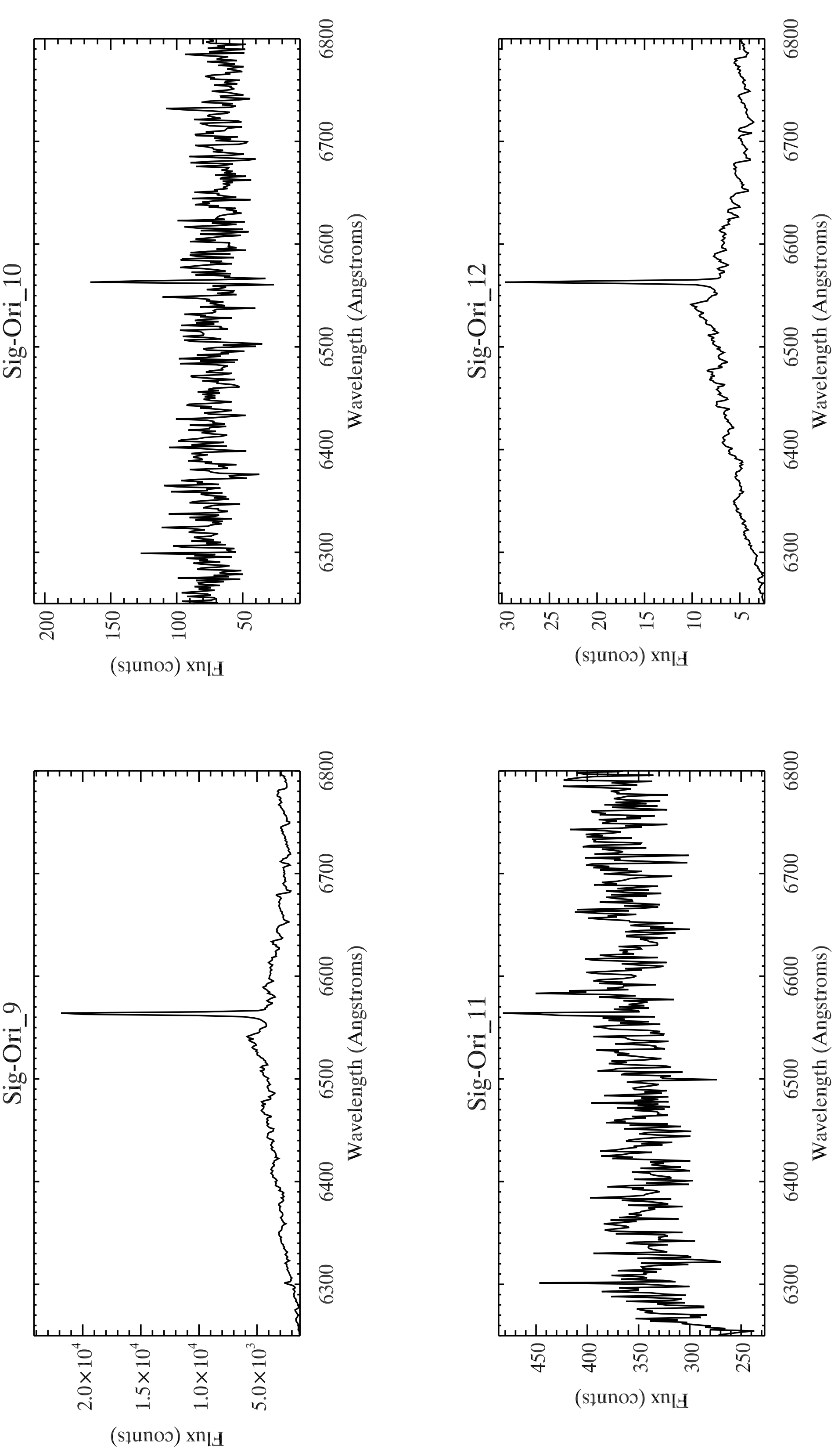

Figure 6.3: Continuation of Fig. 6.1

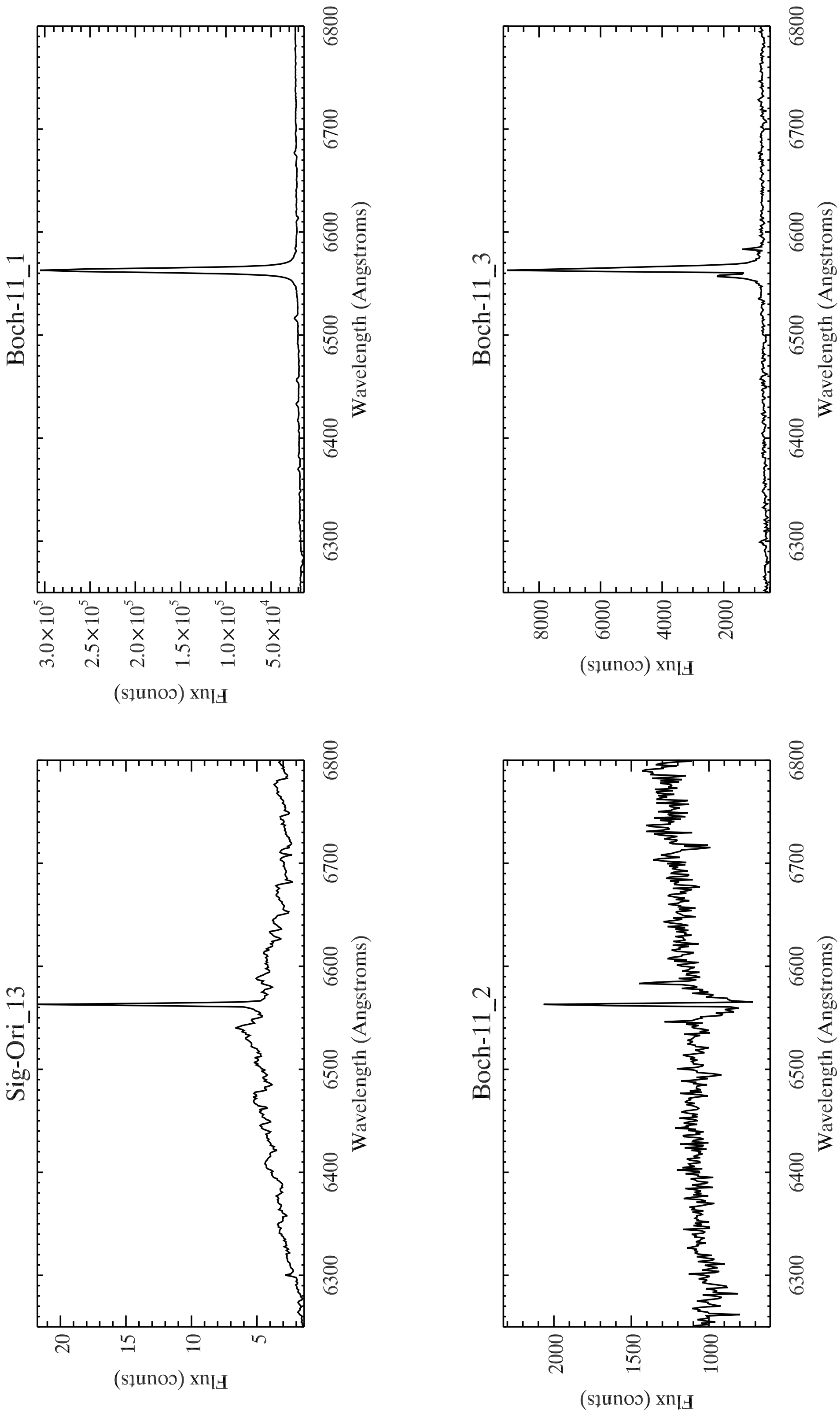

Figure 6.4: Continuation of Fig. 6.1

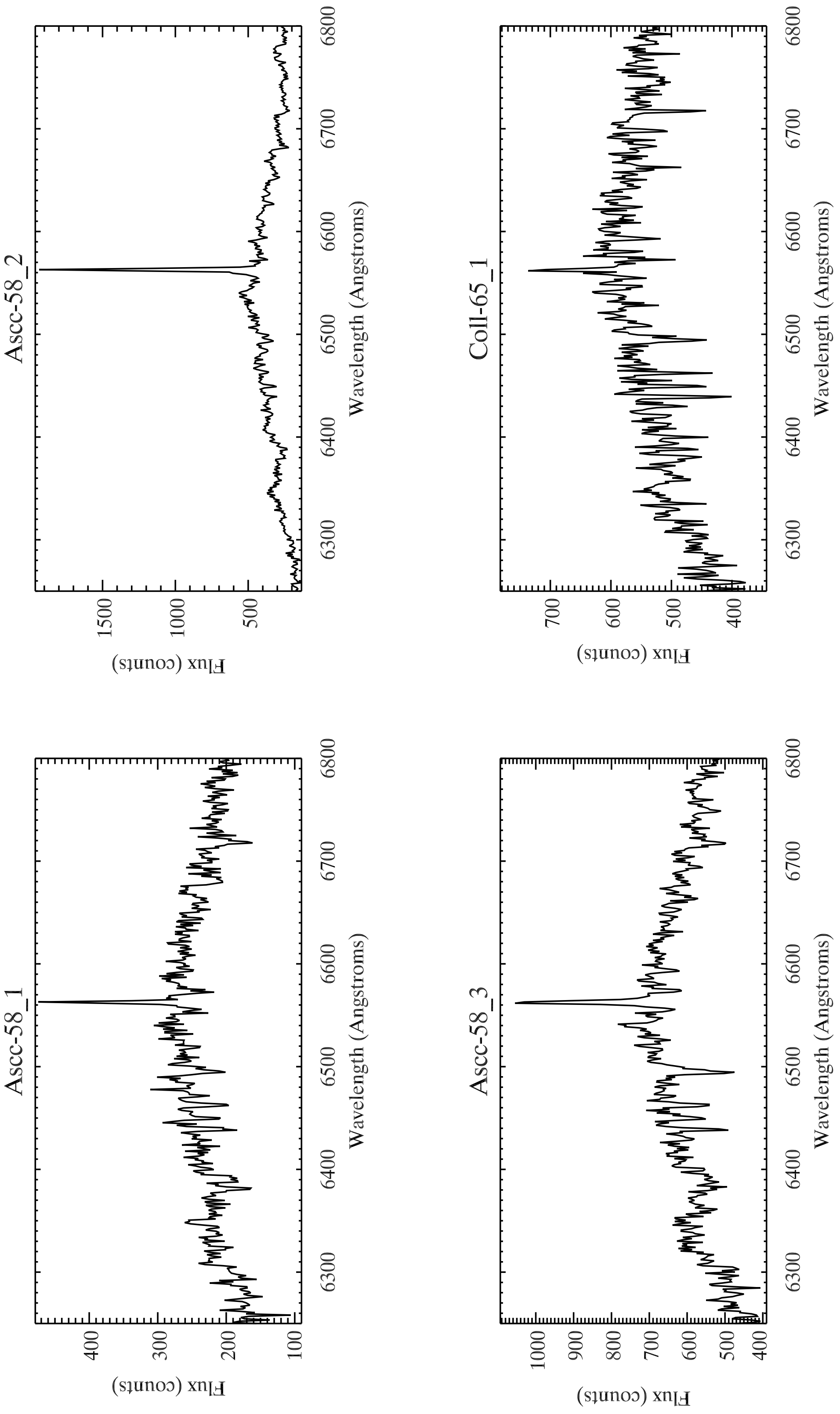

Figure 6.5: Continuation of Fig. 6.1

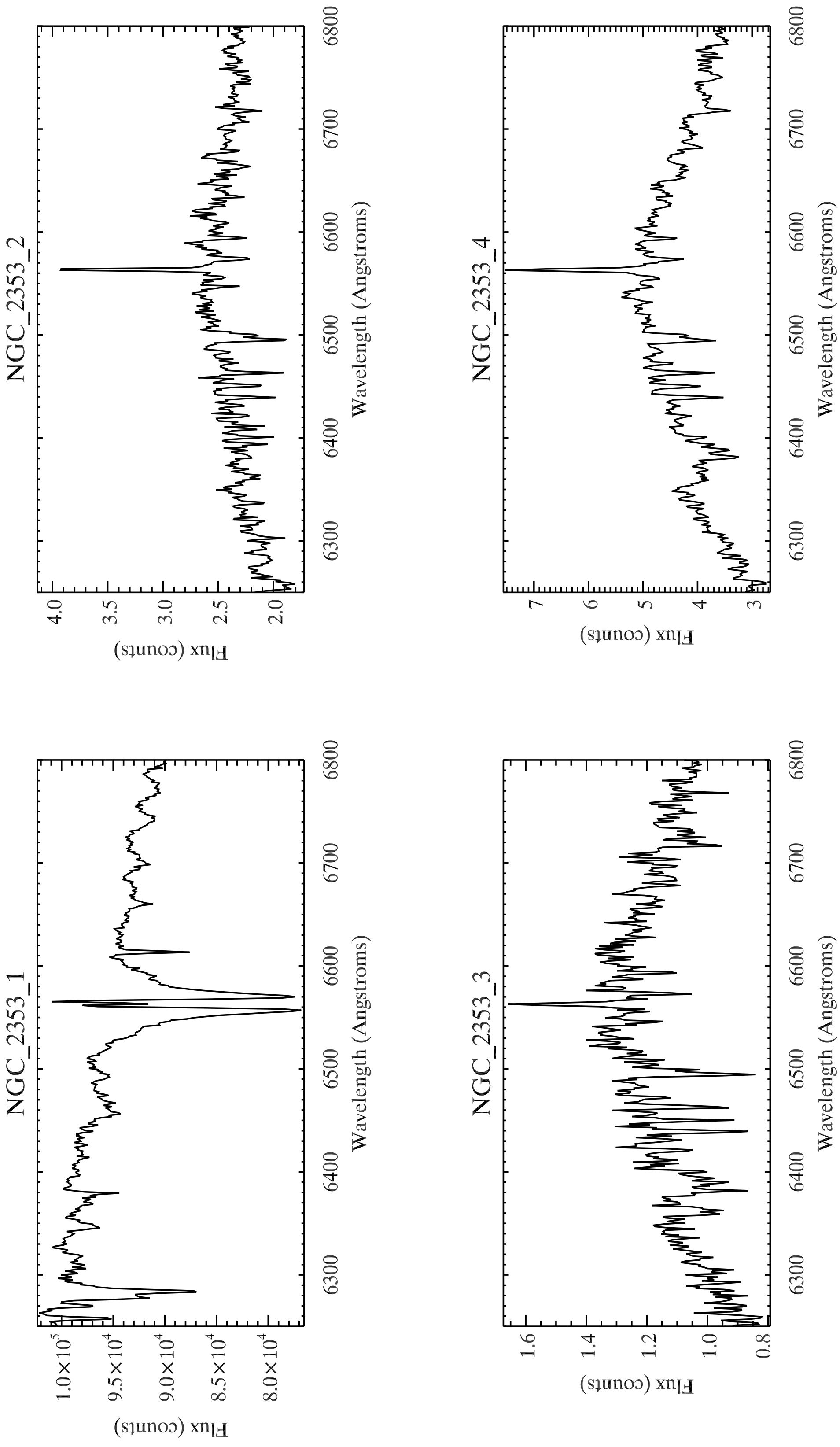

Figure 6.6: Continuation of Fig. 6.1

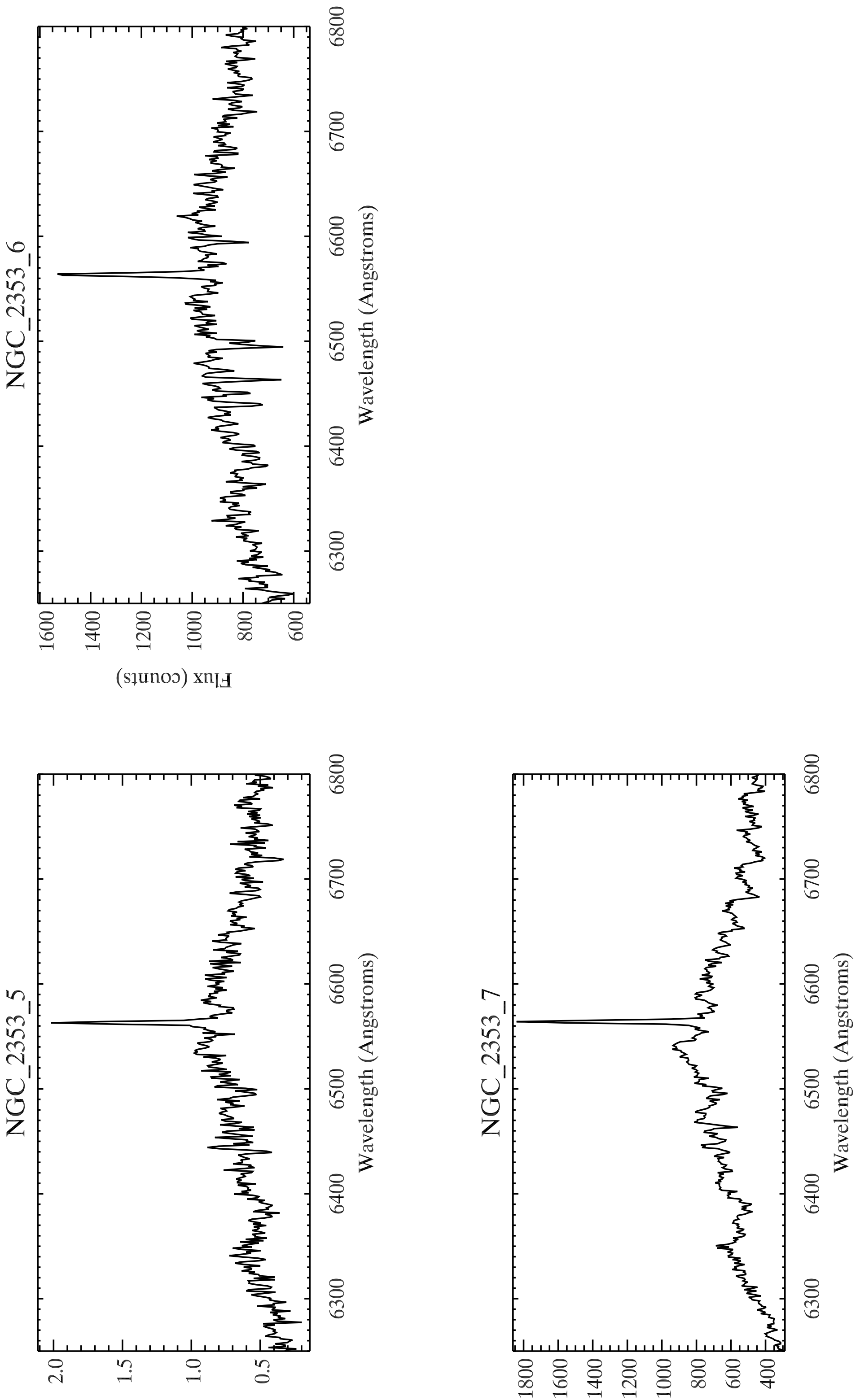

Figure 6.7: Continuation of Fig. 6.1

survey and 2) the "photometric" survey, are unbiased sub-samples of the same parental sample. This allow to perform star counts on the photometric sample (which contains many more stars) and apply the result to the *VIMOS* sample. Three offset regions of equal size (c_1, c_2, c_3) were selected for each cluster as reference for the field stars (Table 6.3). The CMD of c_1, c_2 and c_3 are shown in Figs. 6.10 – 6.15. The fraction of contaminants was computed as the star counts difference in the *VIMOS* regions and the associated offset regions (f_{field}, Table 6.3). We then derived the number of cluster members as the mean difference of the three values. Among the stars observed with *VIMOS* we find that 155 (± 7) are members of the σ Ori cluster, 210 (± 18) of Boshum 11, 115 (± 26) of ASCC 58, 45 (± 16) of Collinder 65 and 242 (± 20) of NGC 2353 ($N_{members}$, Table 6.3).

6.4.2 Frequency of accreting stars

The Hα equivalent width (EW) was historically used to distinguish between accreting stars and stars with active chromosphere. However, the EW may be subject of confusion due to a contrast effect (e.g. Basri & Marci [12]). Stars of later spectral type will have a "reduced" continuum near the line compared to their early spectral type counterpart. As consequence, the pure chromospheric Hα emission will have a larger EW in later spectral type. This was shown by White & Basri [154] and is illustrated in Fig. 6.8 (from White & Basri). The chromospheric Hα line in non-accreting stars (unfilled symbols) cover a large range in EW and have larger EW as the spectral type increases. For this reason, White & Basri proposed a different tool to distinguish accreting and non-accreting stars. They notice that the width of Hα at 10% (H$\alpha_{10\%}$) of the line peak is a good quantitive discriminant. As shown in Fig. 6.8, accreting objects (filled symbols) have systematically larger value of H$\alpha_{10\%}$ compared to non-accreting objects. Stars with H$\alpha_{10\%} > 270$ Km s^{-1}are accreting material from a circumstellar disk. Smaller values of H$\alpha_{10\%}$ have chromospheric origin. For low mass objects, a more reasonable cutoff is 200 km s^{-1} (Jayawardhana et al. 2006). Natta et al. [118] compared the accretion rate derived from model fitting of the Hα profiles with the H$\alpha_{10\%}$ for a small sample of stars in ρ Ophiuchus and Chamaeleon I. Interestingly, they found that Hα correlates well with the accretion rate (Fig. 6.9, from Natta et al. [118]). This is an important result: H$\alpha_{10\%}$ may be used not only as accretion indicator but also to measure the accretion rate in PMS stars.

We have measured the EW and the 10% width of the Hα emission. The spectral continuum was computed using two spectral windows at both sides of Hα. The continuum level in correspondence of the emission line was interpolated using a first order polynomial. The spectra were then continuum-

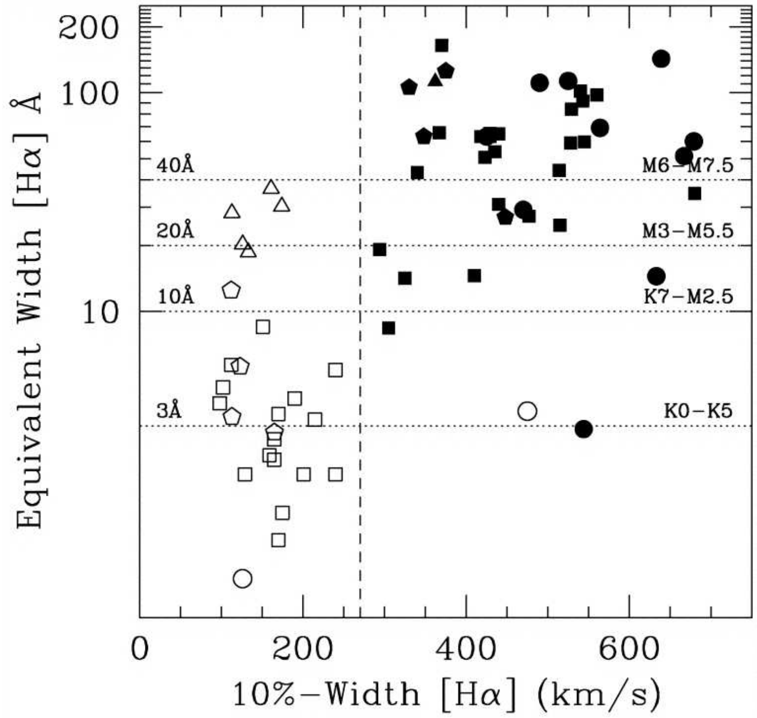

Figure 6.8: *From White & Basri [154]*: Hα equivalent width versus Hα width at 10% for T Tauri stars. Stars with ongoing accretion (filled symbols) have larger 10% width of non-accreting stars (unfilled symbols). A width of 270 Km s^{-1} separates the two categories of stars. Equivalent width may also be used to distinguish between accreting and non-accreting objects. In this case the knowledge of the spectral type of the star is needed. The accretion induced veiling produce an Hα EW of > 3Å in a K0-K5 star, > 10Å in K7-M2.5, > 20Å in M3-M5.5 and >40 Å for M6-M7.5.

normalized and subtracted. H$\alpha_{10\%}$ was measured as the width of the Hα line at the height corresponding to 10% of the line peak. In the case of narrow emission line and low signal-to-noise spectrum, the 10% level might be confused with the neighbor continuum fluctuations. To avoid this, the result was visually inspected. The results are listed in table 6.4. The FWHM of the Hα line was also measured by fitting the line with a Gaussian function. The uncertainty on H$\alpha_{10\%}$ is dominated by the low spectral resolution of our observations. A resolution of $\lambda/\Delta\lambda = 2150$ corresponds to ~ 140 Km s^{-1} ($= \frac{2.998 \cdot 10^5}{2150}$ Km s^{-1}), i.e. the velocity uncertainty is ~ 70 Km s^{-1}.

Combining the results of Table 6.3 and 6.4 we find that 11 out of 155 stars

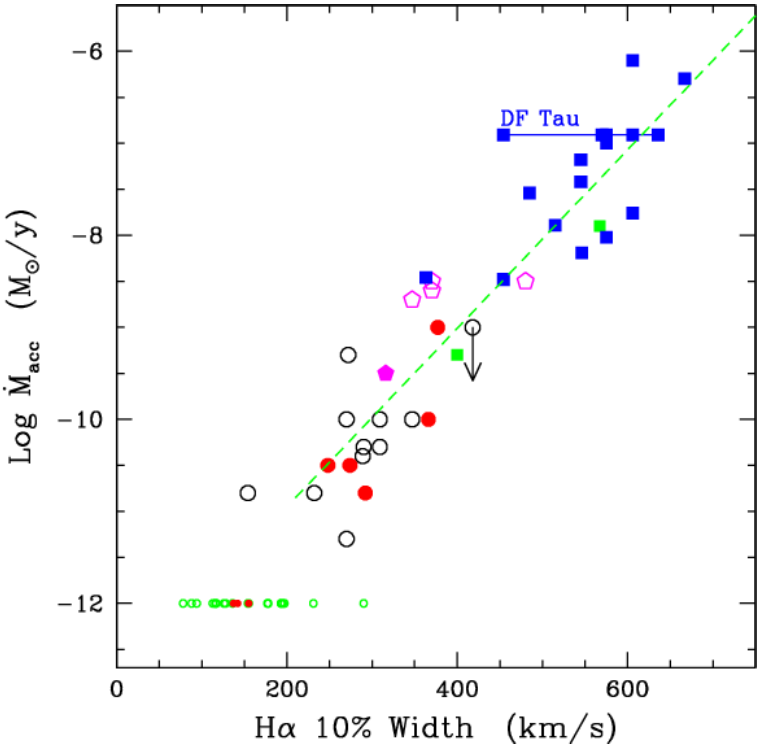

Figure 6.9: *From Natta et al. [118]*: correlation of the $H\alpha_{10\%}$ and mass accretion rate in young stars. Given such a strong correlation over a wide range of accretion rate, $H\alpha_{10\%}$ is a valid accretion indicator and a possible tool for measuring the mass accretion rate in young stars.

in σ Orionis (7 ± 2 %), 3 out of 210 (1.5 ± 0.5 %) in Bochum 11, 2 out of 115 (1.7 ± 0.3 %) in ASCC 58, 0 out of 198 ($0^{+1.6}$ %) in Collinder 65 and 3 out of 242 (1.2 ± 0.2 %) in NGC 2353 are accreting stars. A critical point is the age determination of the cluster. The most recent study of σ Ori suggest an age between 3 – 5 Myr. Patat & Carraro [126] find an age of 4 – 8 Myr for Bochum 11. For the remaining clusters we adopt the age provided by WEBDA. For these clusters the age in WEBDA is estimated by fitting the zero-age-mean-sequence (ZAMS) to the brightest stars of the cluster. We think an accuracy of 30% is a conservative assumption.

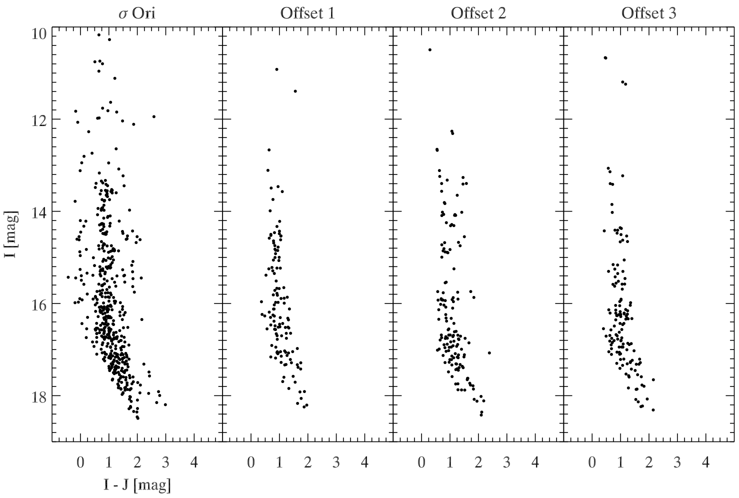

Figure 6.10: Color-Magnitude diagram of the *VIMOS* field σ Orionis (left) and three offset regions.

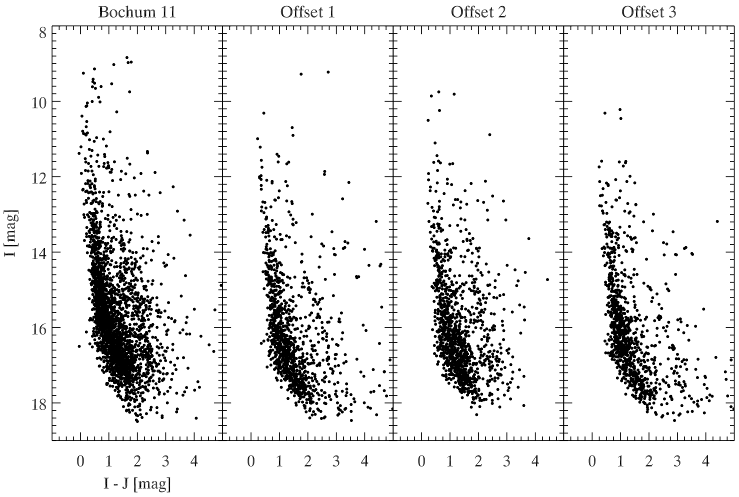

Figure 6.11: Same as Fig. 6.10 for Bochum 11

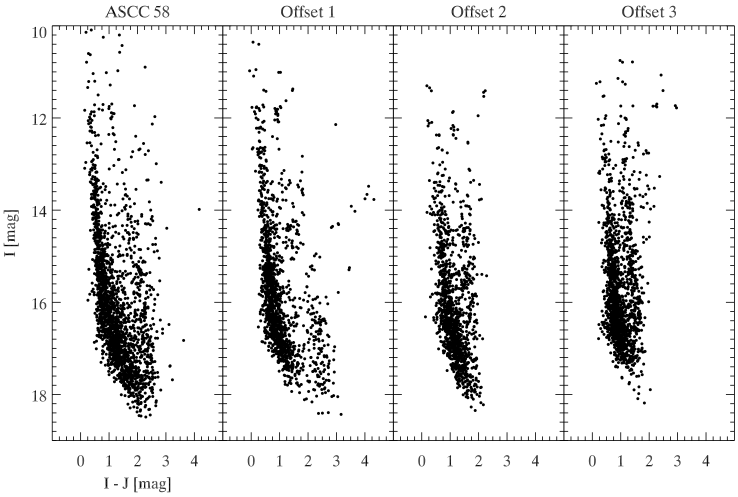

Figure 6.12: Same as Fig. 6.10 for ASCC 58 and Collinder 65.

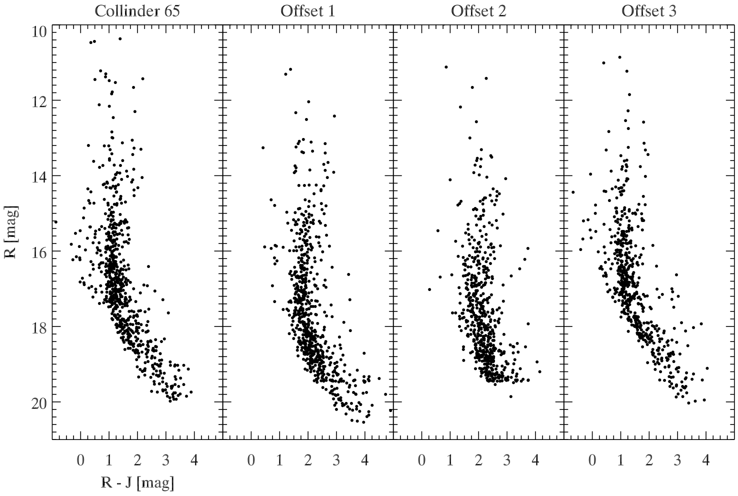

Figure 6.13: Same as Fig. 6.10 for Collinder 65

Figure 6.14

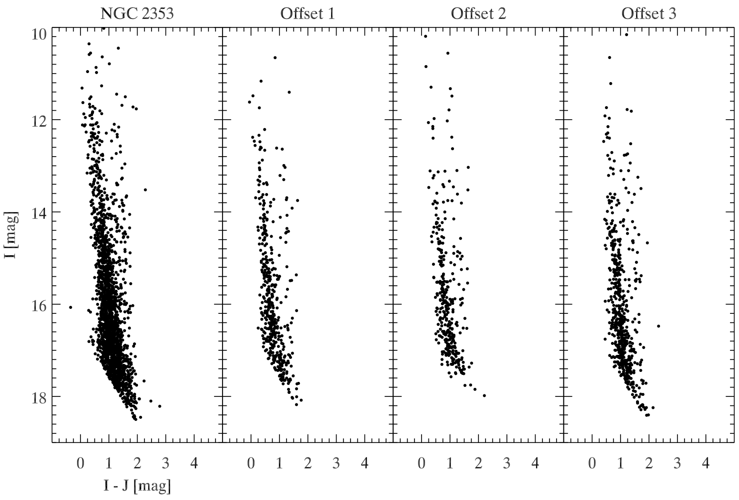

Figure 6.15: Same as Fig. 6.10 for NGC 2353

6.5 Discussion and conclusion

The mass of the central star is known to play a role in the dissipation of gas and dust in disks. Both the fraction of circumstellar disks and accreting stars may vary with spectral type for a given, coeval, stellar cluster. In the case of σ Orionis we found that only 7% of the cluster members are accreting stars. Oliveira et al. [122] find, for the same cluster, an accretors fraction of 30% (± 10%). Similar results were found by Barrado y Navascués & Martin [11] (27% ± 7%) and by Zapatero Osorio et al. [158] (30 - 40%). The difference here is due to the fact that our survey is limited to earlier spectral type (~ M2 - M3) compared to previous work. Barrado y Navascués & Martin measured the fraction of accreting stars in σ Orionis as a function of spectral type. They find that within the range K3 - M5.5, 25% of the stars are accreting. Fig. 5 of Oliveira et al. [122] shows the Hα EW as a function of the spectral type. The number of stars with ongoing accretion peaks around the spectral type range M3 - M5.5. The accretors frequency in Oliveira et al. drops to ~ 7% if we only consider spectral type earlier than M3. This is consistent with our result.

Fig. 6.16 shows the fraction of accreting stars as function of cluster age found here (red dots). We included literature data from Mohanty et al. [112] (filled triangles, ρ Ophiucus, Taurus, Chamaeleontis I, IC 348 and Upper

Table 6.3: Offset fields used for star counts (9 arcmin-radius each)

	l [deg]	b [deg]	f_{field} [%]	$N_{members}$
		σ Ori		
C_1	218.0	-16.8	25	162
C_2	204.0	-17.5	30	151
C_3	212.0	-17.5	30	151
		Bochum 11		
C_1	293.0	-0.75	48	204
C_2	286.0	-0.85	50	197
C_3	293.0	-0.85	42	228
		ASCC 58		
C_1	286.0	+1.3	70	111
C_2	278.0	+1.6	62	141
C_3	292.0	+1.3	75	93
		Collinder 65		
C_1	174.0	-10.9	80	40
C_2	175.0	-11.0	69	61
C_3	190.0	-12.0	83	34
		NGC 2353		
C_1	215.0	+0.38	23	243
C_2	220.0	+0.40	17	262
C_3	230.0	+0.35	30	221

Scorpius), from Jayawardhana et al. [75] (filled squares, η Chamaeleontis, TW Hydrae, β Pictoris and Tucanae-Horologium) and from Dahm & Hillenbrand [32] (star, NGC 2362). As for σ Orionis, the fraction of accretors varies with spectral type in the case of Upper Sco as found by Mohanty et al. [112] increasing from 7% (± 2%) for spectral type later than M4 to 20% (± 10%) for K0 - M4 stars. For the youngest regions, ρ Ophiucus, Taurus, Cha I and IC 348, Mohanty et al. find no appreciable variation, within errors, in the fraction of accretors between low- and high-mass stars. For consistency with our survey we considered here only the result for the earlier types (< M4).

The fraction of accreting stars decreases quickly with time within the first 10 Myr. At the age of 3 - 5 Myr only $\sim$ 7% of the stars in a cluster appear to be in accretion. Between 5 – 10 Myr this number falls to 1 - 2%. No accreting stars is found beyond 10 Myr. A small fraction is found in the 80 Myr NGC 2353 cluster. The η Cha cluster shows an higher accretors frequency compared to clusters of equal age. This particular association shows a similar

Table 6.4: Line properties of the Hα emission.

Ident.	EW [Å]	FWHM [$\mathrm{Km\,s^{-1}}$]	H$\alpha_{10\%}$ [$\mathrm{Km\,s^{-1}}$]
		σ Ori	
1	-7.2	460	720
2	-3.2	160	310
3	-14.2	170	330
4	-1.3	190	260
5	-5.1	130	280
6	-0.2	240	320
7	-2.0	150	330
8	-293.8	260	450
9	-15.9	140	260
10	-3.8	180	160
11	-1.0	120	170
12	-7.7	110	210
13	-9.1	100	200
		Bochum 11	
1	-79.4	270	470
2	-9.7	140	180
3	-63.8	230	610
		ASCC 58	
1	-2.1	90	230
2	-9.7	110	280
3	-2.4	170	360
		Collinder 65	
1	-0.7	100	180
		NGC 2353	
1	-3.9	380	470
2	-1.6	100	190
3	-0.9	130	230
4	-1.6	130	240
5	-4.7	130	320
6	-2.4	160	300
7	-4.6	140	270

behavior in the disk frequency (from near-infrared excess). Age and distance are unlikely to be wrong for this well know system. A possible explanation of this peculiarity is that most of the low-mass stars have already been dispersed,

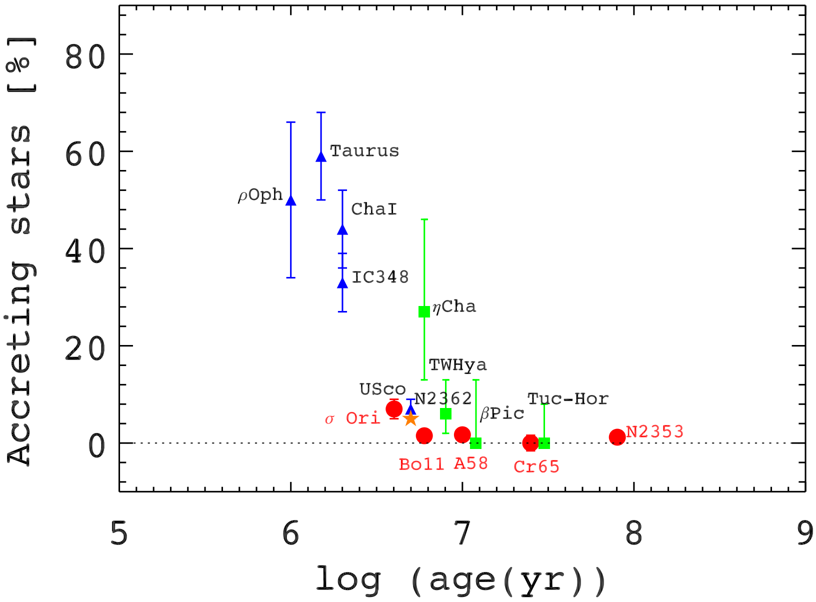

Figure 6.16: Accreting stars frequency as a function of age. Triangles are from Mohanty et al. [112], squares from Jayawardhana et al. [75], star (NGC 2362, here N2362) from Dahm & Hillenbrand [32], circles (this work) are the data points for σ Ori, Bochum 11 (Bo 11), ASCC 58 (A58), Collinder 65 (Cr 65) and NGC 2353. For the latter the errors (smaller than symbols) are dominated by the uncertainty on the cluster membership based on star counts.

making difficult the computation of any statistical quantity.

Viscous accretion appears to ceases around 5 - 10 Myr in early type stars. This age is interestingly similar to the dust dissipation timescale in the inner disc, τ_{dust} = 5 - 9 Myr. Several processes affects the dispersion of disk material. Apart from viscous accretion onto the central star there are also: photo-evaporation, disk and stellar wind/outflow and planet formation. Disk dispersal seems to proceed inside-out, i.e. the material closest to the star is dissipated first. Given this evidence, and the similarity between τ_{acc} and τ_{dust}, we may speculate that viscous accretion is the dominant mechanism of disk dispersion. We cannot exclude photo-evaporation as a secondary mechanism in disk dispersal. This result has important consequence on our knowledge of planet formation. In the conventional *core accretion* planet formation model (Pollack et al. [128]), a giant planet needs 1 - 10 Myr to form. Our result show that already at 5 Myr, a large amount of the inner gaseous and dusty disk is dissipated. Planet formation is likely much faster than predicted so far.

7

Conclusions and future work

7.1 Introduction

The processes of star and planet formation are linked by the presence of the circumstellar disk which surrounds the star during the pre-main-sequence evolution. In this chapter we wish to summarize the results of previous chapters on the structure and evolution of protoplanetary disks and propose new observational projects aimed at contributing to the solutions of open questions in this field.

7.2 Disk's instability

In Chapters 3-4 we studied the outburst of the young star V1647 Orionis and the composition of the associated nebula. V1647 Ori went in outburst in late 2003 and its optical brightness increased by ~ 6 mag. The system remained in outburst for nearly 2 years and showed at its maximum light optical brightness variations on a timescale of 24 h. Some properties of the outburst resemble that of a FU Orionis outburst: the rapid and strong brightness increase, the increased mass accretion rate, the shape of the spectral energy distribution (SED). The presence and morphology of the nebula associated with V1647 Ori is another properties shared with FU Orionis objects. The prevalent theory about the nature of the conical shape of such nebulae is a bipolar structure of circumstellar material in which one of the lobe is oriented toward the observer. While the secondary lobe may be obscured by the disk/envelope, the closest lobe will always appear arc-like unless it is observed pole-on, in which case it will appear ring like. In good agreement with this, the infrared-mm SED suggests the presence of an envelope in which the star-disk system is still partially embedded. The presence of the envelope, and the mass of the disk estimated from sub-millimeter observations (Tsukagoshi et al. [145]) suggest that V1647 Ori is a Class I sources according to the classification of Lada (1987). In Chapter 3 we reported the detection of optical forbidden line emissions during the fading phase of the outburst. These lines are likely produced by a Herbig-Haro object driven by V1647 Ori. This is the first probe of a link between an accretion event and the ejection of material by an Herbig-Haro object.

Among the various models proposed to explain the outburst mechanism, the thermal instability requires indeed the presence of an envelope with an infall rate of material from the envelope into the disk of few 10^{-6} $M_{\odot}$ yr^{-1}. The thermal instability model predicts shorter outburst as the system ages and the infall rate decreases. This may explain the differences between V1647 Ori and "classical" FU Orionis outburst.

On the other hand, the duration of the outburst and the optical/infrared spectrum remind that of an EX Lupi stars, which have shorter and recurrent outbursts. Moreover, V1647 Ori is known to have experienced a previous outburst in 1966-1967. A possible mechanism of producing recurrent and short outbursts in V1647 Ori as well as in EX Lupi objects is via interaction with a (sub)stellar companion. The gravitational force of a companion may perturb the disk and lead to an enhancement of the mass accretion rate.

The statistics of young eruptive star is poor. This makes difficult to state clear conclusions on the nature and classification of outbursts in young stars. Rapid follow-up of future outbursts are badly needed to distinguish between the different instability scenarios.

7.3 High resolution observations of protoplanetary disks

In Chapter 5 we analyzed the structure of three protoplanetary disks around intermediate mass PMS stars. We combined high optical resolution spectroscopy and infrared interferometry to direct compare the gas and dust emitting regions using *UVES* at *VLT* and *MIDI* at *VLTI* respectively. The optical [O I] 6300Å line was used as tracer for the gas, and the N-band spectrum as tracer for the dust. In particular, we derived the radial profile of the [O I] line by simply assuming Keplerian rotation of the gas and compared it to the size of the dust emitting region as found with MIDI observations. These two emissions are expected to come from the surface layers of the disk which are directly irradiated by the stellar photons. Our results show that the gas and dust emitting regions may vary from disk to disk. We find a fairly good agreement for the F4 star HD 135344 B. Both the [O I] and the mid-infrared dust emission are compact with the bulk of both emission coming from within ~ 2 AU from the central star. For this disk, the comparison of our MIDI observations with the SED and direct imaging at 20 μm, suggest the absence of warm dust beyond 2 AU. A ring-like structure "re-appears" at larger radii. The disk around HD 179218 is clearly flared. We do find much more dust emission past 15 AU than we would have expected based on the [O I] emission only. Gas and dust emission are both produced within ~ 3 AU from the star. a further ring of dust emission is found between ~ 15 - 23 AU. Also in this case warm dust seems to be absent forming a gap between ~ 3 - 15 AU. For the third star, HD 101412, the results are unambiguous: this disk must be strongly flared in the gas, but self-shadowed in the dust beyond ~ 2 AU. This is the first observational evidence of gas-dust decoupling in a protoplanetary disk.

A future development of this project is to use high resolution near-infrared spectroscopy with *CRIRES* at *VLT*. The warm temperature ($T \geq 150$ K) and high density ($n = 10^9 - 10^{15}$ cm^{-3}) of the disks excite a rich near-infrared spectrum of molecular ro-vibrational transitions. Fig. 7.1 shows a sketch of the near-infrared molecular emission in protoplanetary disks (Carr [25]). The figure shows the different part of the disk surface traced by different near-infrared lines. Among these, excellent tracers of the gas at different radii from the central stars are:

H_2 ro-vibrational lines @ 2.12 μm & 2.22 μm: molecular hydrogen is the most abundant molecular species and most of the disk mass resides in H_2. The 2.12 μm 1-0 S(1) line has been detected (Bary et al. [10]) in some T Tauri stars. The line width measured in these objects goes from 10 - 30 Km s^{-1}which suggests the possibility that the near-infrared H_2 emission can extend up to ~ 10 AU from the central star. These transitions have very high energy levels above the ground state. To excite such levels very high gas temperature or a strong nearby radiation source is needed. Passive protoplanetary disks are not expected to reach the temperature needed to excite these levels ($T \sim 7000$ K), however, Herbig AeBe stars are strong UV sources (stronger than T Tauri stars). This evidence together with the detection of H_2 in T Tauri stars, make Herbig AeBe stars good candidates to search for H_2 emission. Fig. 7.2 shows a strong H_2 emission at 2.12 μm that we detected in the young star LkHα 264 during the science verification of CRIRES.

CO first overtone ro-vibrational lines @ 2.3-2.5 μm: CO is the second

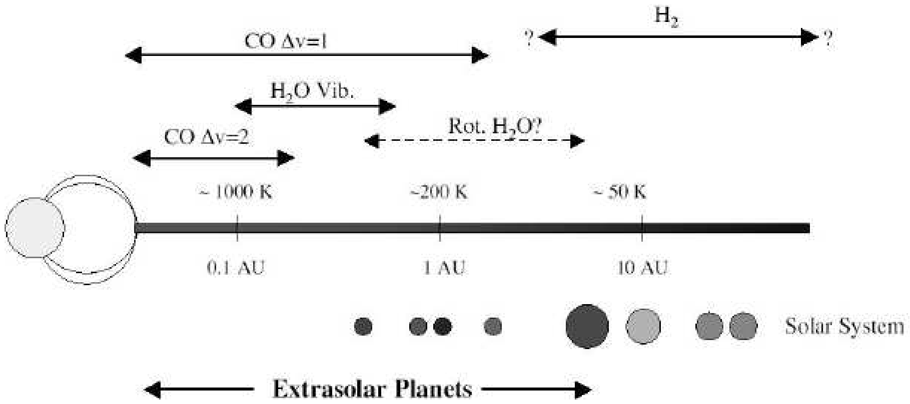

Figure 7.1: Schematic view of a protoplanetary disk with respect to the radial location of planets in the Solar System and known extra-solar planets. At a radius of several stellar radii the disk is truncated by the stellar magnetosphere, and accretion proceeds along the magnetic field lines. The approximate radial location of near-infrared molecular lines is shown (from Carr [25]).

most abundant molecular species after H_2. Previous work has shown that a large fraction ($\sim$ 20%) of young stars have CO first overtone emission (Najita et al. [117]). High spectral resolution studies of these lines provide some of the best evidence for the existence of a rotating disk around young stars. The excitation of emission from the first overtone ro-vibrational levels ($\Delta v = 2$) requires the presence of hot gas ($T >$ 2000 K) and rather high density ($n > 10^{10}$ cm^{-3}). As a consequence, these lines probe the innermost radii of disks around young massive stars ($r \leq 1$ AU).

CO fundamental ro-vibrational lines @ 4.70-5.1 μm: the transition probabilities of these lines are $\sim$ 2 orders of magnitude bigger than the 2.3 μm overtone bands. In addition the fundamental transitions can be excited in cooler gas than the overtone. Because of that, the CO fundamental emission extends over a large range in radii up to few AU from the central star. Moreover, because of their sensitivity to low column densities regions (<< 1 g cm^{-2}), the CO fundamental transitions are a powerful tool to search for gaps (low column density regions) in disks induced by a giant protoplanetary companion.

7.4 Multi-object spectroscopy of young stellar clusters

In Chapter 6 we presented the preliminary results of a multi-object optical spectroscopic survey of young stellar clusters using *VIMOS* at *VLT*. We have

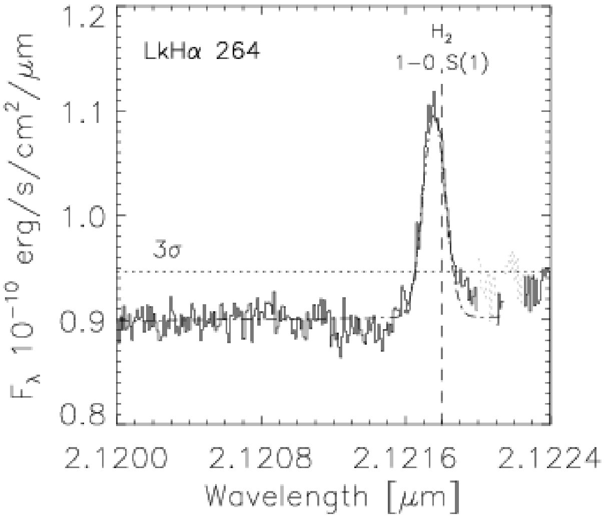

Figure 7.2: H_2 ro-vibrational line at 2.12 μm detected in the pre-main-sequence star LkHα 264. The spectrum was obtained during the science verification of CRIRES.

studied the accretion properties of the 5 clusters in order to determine the frequency of stars with ongoing mass accretion. The clusters were selected in order to have different age. The strongest line produced by the magnetospheric accretion is Hα. Following the method suggested by White & Basri [154], the wings of the line may be used to determine whether the emission is produced by ongoing mass accretion or by the active chromosphere of the star. To do this we measured the width of the line at the 10% of the line peak. We determined the fraction of contaminants stars towards the clusters with a statistical approach: we performed star counts towards the regions of the cluster observed with *VIMOS* and towards 3 nearby offset regions of equal area. As expected we find a different number of accreting stars per cluster. We then compared our result with previous work and we find them the fraction of accreting stars decreases with time. At an age of $\sim$ 5 Myr the systems with ongoing accretion represent the $\sim$ 7% of all cluster members. Between 5 - 10 Myr, this number decreases to 1 - 2 % and is equal to zero beyond 10 Myr. We may clearly state that the accretion timescale, τ_{acc}, is 5 - 10 Myr. The dust dissipation timescale, τ_{dust}, derived from the evolution of the near-infrared excess is 5 - 9 Myr. Interestingly, the two timescales do coincide. This result give insights on the disk dispersal mechanism. Several processes affects the dispersion of disk material. Among these: viscous accretion onto the central star, photo-evaporation, disk and stellar wind/outflow and planet formation. Disk dispersal seems indeed to proceed inside-out, i.e. the material closest to the star is dissipated first. Given this evidence, and the similarity between τ_{acc} and τ_{dust}, we may speculate that viscous accretion is the dominant mechanism of disk dispersion.

In the near future we plan to analyze more in detail the optical spectra obtained with *VIMOS* in order to derive some properties of the clusters (e.g. membership, radial velocity, extinction, members spectral type). The evolution of gas and dust in disks may also be affected by other parameters like: binarity, spectral type, environment. The next step will be to investigate the importance of such parameters on disk evolution through the comparison of optical (*VIMOS*) and infrared data (*HAWK-I* and *Spitzer*).

A
List of publications

The structure of protoplanetary disk surrounding three young intermediate mass stars. II Spatially resolved dust and gas distribution. Submitted to A&A
D. Fedele[1,2,3], M. E. van den Ancker[3], B. Acke[4], G. van der Plas[3,5], R. van Boekel[1], M. Wittkowski[3], Th. Henning[1], J. Bouwman[1], G. Meeus[6] and P. Rafanelli[2]
1 - Max Planck Institut für Astronomie, Heidelberg, Germany
2 - Dipartimento di Astronomia, Universitá degli studi di Padova, Padova, Italy
3 - European Southern Observatory, Garching bei München, Germany
4 - Instituut voor Sterrenkunde, Leuven, Belgium
5 - Sterrenkundig Instituut 'Anton Pannekoek', University of Amsterdam, Amsterdam, The Netherlands
6 - Astrophysikalisches Institut Potsdam, Potsdam, Germany

The structure of protoplanetary disks surrounding three young intermediate mass stars. I. Resolving the disk rotation in the [OI] 6300Åline. A&A 485, 487 (2008)
G., van der Plas[1,2], M.E., van den Ancker[1], D., Fedele[1,3,4], B., Acke[5], C., Dominik[2],L.B.F.M., Waters[2], J., Bouwman[4].
1 - European Southern Observatory, Garching bei München, Germany
2 - Sterrenkundig Instituut 'Anton Pannekoek', University of Amsterdam, Amsterdam, The Netherlands

3 - Dipartimento di Astronomia, Universit Degli Studi Di Padova, Padova, Italy
4 - Max-Planck-Institut fr Astronomie, Heidelberg, Germany
5 - Institute of Astronomy, Leuven, Belgium

A search for near-infrared molecular hydrogen emission in the CTTS LkHα 264 and the debris disk 49 Ceti. A&A 476, 853 (2007)
Carmona, A.[1,2]; van den Ancker, M. E.[2]; Henning, Th.[1]; Goto, M.[1]; Fedele, D.[2,3]; Stecklum, B.[4]
1 - Max Planck Institute for Astronomy, Heidelberg, Germany
2 - European Southern Observatory, Garching bei München, Germany
3 - Dipartimento di Astronomia, Padova, Italy
4 - Thringer Landessternwarte Tautenburg, Tautenburg, Germany

Optical and infrared properties of V1647 Orionis during the 2003-2006 outburst. I The reflection nebula. A&A 472, 199 (2007)
D. Fedele[1,2] - M. E. van den Ancker[1] - M. G. Petr-Gotzens[1] - N. Ageorges[3] - P. Rafanelli[2]
1 - European Southern Observatory, Garching bei Mnchen, Germany
2 - Dipartimento di Astronomia, Universit degli studi di Padova, Padova, Italy
3 - European Southern Observatory, Santiago, Chile

Optical and infrared properties of V1647 Orionis during the 2003-2006 outburst. II Temporal evolution of the eruptive source. A&A 472, 207 (2007)
D. Fedele[1,2] - M. E. van den Ancker[1] - M. G. Petr-Gotzens[1] - P. Rafanelli[2]
1 - European Southern Observatory, Garching bei Mnchen, Germany
2 - Dipartimento di Astronomia, Universit degli studi di Padova, Padova, Italy

The K-band intensity profile of R Leonis probed by VLTI/VINCI. A&A 431, 1019 (2005)
D. Fedele[1,2] - M. Wittkowski[1] - F. Paresce[1] - M. Scholz[3,4] - P. R. Wood[5] - S. Ciroi[2]
1 - European Southern Observatory, Garching bei Mnchen, Germany
2 - Dipartimento di Astronomia, Universit di Padova, Padova, Italy
3 - Institut fr Theoretische Astrophysik der Universitt Heidelberg, Heidelberg, Germany
4 - School of Physics, University of Sydney, Sydney, Australia
5 - Research School for Astronomy and Astrophysics, Canberra, Australia

Acknowledgment

This work was possible thanks to the ESO studentship proramme and to the Deutscher Akademischer Austausch Dienst (DAAD). A deep thanks to Mario van den Ancker for being an enthusiastic supervisor, for his many advises and help. I wish to thank Thomas Henning for having hosted me at MPIA and for his many useful advises. Thanks also to Piero Rafanelli. Thanks to Arjan Bik, Anna Gallazzi, Anna Pasquali, Domenico Tamburro and Stefano Zibetti who helped me in writing this thesis. Thanks to Andres Carmona, Bram Acke, Gerrit van der Plas for their contribution to this work. Thanks to Jeroen Bouwman, Aurora Sicilia-Aguilar and Roy van Boekel for the interesting discussions. I wish also to thank all the people that I met during the last three years at ESO-Garching and at MPIA.

My warmest and deepest thanks to **Veronica** *who made this work possible.*

Bibliography

[1] Abraham P., Kospal A., Csizmadia A. et al. 2004, A&A, 419,L39

[2] Abraham, P., Mosoni, L., Henning, T. et al. 2006, A&A, 449,L13

[3] Acke, B., & van den Ancker, M. E. 2004, A&A, 426, 151

[4] Acke, B., van den Ancker, M. E., & Dullemond, C. P. 2005, A&A, 436, 209

[5] Acke, B., & van den Ancker, M. E. 2006, A&A, 449, 267

[6] Acosta-Pulido, J. A., et al. 2007, AJ, 133, 2020

[7] Andrews, S.M., Rothberg, B., Simon, T. 2004, ApJ, 610,L45

[8] Appenzeller, I. et al. 1998, The Messenger ,94,1

[9] Aspin, C., Barbieri, C., Boschi, F., et al. 2006, AJ, 132,1298

[10] Bary et al. 2003 ApJ 586, 1136

[11] Barrado y Navascués, D., Martin, E.L. 2003, AJ, 126, 2997

[12] Basri, G., & Marcy, G. W. 1995, AJ, 109, 762

[13] Bastien, P., Menard, F., 1988, ApJ, 326, 334

[14] Bell, K.R., et al. 1995, ApJ, 444,376

[15] Behrend, R., & Maeder, A. 2001, A&A, 373, 190

[16] Berger, J. P., & Segransan, D. 2007, New Astronomy Review, 51, 576

[17] Bonnel, I. & Bastien, P. 1992, ApJ, 401, 654

[18] Boersma, C., Bouwman, J., Lahuis, F., van Kerckhoven, C., Tielens, A. G. G. M., Waters, L. B. F. M., & Henning, T. 2008, A&A, 484, 241

[19] Bouwman, J., Lawson, W. A., Dominik, C., Feigelson, E. D., Henning, T., Tielens, A. G. G. M., & Waters, L. B. F. M. 2006, ApJL, 653, L57

[20] Bouwman, J., et al. 2008, ArXiv e-prints, 802, arXiv:0802.3033

[21] Briceño, C., Vivas, A.K., Hernandez, J. et al. 2004, ApJ, 606, L123

[22] Brown, J. M., et al. 2007, ApJL, 664, L107

[23] Brown, J. M., Blake, G. A., Qi, C., Dullemond, C. P., & Wilner, D. J. 2008, ApJL, 675, L109

[24] Cardelli, J.A., Clayton, G.C., Mathis, J.S. ApJ, 345, 245

[25] Carr, J. 2005, High Resolution Infrared Spectroscopy in Astronomy, 203

[26] Cesaroni, R., Galli, D., Lodato, G., Walmsley, C. M., & Zhang, Q. 2007, Protostars and Planets V, 197

[27] Chesneau, O., et al. 2006, A&A, 455, 1009

[28] Clarke, C., Lin, B.D.C.,& Pringle, J.E., 1990 MNRAS, 242, 439

[29] Clarke, C., et al. 2005 MNRAS, 361, 942

[30] Cohen, M. et al. 1999 AJ, 117, 1864

[31] D'Alessio, P., Calvet, N., & Hartmann, L. 2001, ApJ, 553, 321

[32] Dahm, S. E., & Hillenbrand, L. A. 2007, AJ, 133, 2072

[33] Dent, W. R. F., Greaves, J. S., & Coulson, I. M. 2005, MNRAS, 359, 663

[34] Doucet, C., Habart, E., Pantin, E. et al. 2007, A&A, 470, 625

[35] Doucet, C., Pantin, E., Lagage, P. O., & Dullemond, C. P. 2006, A&A, 460, 117

[36] Duchêne, G., & Ménard, F. 2007, A&A, 470, 625

[37] Dullemond, C. P., Dominik, C., & Natta, A. 2001, ApJ, 560, 957

[38] Dullemond, C. P., & Dominik, C. 2004, A&A, 421, 1075

[39] Dullemond, C. P., & Dominik, C. 2005, A&A, 434, 971

[40] Eislöffel, J., & Mundt, R. 1997, AJ, 114, 280

[41] Eisner, J. A., Lane, B. F., Hillenbrand, L. A. et al. 2004, ApJ, 613, 1049

[42] Eisner, J. A., Hillenbrand, L. A., White, R. J. et al. 2007, ApJ, 669, 1072

[43] Fedele, D., van den Ancker, M. E., Petr-Gotzens, M. G., Ageorges, N., & Rafanelli, P. 2007, A&A, 472, 199

[44] Fedele, D., van den Ancker, M. E., Petr-Gotzens, M. G., & Rafanelli, P. 2007, A&A, 472, 207

[45] Gammie, C.F. 1996, ApJ, 457, 355

[46] Garcia et al. 1999, A&A, 346, 892

[47] Geers, V. C., et al. 2006, A&A, 459, 545

[48] Geers, V. C., van Dishoeck, E. F., Visser, R. et al. 2007, A&A, 476, 279

[49] Gerakines, P.A., Whittet, D.C.B. & Lazarian A. 1995 ApJ, 455,L171

[50] Glassgold, A. E., Najita, J. R., & Igea, J. 2007, ApJ, 656, 515

[51] Goodrich, R.W., 1987 PASP, 99,116

[52] Gorti, U. & Hollenbach, D., 2008 in preparation

[53] Green, T. 1001 American Scientist, 89, 4

[54] Green, J.D. et al. 2006 ApJ, 648,1099

[55] Grosso, N., Kastner, J.H., Ozawa, H. et al. 2005 A&A 438, 159

[56] Hartmann, L. & Kenyon S.J. 1996 ARA&A 34, 207

[57] Habart, E., Natta, A., & Krügel, E. 2004, A&A, 427, 179

[58] Habart, E., Natta, A., Testi, L., & Carbillet, M. 2006, A&A, 449, 1067

[59] Haisch, Lada & Lada 2001 ApJ, L553,153

[60] Haisch, K. E., Jr., Jayawardhana, R., & Alves, J. 2005, ApJL, 627, L57

[61] Hartmann, L., 1998 *Accretion processes in star formation*

[62] Henning, Th. Early Phases of Planet Formation in Protoplanetary Disks.: Nobel Symposium (2007), in press.

[63] Herbig, G.H. 1966 Vistas in Astronomy 8, 10

[64] Herbig, G.H. 1977 ApJ, 217, 693

[65] Hernandez et al. 2004, AJ, 127, 1682

[66] Hessman et al. 1991, ApJ, 370, 384

[67] Hillenbrand et al. 1998, AJ 116, 1816

[68] Hillenbrand 2006, eds. M. Livio, STScI Symposium Series #19

[69] Hornes optimal extraction (Horne, K., 1986, PASP, 98, 609

[70] Ireland, M. J., & Kraus, A. L. 2008, ApJL, 678, L59

[71] Isella, A., & Natta, A. 2005, A&A, 438, 899

[72] Isella, A., Testi, L., & Natta, A. 2006, A&A, 451, 951

[73] Jaffe, W.J. 2004, Proc. SPIE, 5491, 715

[74] Jayawardhana et al. 1999 ApJ, 521, L129

[75] Jayawardhana, Mohanty & Basri 2003 ApJ, 592, 282

[76] Jayawardhana et al. 2006 ApJ, 648, 1206

[77] Johansen, A., Oishi, J. S., Low, M.-M. M., Klahr, H., Henning, T., & Youdin, A. 2007, Nature, 448, 1022

[78] Johansen, A., Brauer, F., Dullemond, C., Klahr, H., & Henning, T. 2008, A&A, 486, 597

[79] Jonkheid, B., Faas, F. G. A., van Zadelhoff, G.-J., & van Dishoeck, E. F. 2004, A&A, 428, 511

[80] Kastner, J. H., et al. 2006, ApJL, 648,L43

[81] Kawazoe, E. & Mineshige, S. 1993 PASP, 45, 715

[82] Käufl, H-U. et al. 2003, SPIE 4841, 117

[83] Kamp, I., & Dullemond, C. P. 2004, ApJ, 615, 991

[84] Kenyon S.J., et al. 2000 ApJ, 531, 1028

[85] Kenyon, S.J., Hartmann, L.W. 1991 ApJ, 383, 664

[86] Kenyon, S.J., Hartmann, L.W. 1995 ApJS, 101, 117

[87] Kirkpatrick, J.D. et al. 1999 ApJ, 519,834

[88] Koenigl, A. 1991, ApJL, 370, L39

[89] Kospal, A., Abraham, P., Acosta-Pulido, J., 2005 IBVS, 5661.

[90] Kospal, A., Abraham, P., Prusti, T., et al. 2006 ASPC, 349, 269

[91] Lada & Wilking 1984, ApJ, 287, 610

[92] Lada, C. J. 1987, Star Forming Regions, 115, 1

[93] Lahuis, F., van Dishoeck, E. F., Blake, G. A. et al. 2007, ApJ, 665, 492

[94] Lawson, P. R. 2000, *Principles of Long Baseline Stellar Interferometry*, edited by Peter R. Lawson, published by National Aeronautics and Space Administration, Jet Propulsion Labratory, California Institute of Technology, Pasadena, 2000.

[95] LeFevre, O., et al. 2003, Proc. SPIE, 4841, 1670

[96] Leinert, Ch., Graser, U., Przygodda, F. et al. 2003, Ap&SS, 285, 73

[97] Leinert, C., et al. 2004, A&A, 423, 537

[98] Lenzen, R. et al. 2003, SPIE, 4841,944

[99] Lin, B.D.C., & Papaloizou, J.C.B. 1985 *Protostars and Planets II*

[100] Liu, W. M., Hinz, P. M., Meyer, M. R., et al. 2007, ApJ, 658, 1164

[101] Lucas, P.W. et al. 2004, MNRAS352,1347

[102] Lynden-Bell D. & Pringle F. E. 1974 MNRAS 168, 603

[103] Magnier E.A., Waters L.B.F.M., Groot P.J. et al. 1999 A&A, 346, 441

[104] Mallas, J.H., & Kreimer, E. 1970 *The Messier Album*

[105] Mayor, M & Queloz D. 1995 Nature 378, 355

[106] McGehee, P.M., Smith, J.A., Henden, A.A. et al. 2004 ApJ, 616, 1058

[107] McNeil, J.W. 2004 IAU Circ. 8284

[108] Meeus, G., Waters, L.B.F.M, Bouwman, J. et al. 2001, A&A, 365, 476

[109] Megeath, S.T., Allen, L.E., Allgaier, E. et al. 2006 IAUS 237, 167

[110] Millan-Gabet, R., Schloerb, F. P., & Traub, W. A. 2001, ApJ, 546, 358

[111] Millan-Gabet, R., Malbet, F., Akeson, R., Leinert, C., Monnier, J., & Waters, R. 2007, Protostars and Planets V, 539

[112] Mohanty, S., Jayawardhana, R., & Basri, G. 2005, ApJ, 626, 498

[113] Monnier, J. D., et al. 2006, ApJ, 647, 444

[114] Montmerle, T. 2007, IAUS 243, page 23

[115] Muzerolle, J. et al. 2003 ApJ, 592, 266

[116] Muzerolle, J. et al. 2005 ApJ, 620, L107

[117] Najita et al. 2000, PPIV

[118] Natta, A., Testi, L., Muzerolle, J., Randich, S., Comerón, F., & Persi, P. 2004, A&A, 424, 603

[119] Natta, A. et al. 2006 A&A 452, 245-252

[120] Natta, A., Testi, L., Calvet et al. 2007, Protostars and Planets V, 767

[121] Nomura, H., & Millar, T. J. 2005, A&A, 438, 923

[122] Oliveira, J. M., Jeffries, R. D., van Loon, J. T., & Rushton, M. T. 2006, MNRAS, 369, 272

[123] Ojha, D. K., Kusakabe, N., Tamura, M. et al. 2006, PASJ, 57,203

[124] Ojha, D. K., Ghosh, S. K., Tej, A. et al. 2006, MNRAS, 368,825

[125] Padgett, D.L, Brandner, W., Stapelfeldt, K.R. et al. 1999, AJ, 117,1490

[126] Patat, F., & Carraro, G. 2001, MNRAS, 325, 1591

[127] Pascucci, I., et al. 2007, ApJ, 663, 383

[128] Pollack et al. 1996 Icarus, 124,62

[129] G. Perrin and F. Malbet (eds) EAS Publications Series, Vol. 6, 2003

[130] Quanz, S. P., Henning, T., Bouwman, et al. 2006, ApJ, 648, 472

[131] Ratzka, T. Ph.D. Thesis, Ruprecht-Karls-Universität Heidelberg

[132] Reipurth, B., Aspin, C., 2004 ApJ, 606, L119

[133] Rettig, T.W., Brittain, S.D., Gibb, E.L. et al. 2005 ApJ, 626,245

[134] Rossi, et al. 1999, A&AS, 136, 95

[135] Rousset, G. et al. 2002, SPIE, 4389,140

[136] Sandell, G. & Weintraub, D.A. 2001 ApJ, 134, 115

[137] Shevchenko, 1999, Astronomy Reports 43, 246

[138] Sicilia-Aguilar, A., Hartmann, L. W., Fürész, G., Henning, T., Dullemond, C., & Brandner, W. 2006, AJ, 132, 2135

[139] Semkov, E.H. 2004 IBVS, 5578.

[140] Semkov, E.H. 2004 IBVS, 5683.

[141] Serkowski, K. Mathewson, D.S. & Ford, D.L. 1975, ApJ, 196,261

[142] Sloan, G. C., et al. 2005, ApJ, 632, 956

[143] Smith J., et al. 2002 AJ, 123, 2121

[144] Stetson P., 2000 PASP, 112, 925

[145] Tsukagoshi, T. et al. 2005 PASJ, 57, L21

[146] Vacca, W.D., Cushing, M.C. Simon, T. 2004 ApJ, 609, L29

[147] van Boekel, R., Waters, L. B. F. M., Dominik, C. et al. 2004, A&A, 418, 177

[148] van Boekel, R., Min, M., Waters, L. B. F. M. et al. 2005, A&A, 437, 189

[149] Van den Ancker et al. 2004, MNRAS, 349, 1516

[150] van der Plas, G., van den Ancker, M. E., Fedele, D., Acke, B., Dominik, C., Waters, L. B. F. M., & Bouwman, J. 2008, A&A, 485, 487

[151] Van der Bliek, N.S., et al. 1996 A&AS, 109,547

[152] Visser, R., Geers, V. C., Dullemond, C. P., et al. 2007, A&A, 466, 229

[153] Walter, F. M., et al. 2004, AJ, 128, 1872

[154] White, R. J., & Basri, G. 2003, ApJ, 582, 1109

[155] Whitney, B.A., Hartmann, L., 1993, ApJ, 402, 605

[156] Whittet, D. C. B., et al. 1992, ApJ, 386, 562

[157] Youdin, A. N., & Shu, F. H. 2002, ApJ, 580, 494

[158] Zapatero Osorio, M. R., Béjar, V. J. S., Pavlenko, Y., Rebolo, R., Allende Prieto, C., Martín, E. L., & García López, R. J. 2002, A&A, 384, 937

[159] Zinnecker, et al. 1999, A&A, 352,L73